# Molecular Dynamics Simulations of Confined Liquids in Nanochannels with Rough Walls

Michail Papanikolaou

Submitted for the Degree of Ph.D.

Institute of Aerospace Sciences

Cranfield University

Cranfield, UK

2017

**Cranfield University**

School of Aerospace, Transport and Manufacturing (SATM)

PhD

**Michail Papanikolaou**

**Molecular Dynamics Simulations of Confined Liquids in Nanochannels with Rough Walls**

Supervisor

Professor Dimitris Drikakis

February 17

# Abstract

During the past few decades Micro-Electromechanical systems (MEMS) have been increasingly used in various engineering domains ranging from electronics to biological sciences as nowadays they can be massively produced in numerous shapes and with various compositions. Additionally, the development of the manufacturing techniques has allowed MEMS to be easily integrated into devices and expand their applications as sensors and actuators. The future of MEMS seems to be more than promising; however the small scales involved in this type of devices give rise to phenomena that cannot be treated by continuum simulations such as Computational Fluid Dynamics (CFD) or Computational Structural Dynamics (CSD). On the contrary, Molecular Dynamics (MD) Simulations are considered to be an effective approach in investigating the flow behaviour and the rheological properties of liquids in the nanoscale.

The aim of this PhD project is to establish and implement Molecular Dynamics Models for the investigation of nano-scale liquid flows and the fluid properties in nanochannels with rough walls. This thesis uses MD to investigate the effect of nano-scale roughness on the slip length, the fluid viscosity and the Kapitza resistance. Rough nanochannel walls have been modelled with the help of the multivariate Weierstrass - Mandelbrot (W-M) function which has been used in the past to describe fractally rough surfaces being common in nature.

A number of different approaches have been used to extract the aforementioned thermodynamic and flow properties including Equilibrium Molecular Dynamics (EMD) and Non-Equilibrium Molecular Dynamics (NEMD) Simulations. The outcomes of this research suggest that surface roughness can greatly affect the flow behaviour of highly confined liquids as well as their thermodynamic behaviour. Therefore they could potentially be used as a first step for the selection of the surface treatment and finishing techniques of MEMS devices according to the desired fluid behaviour.

# Acknowledgements

# Contents

# List of Figures

x

# List of Tables

# Abbreviations

| | |
|---|---|
| AFM | Atomic Force Microscopy |
| AMM | Acoustic Mismatch Model |
| APF | Atomic Packing Factor |
| BCC | Body Centred Cubic |
| CFD | Computational Fluid Dynamics |
| CHF | Constant Heat Flux |
| CSD | Computational Structural Dynamics |
| CWT | Constant Wall Temperature |
| DFT | Density Functional Theory |
| DMM | Diffuse Mismatch Model |
| DPD | Dissipative Particle Dynamics |
| DSMC | Direct Simulation Monte Carlo |
| EAM | Embedded Atom Model |
| EBT | Embedded Based Techniques |
| EDM | Electro Discharge Machining |
| EMD | Equilibrium Molecular Dynamics |
| FCC | Face Centred Cubic |
| FEA | Finite Element Analysis |
| GD | Geometric Decomposition |
| HCP | Hexagonal Close Packed |
| LB | Lattice Boltzmann |
| LGA | Lattice Gas Cellular Automata |
| LIGA | Lithographie Galvanoformung Abformung |
| MD | Molecular Dynamics |
| MEAM | Modified Embedded Atom Model |
| MEMS | Micro Electro Mechanical Systems |
| MSD | Mean Square Displacement |
| NEMD | Non Equilibrium Molecular Dynamics |
| PDMS | Polydimethylsiloxance |
| PVDF | Polyvinylidene Fluoride |
| RDF | Radial Distribution Function |
| ReaxFF | Reactive Force Field |
| RTT | Reynolds Transport Theorem |
| VACF | Velocity Autocorrelation Function |
| VdW | Van der Waals interaction |
| μ-PIV | Micron-resolution Particle Image Velocimetry |
| ITR | Interfacial Thermal Resistance |

# 1 Introduction

## 1.1 Micro and Nano Flows

During the past few decades, the enhancement of the micromachining processing techniques has made the fabrication of MicroElectroMechanical Systems (MEMS) feasible [1] and contributed to their integration in commercial and scientific applications mainly as sensors and actuators ([2], [3]). MEMS are comprised of elements such as microfluidic networks with dimensions varying between 0.1 and 100 μm.

In such small scales where the interaction between the wall and the fluid particles becomes increasingly important, the flow behaviour of liquids confined in micro- and nanochannels presents some unique characteristics and varies from the corresponding one in large systems. Continuum Models (e.g. CFD, FEA) have been the staple of computational simulations of many engineering problems over the last century. However, they fail to describe the flow in nanofluidic systems ([4]–[6]), as some of the assumptions made like the Navier-Stokes no slip boundary condition, break down in such small scales. Therefore, alternative methods derived from first principles should be adopted.

## 1.2 Modelling Approaches for Nano Flows

Recent advances in computing have made the investigation of the mechanics of fluids and materials in the nanoscale feasible with the use of molecular models. Molecular models can be simulated using two techniques: Molecular Dynamics [7] and Monte Carlo [8], which can be used to investigate the structure and dynamics of small systems in fine detail. However, their high computational expense limits their use to a relatively small computational domain compared to continuum models.

Multiscale methods attempt to bridge the accurate microscopic models with the efficient continuum ones (Figure 1.1). These methods can be divided into 2 groups: the mesoscale and the hybrid ones. Mesoscale methods work with intermediate resolution, i.e. a single solver that can simulate large physical phenomena taking into account the essential detail of the molecular interactions. This is achieved by replacing an atomic description by larger particles while averaging fine detail out. The most common mesoscale methods are: i) Lattice Gas Cellular Automata (LGA) ([9], [10]), ii) the Lattice-Boltzmann (LB) method ([11], [12]), iii) Dissipative Particle Dynamics (DPD) ([13], [14]), and iv) Direct Simulation Monte Carlo (DSMC) ([15], [16]). On the other hand, hybrid models employ two solvers, a molecular (e.g. Molecular Dynamics, Monte Carlo) and a continuum one (e.g. CFD, FEA). The challenge in such an approach is the transparent exchange of information between the two. Hybrid models can be classified into Geometric Decomposition (GD) ([17]–[19]) and Embedded Based Techniques (EBT) ([20]–[22]) depending on how the length scales are decoupled (Figure 1.2).

**1.2** Modelling Approaches for Nano Flows
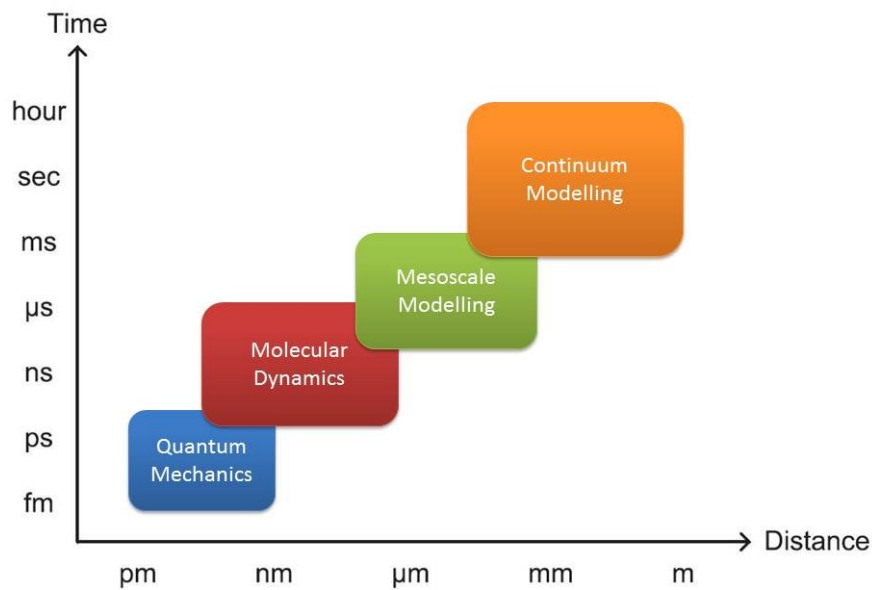


**Figure 1.1:** Modelling approaches for Nano Flows at various spatial and temporal scales

The focus of this PhD study is correlating phenomena taking place in nanochannels with the topography of the nanochannel walls which is a problem limited in small scales at least in its initial steps. Therefore Molecular Dynamics models should be employed, as they are considered to be the most dominant and effective atomistic simulation technique. Using mesoscale and hybrid methods to extend this research to coarser scales is a future goal that has to be pursued.
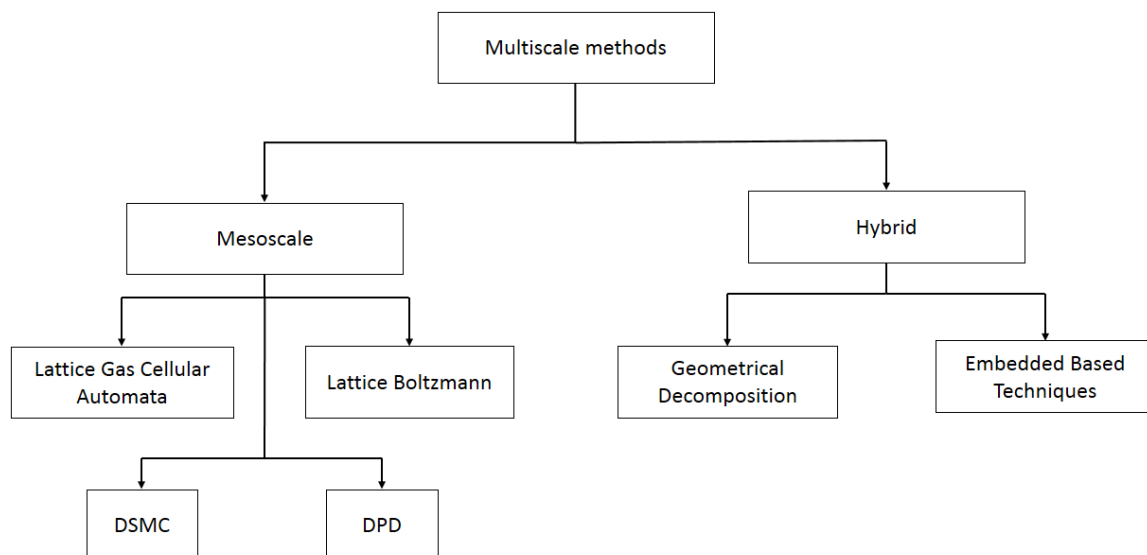


**Figure 1.2:** Classification of Multiscale methods

## 1.3 Surface Roughness Modelling

It has been observed that surface roughness has a great effect on a variety of physical phenomena related to engineering problems such as wear, contact angle and friction. The characterisation of rough surfaces has been one of the most significant tribological problems of the last century. According to the International Standard for Surface Roughness, there are 16 parameters that are used for the characterisation of rough surface profiles which can be divided in 5 main categories:

- Amplitude parameters
- Spatial Parameters
- Hybrid Parameters
- Functional Parameters

The most common parameters amongst all are $R_a$, $R_q$ and $R_z$ as presented in Table 1.1.

| Parameter | Name | Formula | Description |
|:---:|:---:|:---:|:---:|
| $R_a$ | Arithmetic mean deviation of the roughness profile | $\frac{1}{l}\int_0^l |Z(x)|dx$ | The arithmetic mean of the absolute values of the coordinates $Z(x)$ within a sampling length $l$ |
| $R_q$ | Arithmetical mean deviation of the assessed profile | $\sqrt{\frac{1}{l}\int_0^l |Z^2(x)|dx}$ | The root mean square (RMS) of the coordinates $Z(x)$ within a sampling length $l$ |
| $R_z$ | Maximum roughness height | - | The sum of the heights of the largest peak and the largest depth within a sampling length $l$ |

**Table 1.1:** Common parameters used for the characterisation of roughness profiles

Modelling roughness in the microscopic level is a challenging task as surfaces in such small scales are not continuous but instead they comprise of discrete points which correspond to the atoms placed on a lattice. However, it has been observed that rough surfaces are self-affine, that is they follow a specific pattern regardless the magnification degree ([23], [24]). Therefore, fractal models, which are able to describe the properties of self-affine topographies, have been employed for the representation of rough surface profiles in this research.

## 1.4 Aims & Objectives

The aim of this PhD research is to investigate the effects of surface roughness on nanoscale flows and on the thermodynamic properties of fluids confined in nanochannels. The main objectives are stated below:

- Select a realistic surface roughness model and generate rough geometry profiles representing the nanochannel walls.
- Investigate the effects of surface roughness on the flow behaviour of monatomic liquids.

- Explore the interaction phenomena between the nanochannel walls and the fluid with respect to the rough wall geometry.
- Investigate the wall roughness effect on the fluid viscosity using Non-Equilibrium Molecular Dynamics (NEMD).
- Study the alteration of the thermal resistance of the fluid using Non-Equilibrium Molecular Dynamics with respect to the wall roughness profiles.

## 1.5 Publications

During my PhD research the following journal papers have been written:

- Papanikolaou, Michail, Dimitris Drikakis, and Nikolaos Asproulis. "Molecular dynamics modelling of mechanical properties of polymers for adaptive aerospace structures." International Conferences and Exhibition on Nanotechnologies and Organic Electronics (Nanotexnology 2014): Proceedings of NN14 and ISFOE14. Vol. 1646. AIP Publishing, 2015.
- Papanikolaou, Michail, Michael Frank, and Dimitris Drikakis. "Nanoflow over a fractal surface." Physics of Fluids (1994-present) 28.8 (2016): 082001.

The following journal papers are under preparation for submission:

- Fluid Viscosity dependence on surface roughness amplitude.
- Molecular dynamics simulations of thermal conductance of fluids confined in rough nanochannels.

## 1.6 Thesis Overview

- **Chapter 2** provides a general overview of the current state of the art in Molecular Dynamics Simulations of nanochannel flows. Fundamental information is provided about the methods employed by researchers for investigating the rheological behaviour and the thermodynamic properties of fluids confined in nanochannels. Moreover, a general description of the factors affecting the properties of confined fluids is provided. Special attention is paid to roughness which has been proven to be one of the most dominant factors affecting the aforementioned properties.
- **Chapter 3** illustrates the basic concepts of molecular modelling. First, the commonly used methods for defining the system geometry of a molecular model are described. Then, the typical force fields and interatomic potentials used in molecular simulations are presented. The basic concepts of statistical mechanics are also illustrated and emphasis is placed on the Molecular Dynamics (MD) technique and its implementation. Moreover, the multivariate Weierstrass-Mandelbrot function, later used for the generation of the rough wall geometries, is being presented. In the end of this chapter our Molecular Dynamics model is validated and verified against previous Molecular Dynamics investigations.
- **Chapter 4** presents our results on the effect of the surface roughness amplitude and the wall-fluid interaction parameter on the slip length.

**1.6** Thesis Overview

- **Chapter 5** describes the variation of the fluid shear viscosity across a rough-wall nanochannel depending on the roughness parameter.
- **Chapter 6** illustrates the effects of surface roughness in combination with the wall-fluid interaction on the thermal conductance and the temperature distribution across the nanochannel.
- **Chapter 7** presents the conclusions from chapters 4, 5 and 6. Additionally, some recommendations for future work are provided.

# 2  Literature Review

## 2.1 Introduction

The development of microfabrication processes during the last two decades has made the massive production of micron and sub-micron devices possible. One characteristic example of such devices are MEMS (Micro-Electro-Mechanical-Systems), whose characteristic length can reach values lower than a micrometre. In such length scales, it is very common that Continuum Models such as the Navier-Stokes equations fail to describe micro- or nanochannel flows. Therefore, it is needed to discover the inherent physical laws governing micro- and nanoflows which are characterised by the high surface-to-volume ratio. In this case, surface effects dominate the physical behaviour of a system while properties depending on the volume of the system become less important as described by the "square-cube" law:

$$\frac{p_1(A)}{p_2(V)} \propto \frac{L^2}{L^3} = \frac{1}{L}$$

Eq. 2.1

where $L$ is the characteristic dimension of the device, $P_1$ a property that depends on the area of interaction and $P_2$ a property which depends on the volume.

Since the late 1950s [25], Molecular Dynamics Simulations have been extensively used for modelling nanochannel flows as they offer significant advantages to the researchers. First of all, during the course of a Molecular Dynamics simulation, the motion of atoms is continuous and as a result, accurate results are produced. Moreover, in such simulations no assumptions are being made, while the only inputs to the model are the initial conditions and the interaction parameters between the simulation atoms. Finally, MD simulations provide the user with atomic-level information and with the help of statistical mechanics tools, MD results can be compared and validated against larger scale simulations.

One of the most interesting topics in the literature nowadays is the investigation of the roughness effects on the flow and transport properties of liquids confined in nanochannels by means of Molecular Dynamics simulations. This chapter is devoted to the description of the efforts made by researchers towards this direction and eventually point out any gaps or flaws in the literature.

# 2.2 MD simulations of liquids confined in nanochannels with smooth walls

## 2.2.1 Introduction

Nowadays, the most popular technique for simulating nanochannel flows is Molecular Dynamics. In this section we will present a number of studies where MD has successfully been implemented and some of the key outcomes concerning the nanochannel flow behaviour of liquids and thermodynamic properties.

Initially, researchers focused on simulating smooth nanochannel flows. They used simple fluids, such as argon, while the interaction between the fluid and the wall atoms was modelled via the 12-6 Lennard-Jones potential. The selection of simple fluids was based on the fact that their simulation requires minimum computational resources compared to more complex molecules, such as water or macromolecules. Moreover, the 12-6 Lennard Jones potential produced accurate results and direct comparison to experimental data was feasible. Finally, simple fluids are suitable for extracting density and velocity profiles and investigating the fluid transport properties.

## 2.2.2 Fluid Structure

One of the first steps made was the investigation of the fluid structure in nanochannels which was proven to be layered and not homogeneous as expected. More specifically, strong oscillations of the fluid density are observed in the vicinity of the walls which gradually diminish until the fluid density obtains a constant (bulk) value towards the centre of the nanochannel (Figure 2.1). The existence of density layers in the vicinity of microchannel walls has been verified experimentally as well ([26]) by measuring the thickness of liquid films confined by molecularly smooth surfaces.

There are several factors affecting the fluid atoms localisation inside a nanochannel. It has been shown that the amplitude of the oscillations in the density profiles reduces as the nanochannel wall distance increases [27]. Moreover, Somers and Davis [28] performed Monte Carlo and Molecular Dynamics Simulations and studied the fluid structure in a nanochannel as a function of the channel width. They found that additional but weaker peaks appear in the fluid density profiles towards the centre of the nanochannel as the nanochannel width increases. They also proposed that for channels with width larger than $10\sigma$ the fluid located in the centre of the nanochannel behaves as a bulk fluid, as the density profiles at this area become almost linear.

One more factor affecting the amplitude of the density fluctuations is the wall-fluid interaction strength. For higher values of the wall fluid interaction parameter, the attractive forces between the wall and the fluid atoms increase. Consequently, the fluid atoms approach the wall more closely and higher peaks can be observed in the density profiles ([29], [30]).

7
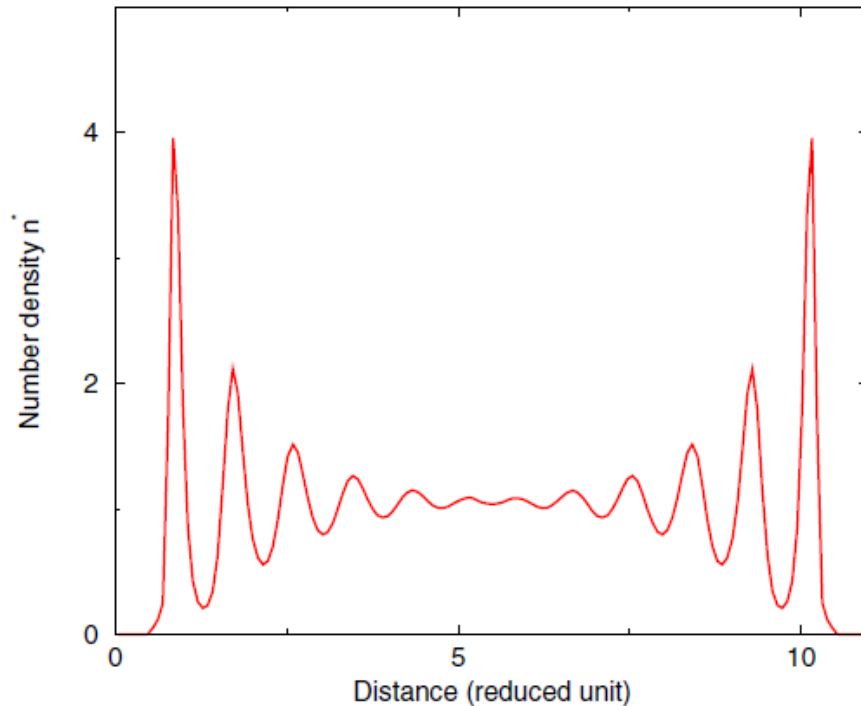
**Figure 2.1:** Oscillations in the density profile of a simple fluid [3]

In most of the Molecular Dynamics simulations about nanochannel flows the wall atoms are located in the sites of a crystal lattice in order to imitate the crystal structure characterising the metals. There are three main ways of placing the wall atoms at these sites: a) wall atoms are fixed to the lattice positions ([31], [32]), b) wall atoms are attached to these sites via a spring potential ([33], [34]) and c) using the Embedded Atom Model (EAM) potential ([35], [36]). It has been proven that the wall structure affects the fluid density profiles. More specifically, for walls with non-oscillating wall atoms (fixed lattice positions) the density peaks are higher compared to walls with vibrating atoms (spring or EAM potential) ([37]). This is because the oscillation of the wall atoms introduces some "distortion" to the interaction forces between the wall and the fluid atoms. Additionally, the effect of the spring stiffness value of the density profiles has been examined by Asproulis and Drikakis [38], who suggested that the spring stiffness constant value mainly influences the value of the first density peak which increases for higher values of the spring constant k.

## 2.2.3 Velocity Profiles and Boundary Slip

Nanochannel flows have been extensively examined by means of Molecular Dynamics Simulations. The most common tool that has been used by researchers in order to investigate the flow behaviour is drawing velocity profiles by averaging the velocities of the fluid atoms over parallel bins. Results have indicated that confined liquids in nanoscale are characterised by a behaviour which deviates from the one described by the Navier Stokes equations, especially when the channel width becomes smaller than 10 liquid diameters [39]. Most of the Molecular Dynamics Simulations studies focus on Poiseuille and Couette nanochannel flows. The former are usually modelled by applying a constant force on each fluid atom towards a

**2.2** MD simulations of liquids confined in nanochannels with smooth walls

particular direction [40], while in the latter case a constant force is applied on one of the nanochannel plates [41].

Similarly to density profiles, velocity profiles at nanoscale are greatly affected by a number of parameters. According to the work of Nagayama and Cheng [42], who performed Molecular Dynamics simulations to study pressure driven nanochannel flows, the flow boundary condition depends strongly on the wall fluid interaction parameters and the driving force. Velocity profiles appear to obtain a parabolic shape for a high wall fluid interaction parameter (hydrophilic case) while the maximum velocity increases with increasing driving force. Moreover, the no-slip boundary condition is satisfied until the point that the driving force exceeds 1.96 pN, where interfacial resistance is overcome (Figure 2.2a). In the hydrophobic wall case, the velocity profiles obtain a plug flow profile, while interfacial slip is apparent in all cases examined. When approaching the centre of the nanochannel, velocity profiles become almost linear and similarly to the hydrophilic case, maximum velocity increases for increasing driving force (Figure 2.2b). As a consequence of the above, the slip velocity increases for higher values of the driving force and for less wettable surfaces. Similar results have been presented in [43] and [44].
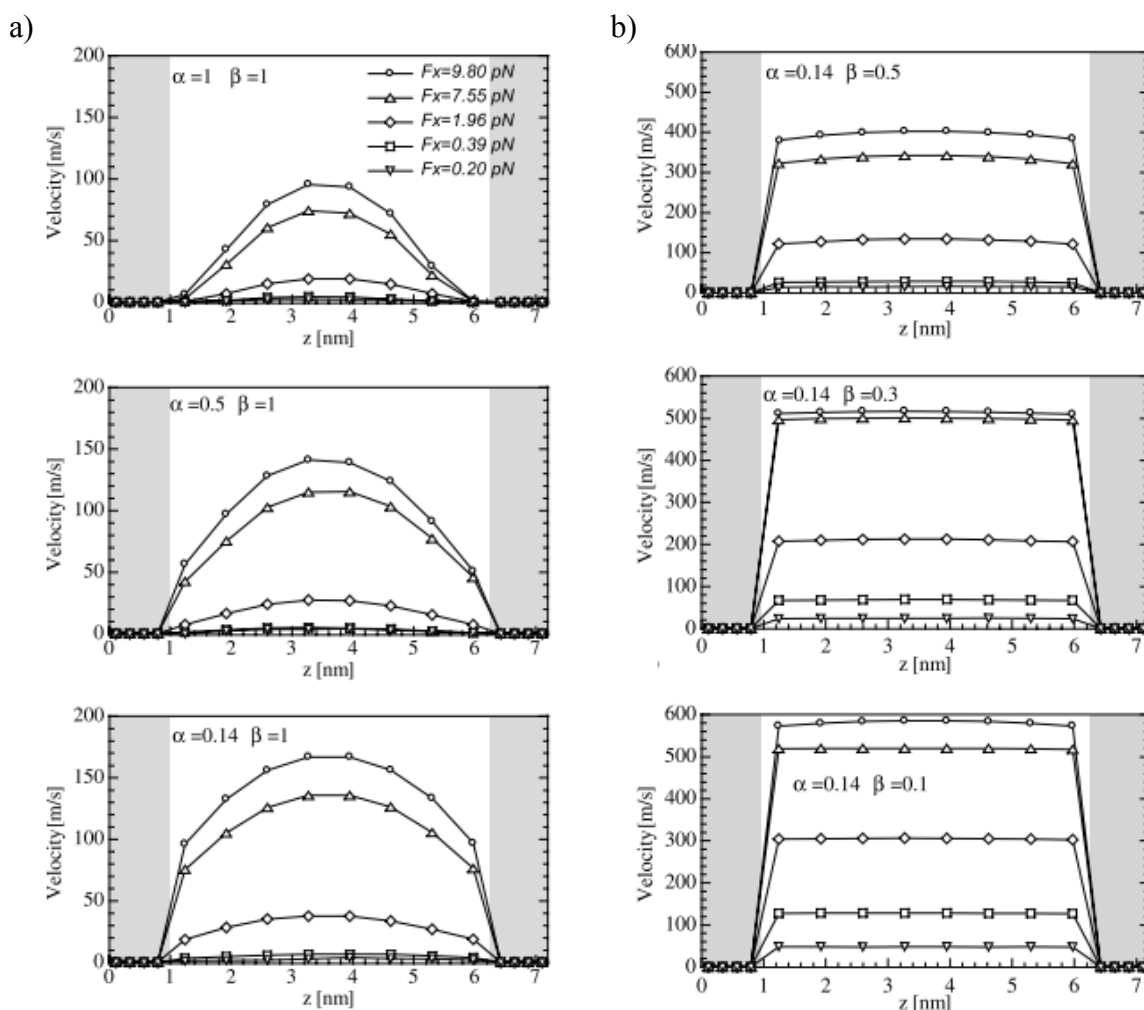


**Figure 2.2:** Velocity profiles for a) hydrophilic and b) hydrophobic nanochannel walls [42]

**2.2** MD simulations of liquids confined in nanochannels with smooth walls

Researchers have also tried to determine the boundary slip condition via Molecular Dynamics simulations. One of the first attempts was made by Thompson and Troian [45]. Their model consisted of a Newtonian liquid confined by two solid walls. A Couette flow was developed by imposing a constant velocity on the upper wall of their model. They obtained the velocity profiles for various values of the shear rate and plotted the slip length as a function of the shear rate. They also proposed an analytical relationship in order to describe the aforementioned curve:

$$L_s = L_s^0 \left(1 - \frac{\dot{\gamma}}{\dot{\gamma}_c}\right)^{-\alpha}$$

Eq. 2.2

where $L_s$ is the slip length, $L_s^0$ its limiting asymptotic value, $\dot{\gamma}$ its limiting asymptotic value and $\dot{\gamma}_c$ corresponds to the point at which the walls can no longer impose resistance to the flow. The constant $\alpha$ equal to $1/2$.

As pointed out by Asproulis and Drikakis [46], the flow behaviour of liquids, and more specifically the slip length, can be affected by the mass of the wall particles $m_w$ and the stiffness constant $k$ of the spring used to place the wall atoms in lattice positions. These two variables were combined using the oscillating frequency:

$$\omega = \sqrt{\frac{\kappa}{m_w}}$$

Eq. 2.3

Their results showed that the slip length increases linearly with the oscillating frequency until it reaches a critical value. After this point, it diminishes towards an asymptotic value. In this study, a fifth-order polynomial master curve was proposed to describe the effect of the oscillating frequency of the wall atoms on the slip length:

$$\frac{L_s}{L_{s,max}} = a + b\frac{\omega}{\omega_{max}} + \cdots + f\left(\frac{\omega}{\omega_{max}}\right)^5$$

Eq. 2.4

where $L_{s,max}$ is the maximum value of the slip length in a series of simulations conducted using the same interaction parameters, wall mass, driving force but variable spring stiffness constant; $\omega_{max}$ is the oscillating frequency corresponding to maximum value of the slip length and $a = -0.55, b = 4.27, c = -4.46, d = 2.21, e = -0.53$, and $f = -0.05$ are constants.

A detailed study regarding the parameters affecting the slip length in nanochannel flows has been conducted by Voronov and Papavassiliou [47] who investigated the dependency of the slip length on a) the relative energy $\varepsilon_r$, b) the relative size $\sigma_r$, c) temperature and d) the wall velocity. Their model consisted of argon confined by graphitelike hexagonal-lattice walls and a Couette flow was developed by imposing a constant speed on the upper wall. As far as the relative energy is considered they found that the slip length diminishes almost exponentially as $\varepsilon_r$ increases. On the contrary, the slip length was found to be dependent and exponentially increasing with $\sigma_r$. The results also revealed that the temperature effect on the slip length is relatively small for the temperature range examined $(83.3 - 100 \, K)$. Finally, it was shown that slip length obtains higher values for increased wall velocity.

Studies have not been limited to monatomic fluids but polymer rheology has attracted the attention of researchers as well. Priezjev and Troian [48] performed Molecular Dynamics Simulations to study the planar shear flow of polymers focusing on the slip response of N-mer chains. Their model was comprised of polymer chains with variable length, confined by two solid walls. They developed a Couette flow by applying a constant velocity on the upper plate of the nanochannel and calculated the velocity profiles for varying chain length and shear rate. They produced an illuminating plot to describe the slip length as a function of the chain length and the shear rate (Figure 2.3). It is shown that for low shear rates the slip length is almost constant while for higher shear rates the slip length increases nonlinearly. They attributed this sudden increase to the fact that beyond a critical value of the shear rate the wall can no longer impose additional resistance to the fluid flow.
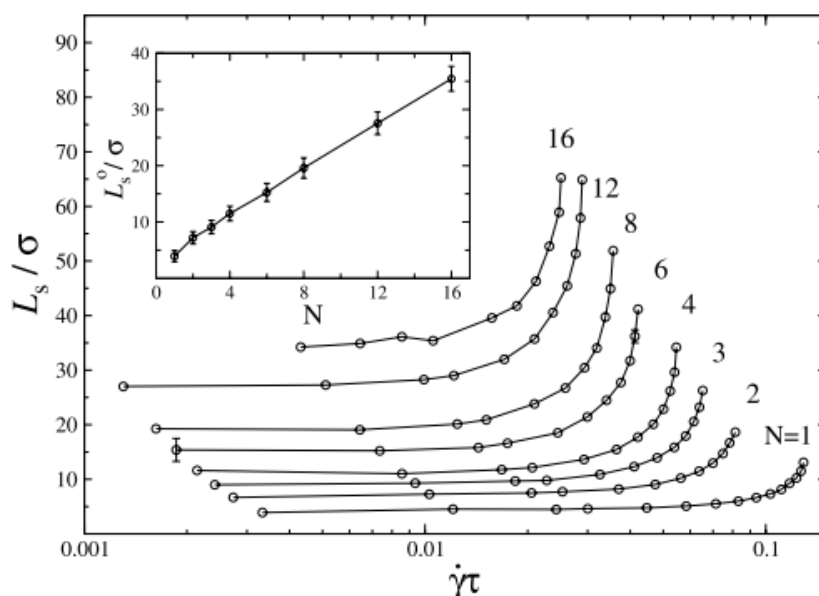


**Figure 2.3:** Slip length vs. shear rate with chain lengths N=1-16 [48]

## 2.2.4 Viscosity

Molecular Dynamics Simulations have been extensively used for the estimation of the transport coefficients of liquids. Several methods have been implemented for the calculation of the fluid shear viscosity via Molecular Dynamics Simulations. The most popular of them are listed below (more details can be found in Chapter 3):

1. **Equilibrium Molecular Dynamics:** according to Allen and Tildesley [49] the shear viscosity can be estimated by the following relationship, which is a form of the Green Kubo relations:

$$\eta_{shear} = \frac{V}{k_b T} \int_0^\infty \langle P_{xy}(t) \cdot P_{xy}(0) \rangle \, dt \qquad \text{Eq. 2.5}$$

**2.2** MD simulations of liquids confined in nanochannels with smooth walls

where $V$ is the volume of the liquid, $T$ is the temperature, $k_b$ the Boltzmann constant and $P_{xy}$ an off-diagonal term of the stress tensor with $x \neq y$.

2. **Non Equilibrium Molecular Dynamics simulations:** A shear velocity profile is imposed and the shear viscosity $\eta$ can be then calculated via Eq. 2.6:

$$\eta_{shear} = \frac{P_{xy}}{\dot{\gamma}} \qquad \text{Eq. 2.6}$$

where $\dot{\gamma} = \frac{\partial u_x}{\partial y}$ is the shear rate and $P_{xy}$ an off-diagonal term of the stress tensor. Both the velocity and pressure profiles are being monitored during the evolution of the simulation after the point when the system has reached equilibrium.

One of the first attempts for the estimation of the shear viscosity was conducted in 1973 by Levesque et al. [50] who used the Green Kubo relations. The computing power of that time allowed them to include only 864 particles in their system and their simulation corresponded to 10 ns of real time in the case of argon. This study revealed that the implementation of the Green Kubo formula for the estimation of the shear viscosity is not a trivial issue, as the computational cost was relatively high and the results were not in agreement with experiments. It was therefore suggested that NEMD should preferably be used for the estimation of transport coefficients. NEMD are based on measuring the steady state response to a perturbation and the inaccuracy induced by the long-time behaviour of the correlation functions is eliminated. It has to be noted that NEMD are very similar to the procedure followed when conducting experiments.

One of the first NEMD methods for measuring the shear viscosity is the periodic perturbation method. Gosling et al. [51] developed an oscillatory velocity profile by applying an external force on each particle at each timestep. The shear viscosity $\eta$ could then be measured using the following relationship:

$$\langle u_x(r_y) \rangle \approx \left(\frac{\rho}{k^2\eta}\right) F \cos(\boldsymbol{k}r_y) \qquad \text{Eq. 2.7}$$

where $F$ is the maximum value of the external force, $\boldsymbol{k} = (0, k, 0) = \left(0, \frac{2\pi n}{L}, 0\right)$ a wavevector, and $\langle u_x(r_y) \rangle$ the mean velocity of a particle at the $r_y$ coordinate. This method was proven to be less computationally expensive compared to the equilibrium Molecular Dynamics method. One advantage of this method is that periodic boundary conditions are maintained. Its most important disadvantage is that the value of the viscosity is dependent on the wavevector $\boldsymbol{k}$: $\boldsymbol{\eta}$ approaches its value as $\boldsymbol{k} \to \boldsymbol{0}$. Consequently, in order to have a correct estimation of the viscosity, several different k-perturbations should be examined and an extrapolation to zero should be made.

In order to overcome the difficulties stated in the previous paragraph, techniques employing modification of the boundary conditions were proposed. Lees and Edwards [52] modified the periodic boundary conditions in order to maintain their system under a shearing stress in steady state. They considered a simulation box (A) surrounded by two images of itself

12

## 2.2 MD simulations of liquids confined in nanochannels with smooth walls

(B & C) in the yz-plane moving in the x-direction with opposite velocities ($V_d$ and $-V_d$) respectively as shown in Figure 2.4. As a result, a linear velocity profile was generated with zero velocity at the midpoint of the system A. When the system reached equilibrium, the shear viscosity was calculated from the non-equilibrium average of the off-diagonal component of the pressure tensor $P_{ij}$ in the steady state as follows:

$$P_{ij} = \eta \frac{\partial V_i}{\partial x_j}$$

Eq. 2.8
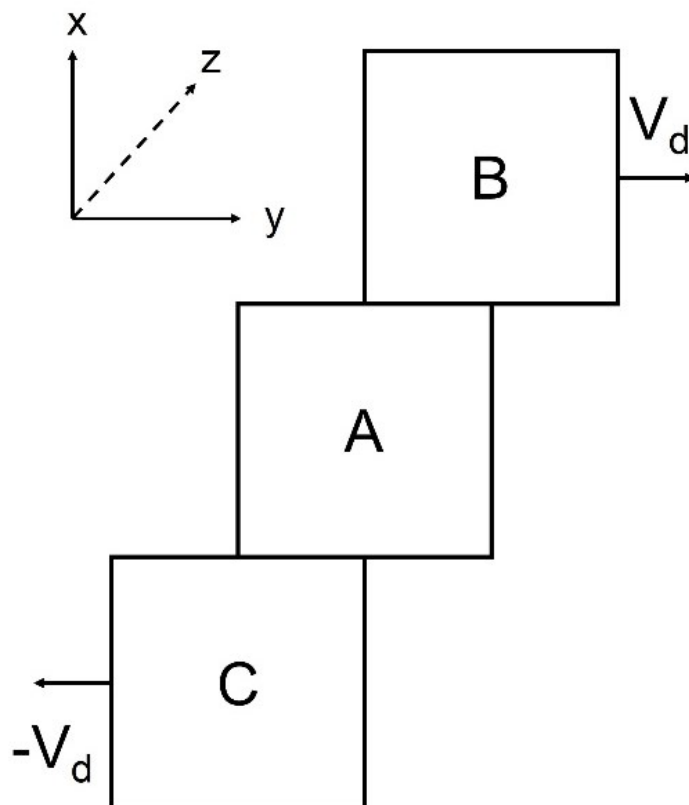


**Figure 2.4:** Shear boundary conditions

A similar approach was proposed by Ashurst and Hoover ([53], [54]). In these investigations the fluid was sheared by applying external forces on two fluid-wall regions and as a result a Couette flow was developed. They also used velocity scaling in order to maintain a constant temperature at the wall region (reservoir method). This was one of the first attempts to perform Molecular Dynamics at constant temperature instead of constant energy. Despite some disadvantages of the reservoir method, such as the use of fluid atoms for the representation of the nanochannel walls, the results produced were in agreement with experimental data and with other NEMD simulations.

One of the most efficient NEMD techniques for estimating the shear viscosity is the SLLOD algorithm [55] which has yielded accurate results for high shear rates and non-Newtonian regimes. The SLLOD algorithm is described by the following equations of motion:

**2.2** MD simulations of liquids confined in nanochannels with smooth walls

$$\frac{d\boldsymbol{r}_i}{dt} = \frac{\boldsymbol{p}_i}{m_i} + \boldsymbol{r}_i \cdot \nabla\boldsymbol{u}$$

$$\frac{d\boldsymbol{p}_i}{dt} = \boldsymbol{F}_i - \boldsymbol{p}_i \cdot \nabla\boldsymbol{u} - a\boldsymbol{p}_i$$

Eq. 2.9

where $\boldsymbol{r}$ and $\boldsymbol{q}$ are the position and momentum vectors respectively, $\boldsymbol{F}_i$ is the fore applied on the particle $\boldsymbol{i}$ and $\boldsymbol{u}$ is the velocity vector. The SLLOD algorithm is implemented in combination with the Lees and Edwards [52] boundary conditions and the shear viscosity can be estimated using Eq. 2.6.

The aforementioned methods do not account for density variations induced by the wall confinement. Todd and Evans [56] studied the Poiseuille flow in nanochannels and suggested that the shear viscosity varies with the fourth power of z (direction normal to the nanochannel walls). Bitsanis et al. [57] proposed the Local Average Density Model (LADM) where the shear viscosity is not dependent on z but on the local average density. The local average density can be calculated by averaging the local density over a sphere centred at a position $\boldsymbol{r}$. LADM was found to predict accurately velocity profiles, effective viscosities and corresponding shear stresses.
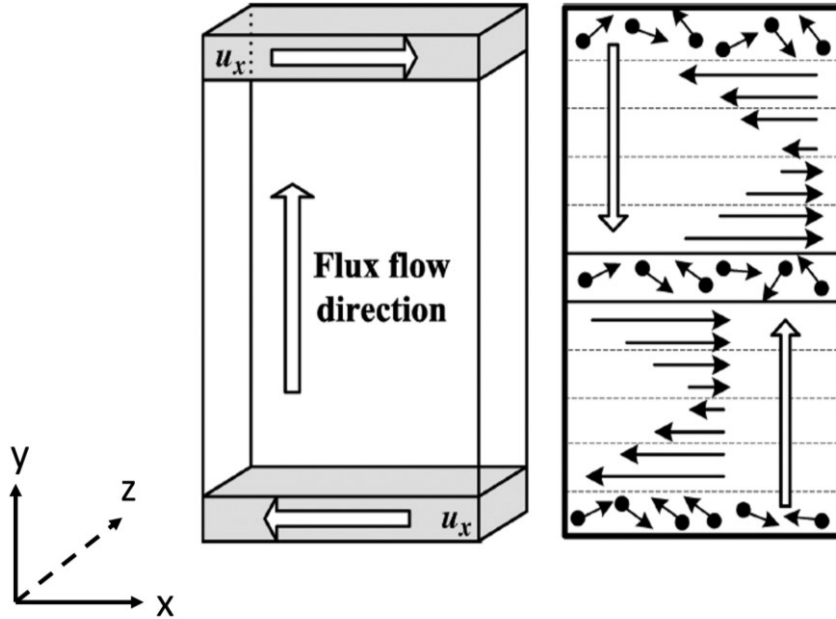


**Figure 2.5:** Momentum exchange in RNEMD [58]

An alternative method for calculating the shear viscosity has been proposed by Müller-Plathe ([59], [60]), which unlike the NEMD and the EMD methods does not suffer from any limitations and has been proven to be very efficient in terms of performance and accuracy. The Müller-Plathe algorithm is called a Non-Equilibrium Molecular Dynamics (RNEMD) method as, contrary to the NEMD methods, a momentum flux is nonphysically imposed on the system instead of a shear velocity. In this case, the shear velocity profile is the response of the system. In order to impose a momentum flux, the simulation box is divided into N bins along the y-direction (Figure 2.5). Then, the momenta of the two particles $\Delta P$ located in the lower and the

middle bin having the maximum velocity in the x and –x direction ($V_{x,max}$ and $-V_{x,max}$ respectively) are exchanged. This procedure is repeated every N timesteps and as a result a velocity profile is developed while the total amount of momentum exchanged is equal to $P_{RNEMD} = \sum \Delta P$. In the upper part of the simulation box momentum is transferred as well, as a response to the momentum flux imposed on the lower part. Finally, the shear viscosity can be calculated using the following relationship:

$$\frac{P_{RNEMD}}{2S\Delta t} = -\mu \frac{\partial u_x}{\partial y}$$

<div align="right">Eq. 2.10</div>

where S is the cross-sectional area of the simulation box. Moreover it has to be noted that besides the velocity profiles, a temperature profile is also imposed through the momentum exchange. Consequently, the Müller-Plathe algorithm can be used for the estimation of the thermal conductivity [61].

## 2.2.5 Interfacial Thermal resistance

One of the topics that have attracted the attention of researchers is the interfacial thermal resistance (ITR) at a solid-liquid interface. Peter Kapitza was the first who suggested that there is a temperature jump at the interface between a solid and a liquid surface [62]. This is because energy is scattered at this region as phonons, which are the main energy carriers, scatter at this region due to the different vibrational properties of the two materials. The investigation of the interfacial resistance has been based on two models: a) the Acoustic Mismatch Model (AMM) and b) the Diffusive Mismatch Model (DMM) [63]. However, the AMM and DMM models do not account for the bonding between the two materials at the interface but only their bulk properties are being taken into consideration. This issue can be addressed with the help of Molecular Dynamics Simulations which have been proven to be very useful in determining the effects of the interaction strength between the solid and the liquid atoms on the ITR.

The first Molecular Dynamics Simulation showing that there is a temperature jump at the interface between two different materials was performed by Maiti et al. [64], who studied the thermal conductance between two heterogeneous solid crystals. Later on, researchers focused on the various parameters affecting the thermal resistance. The first parameter examined was the interaction strength between a solid and a liquid. Barrat and Chiaruttini [65] estimated the Kapitza length as a function of the liquid-solid interaction parameter. For this purpose, they used the Kapitza length $L_k$, which is a measure for the interfacial thermal resistance and can be estimated using the following relationship:

**2.2** MD simulations of liquids confined in nanochannels with smooth walls

$$\Delta T = L_k \frac{\partial T}{\partial n}\bigg|_{liquid} \qquad \text{Eq. 2.11}$$

where $\Delta T$ is the temperature jump at the interface and $\frac{\partial T}{\partial n}\big|_{liquid}$ is the thermal gradient which can be obtained by the temperature profile. Their results showed that the ITR is dependent on the wetting properties of the surface and the Kapitza length is a decreasing function of the wall fluid interaction as shown in Figure 2.6.
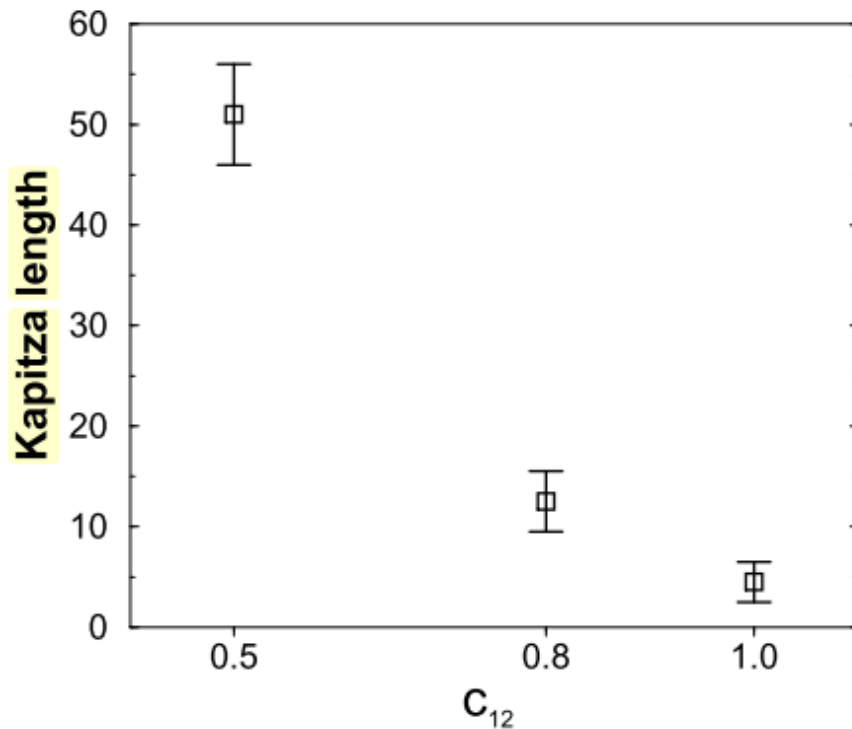


**Figure 2.6:** Kapitza length as a function of the interaction parameter $c_{12}$ [65]

Similar results have been obtained by Xue et al. [66] who additionally suggested that there are two regimes in the function describing the dependence of the interfacial thermal resistance on the wetting properties: a) an exponential dependence in the case of non-wetting liquids and b) a power law dependence in the case of wetting liquids.

Molecular Dynamics Simulations have also shown that the Kapitza length also strongly depends on the wall bonding stiffness [67]. It has been shown that increased wall bonding stiffness leads to higher temperature jumps because momentum transfer is prohibited. Liu et al. [68] investigated the effect of the external driving force on the thermal resistance in a Poiseuille flow. They showed that the thermal resistance decreases monotonically as the external driving force increases. They attributed this phenomenon to the breakage of the wall-

fluid binding when the driving force becomes very large. On the contrary, when the driving force is small the first liquid layer is adsorbed by the wall allowing for enhanced thermal conductance. Balasubramanian and Banerjee [69] performed NEMD Simulations in a system consisted of liquid-vapour Argon mixtures in contact with Fe walls. They found that thermal resistance is dependent on the wall temperature and that it decreases as the wall temperature increases. Finally they proposed that the ITR is proportional to $T_w^{-4.8}$ as depicted in Figure 2.7. Besides the wall temperature, Murad and Puri [70] showed that one more factor affecting the Kapitza resistance is the heat flux. Their results indicated that the temperature jump is inversely proportional to the heat flux and proportional to the term $\left(\frac{Q'}{A}\right)^{0.34}$ as shown in Figure 2.8.
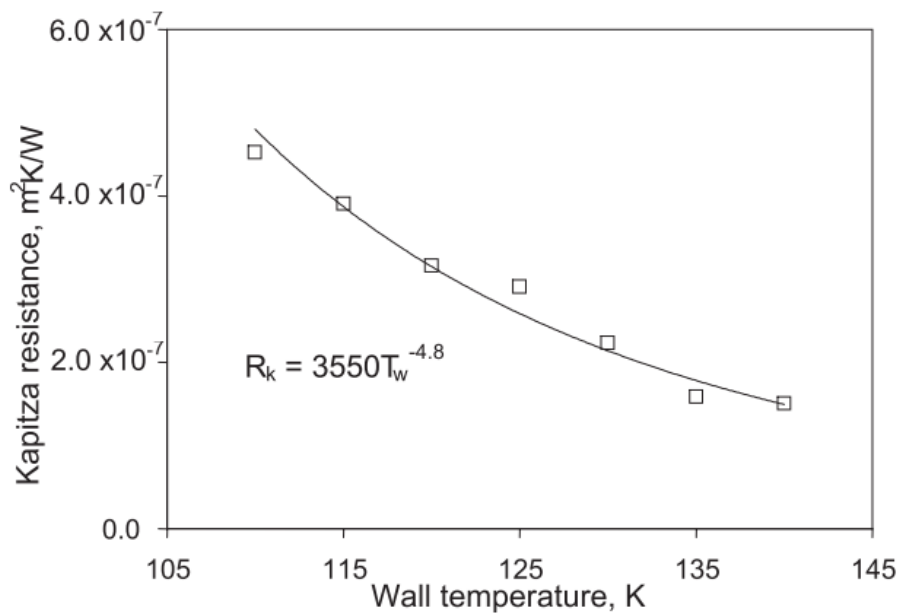


**Figure 2.7:** Kapitza resistance as a function of the wall temperature [69]

The initial step of the procedure followed in Molecular Dynamics Simulations in order to measure the ITR is to impose a temperature difference by thermostating the atoms of the two nanochannel walls. The most common way of controlling a system's temperature is by applying a Langevin, a Nose Hoover thermostat or even by velocity rescaling as it will be discussed in Chapter 3. However, a temperature jump between the regions on which a thermostat is applied and thermostat-free regions has been reported in homogeneous systems such as solids [64]. This temperature jump is attributed to the fact that the force applied by the thermostat on the particles (in order to maintain the system at the desired temperature) de-correlates their motion at the interface of the regions mentioned in the preceding lines. Because

**2.2** MD simulations of liquids confined in nanochannels with smooth walls

of this phenomenon thermal conductivity is underestimated and an artificial thermal resistance is imposed. Barisik and Beskok [71] investigated this phenomenon at the interface between a solid and a liquid considering three types of boundary treatment: a) a thermostat is applied on all the wall layers, b) a thermostat is applied on a few only wall layers and c) energy is injected and removed from the wall layers. Their results indicated that thermostats should only be applied on a few layers of the nanochannels walls, several layers away from the wall-fluid interface or by adding and removing energy from the wall layers in order to reproduce realistic results.
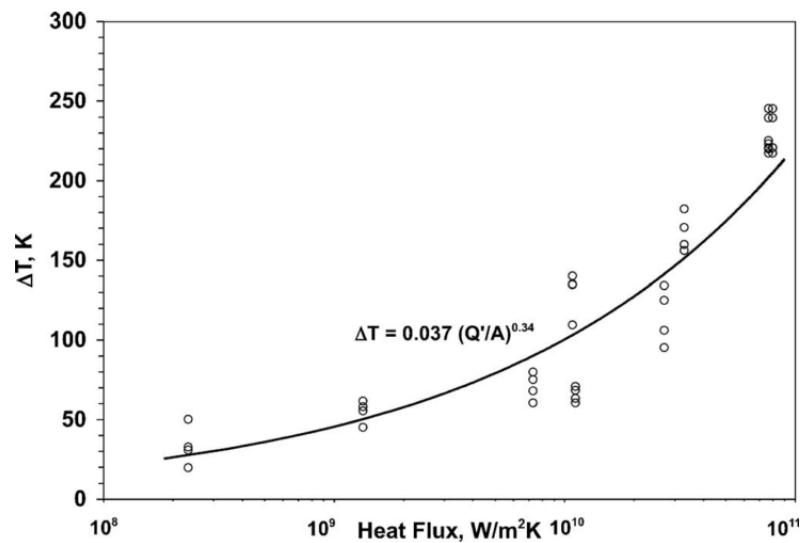


**Figure 2.8:** Temperature jump as a function of the Heat Flux [70]

Shi, Barisik and Beskok [36] used the thermostating method described above for the characterisation of the ITR as a function of temperature. They created a very realistic Molecular Dynamics model which was comprised of silver and graphite walls and liquid argon molecules. The interaction between the wall atoms was modelled using the EAM (for silver) and the AIREBO (for graphite) potentials and the interaction between the argon and the silicon atoms was described using the 12-6 Lennard Jones potential. They developed mathematical models to estimate the Kapitza length as a function of the wall temperature and utilised them as boundary conditions for the solution of the heat conduction equation to predict the temperature profile in the nanochannel. Their theoretical model was found to be in a very good agreement with the Molecular Dynamics simulations for both silver and graphite walls.

Molecular Dynamics studies on interfacial thermal resistance have not been limited to monatomic fluids but more complex liquids have been examined as well. Barisik and Beskok

[72] studied the heat transport through a water silicon interface. In order to describe the interaction between the water molecules they used the SPC/E model [73] and the interaction between the silicon and the water atoms was modelled using the Lorentz-Berthelot mixing rule:

$$\sigma_{Si-O} = \frac{\sigma_{Si-Si} + \sigma_{O-O}}{2}$$

<div align="right">Eq. 2.12</div>

$$\varepsilon_{Si-O} = \sqrt{\varepsilon_{Si-Si} \times \varepsilon_{O-O}}$$

They also estimated the Kapitza length as a function of temperature for both the hot and the cold wall surfaces noticing no significant difference between the two (Figure 2.9). Their estimation of the Kapitza length ($L_k \approx 9\ nm$) was found to be in a very good agreement with experimental results for hydrophobic surfaces [74]
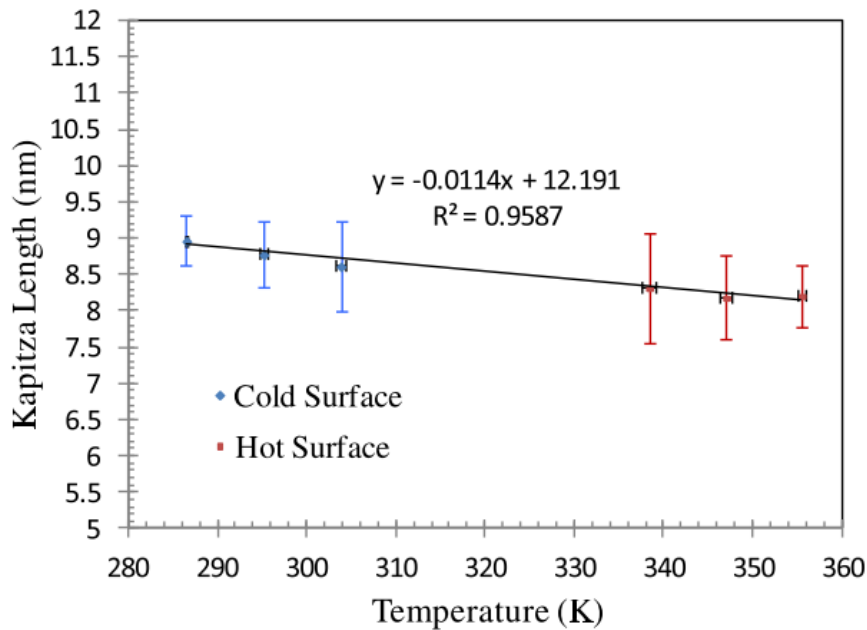


**Figure 2.9:** Kapitza Length as a function of Temperature [74]

# 2.3 MD simulations of liquids confined in nanochannels with rough walls

## 2.3.1 Introduction

In the previous chapter, the investigation of flows in smooth nanochannels by means of Molecular Dynamics Simulations has been discussed. In this chapter we will present the current state of the art in the MD simulations conducted for rough nanochannels and the wall roughness effects on a) the fluid structure in the vicinity of the rough walls, b) the velocity profiles and

the slip length, c) the fluid viscosity and d) the thermal resistance. As it will be presented in the following paragraphs, the nanochannel wall topography is one of the most important factors affecting the fluid properties.

The first attempts to quantify the effects of roughness on the flow behaviour and the properties of confined liquids were experimental. In 1937 Nikuradse [75] performed a sequence of experiments on the water flow in smooth and rough pipes and his results indicated that neither the friction factor nor the laminar-to-turbulent transition were affected by roughness. However, one of the first attempts to model the effects of roughness on microchannel flows was made by Richardson [76] who studied the shear flow over a periodically grooved surface and revealed that the no-slip boundary condition in macroscale is due to the existence of surface roughness in micro- and nanoscale. A series of experiments conducted in the late 80's and 90's showed that the conventional laminar theory for rough pipes is not valid in micro- and nanoscale. The main conclusions drawn from the later work in microflows in rough nanochannels are that heat transfer is enhanced and there is an increase in the friction factor and an early transition from laminar to turbulent flow [77].

Despite the fact that experiments proved that the roughness effects in the micro- and nanoscale are dominant, a clear explanation of the phenomena taking place at such small sales were not provided and the roughness effects on the flow behaviour were not fully quantified. Therefore, researchers utilised Molecular Dynamics Simulations which can provide reliable models and an insight into the dynamics and thermodynamics of molecules at the nanoscale.

## 2.3.2 Fluid Structure

One of the first attempts to study the fluid structure in rough nanochannels via Molecular Dynamics Simulations was made by Gao et al. [78]. Their model consisted of alkane molecules confined by two gold walls. In order to create the rough wall topography they prepared two slabs made of 8 layers of gold (Au) atoms in the z-direction each, while periodic boundary conditions were applied in the x and y directions. The solid particles were placed in a FCC lattice with the (111) plane being parallel to the z-axis and the interaction between the wall atoms was modelled using the EAM potential. Then, the slabs were heated up to 1100 K and as a result a few atoms of the top layers left their initial lattice positions generating rough walls (Figure 2.10). Finally, the system was equilibrated back at 350 K.
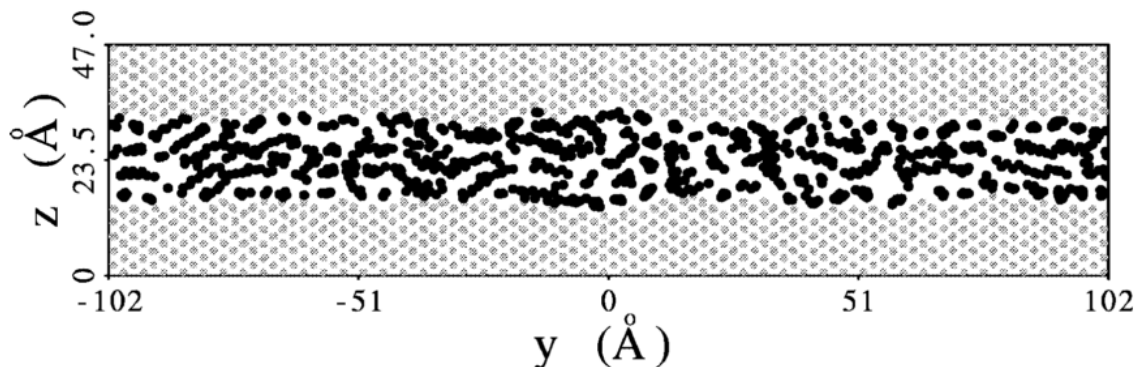


**Figure 2.10:** Schematic representation of the rough wall nanochannel of Gao et al. [78]

**2.3** MD simulations of liquids confined in nanochannels with rough walls

Gao et al. compared the density profiles for the smooth and rough wall nanochannels for different average nanochannel widths $\overline{D}$. They found that the density layering is more distinct and sharp in the case of smooth nanochannel walls for all the $\overline{D}$ values examined. Moreover, they showed that the density in the centre of the nanochannel becomes more homogeneous as the channel width increases (Figure 2.11).
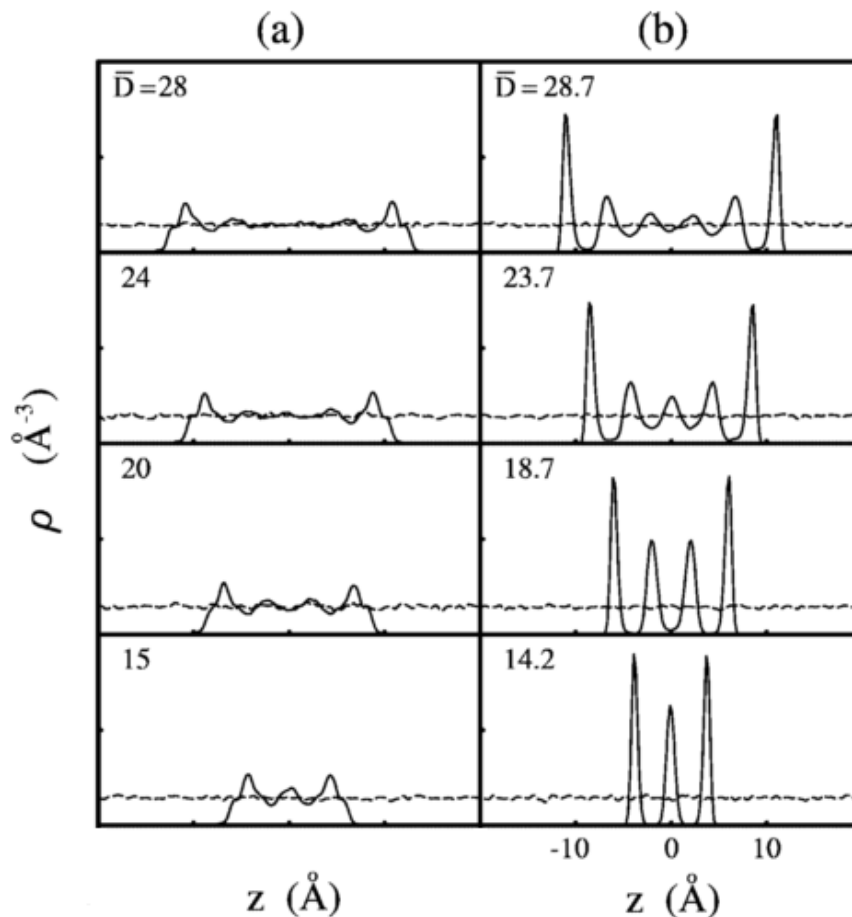


**Figure 2.11:** Density profiles of (a) rough wall and (b) smooth wall nanochannels for various channel widths [78]

Jabbarzadeh et al. [79] investigated the effect of wall roughness on the rheological properties of hexadecane. In order to generate rough walls they displaced the wall atoms which were placed on the sites of a Body Centred Cubic (BCC) lattice in the z-direction by $\Delta z$:

$$\Delta z = A \sin\left(\frac{2\pi x}{P}\right)$$

Eq. 2.13

where $A$ is the roughness amplitude and $P$ the period of the sinusoidal wall. They also investigated the fluid localisation inside the nanochannel and found that the fluid layering phenomenon is more intense for lower values of $P$. Moreover, they suggested that for higher roughness amplitude the density peaks in the vicinity of the walls move towards the centre of the nanochannel and the density in the nanochannel centre increases. Galea and Attard [80] modelled atomic roughness as a function of size and distance between the solid atoms placed

**2.3** MD simulations of liquids confined in nanochannels with rough walls

on a Face Centred Cubic lattice (FCC) with a constant packing fraction. Similarly to the previously reported results, strongest fluid layering in the vicinity of the nanochannel walls was observed in the smooth wall case.

Chen et al. [81] performed Molecular Dynamics simulations to study the fluid flow in rough nanochannels. They modelled the rough wall surface profiles using the 2-dimensional Weierstrass-Mandelbrot function [82]:

$$R(x) = G^{D-1} \sum_{n=n_1}^{\infty} \frac{\cos(2\pi\gamma^n x)}{\gamma^{(2-D)n}}$$

Eq. 2.14

where $1 < D < 2$ is the fractal dimension, $G$ is the roughness amplitude and $\gamma > 1$ the scaling parameter. Their walls were generated by adding and subtracting atoms above and below a centreline. In this way, a top surface profile following the $R(x)$ function was created. Their density profiles revealed that, under the presence of fractal roughness, density increases gradually as departing from the wall region. Moreover, they suggested that density oscillations decrease for higher values of the average roughness height $\delta$ or the fractal dimension $D$ as depicted in Figure 2.12.
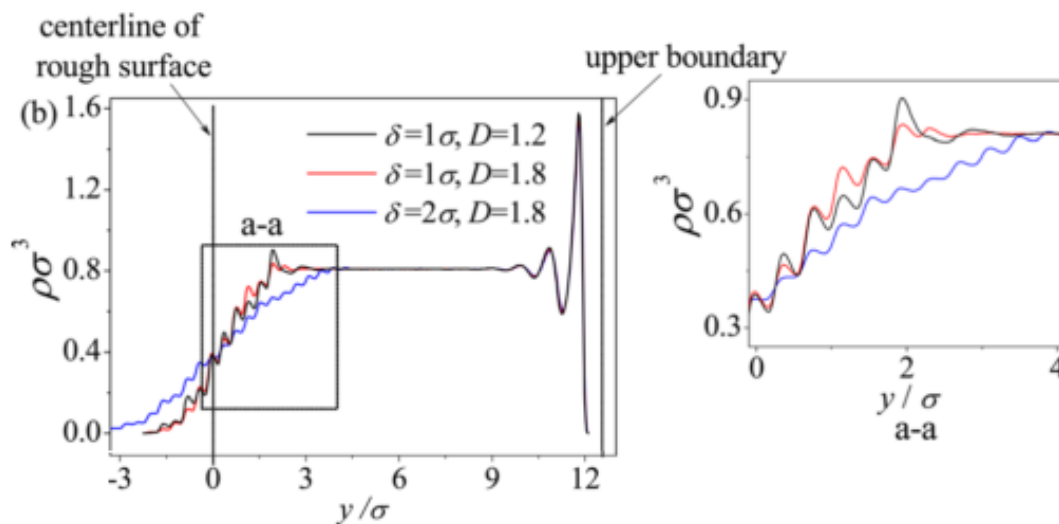


**Figure 2.12:** Density profiles for various values of the average roughness height δ and the fractal dimension D [81]

A clearer understanding of the fluid atoms localisation in rough nanochannels has been given by Sofos et al. [83]. Their model was comprised of liquid argon confined by two krypton walls. The lower wall was smooth while the upper wall was rough having periodically spaced rectangular cavities. They performed simulations for five different values of the roughness period $p$ ($p = 0, 1, 2, 3, 6$) and estimated the corresponding two dimensional density profiles as shown in Figure 2.13. It can be seen that the fluid density is increased inside the wall cavities. The authors attributed this behaviour to the increased trapping time of the liquid atoms inside the wall cavities. It can also be observed that the trapping phenomenon becomes more pronounced for higher values of the roughness period.

a)



b)
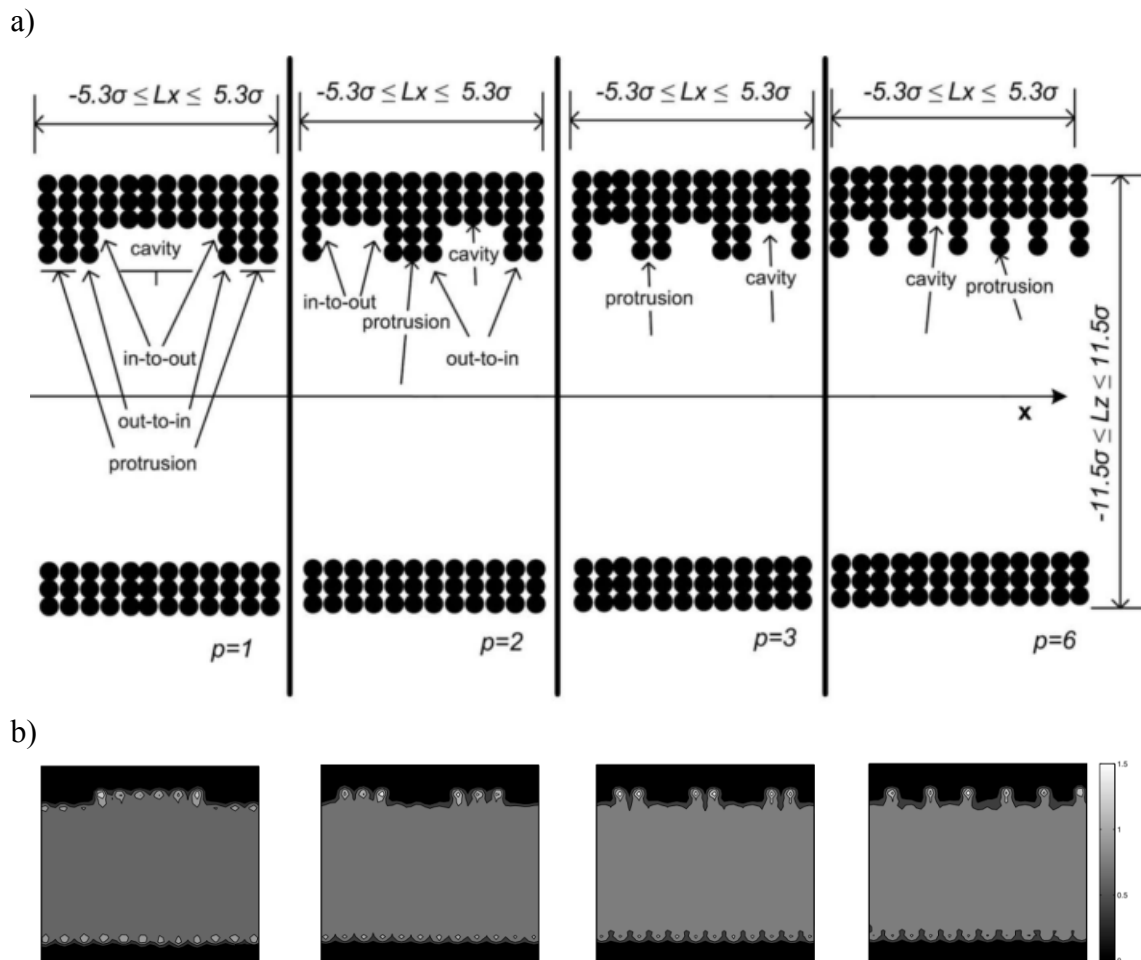


**Figure 2.13:** (a) Schematic representation of periodic protrusions and (b) corresponding 2-dimensional density profiles

## 2.3.3 Velocity Profiles and Boundary Slip

The influence of surface roughness on nanochannel flows has been investigated by means of Molecular Dynamics Simulations during the last two decades. Jabbarzadeh et al. [79] investigated the Couette shear flow of hexadecane in nanochannels with sinusoidal walls (Figure 2.10). The estimated velocity profiles revealed that the slip length depends on a) the roughness amplitude $A$, b) the roughness period $P$ and c) the length of the hexadecane chains. More specifically, it was found that the slip length increases for higher values of the roughness amplitude or the roughness period. This is because both of the aforementioned parameters contribute to the increased trapping time of the hexadecane molecules in the wall valleys and as a consequence the momentum of the wall is effectively transferred towards the nanochannel centre. Additionally, enhanced slip was observed for longer hexadecane chains. The authors attributed this observation to the fact that as the chain length increases (and while the roughness amplitude and period remain constant) it is more difficult for macromolecules to get trapped between the peaks and the valleys of the rough wall topography.

Another early Molecular Dynamics study about the roughness effects on the slip length [80] surprisingly revealed that the slip length is a nonmonotonic function of the interatomic spacing $m_r$, which in this case was used as a measure of the wall roughness (rougher walls

correspond to higher values of $m_r$). The authors found that there is a stick boundary condition for $0.7 < m_r < 1.3$. Outside this region (as the walls become rougher or smoother) they suggested that the boundary condition is one of slip. They attributed this complicated behaviour to the resonances taking place at the liquid-solid interface.

Priezjev and Troian [84] performed Molecular Dynamics simulations of Couette flows in nanochannels for the investigation of the wall roughness effects on the slip behaviour at patterned solid-liquid interfaces. The upper nanochannel wall was smooth while the roughness model they used for the lower wall is described by Eq. 2.13. They plotted the slip length as a function of the stretching parameter $s = \frac{\langle C \rangle}{\lambda}$ (where $C$ is the contour length and $\lambda$ the roughness wavelength of the sinusoidal roughness profile), which was used to control the wall density, and the slope parameter $ka$ (where $k = \frac{2\pi}{\lambda}$ is the wavenumber and $a$ the amplitude of the roughness profile) as illustrated in Figure 2.14. It can be seen that the slip length decreases monotonically as $s$ increases because particles are increasingly trapped between the wall cavities when the spacing between the wall atoms becomes larger. Moreover, the no slip condition is valid for $s > 1.3$. Finally, it is shown that for smaller values of the wavelength (higher values of the slope parameter $ka$) the slip length decreases monotonically. The MD results of this study were found to be in a good agreement with the corresponding continuum solutions for large values of the wavelength and small values of the slope parameter. Consistent results have also be presented by Sofos and Karakasidis [83] who plotted the slip length as a function of the roughness period.
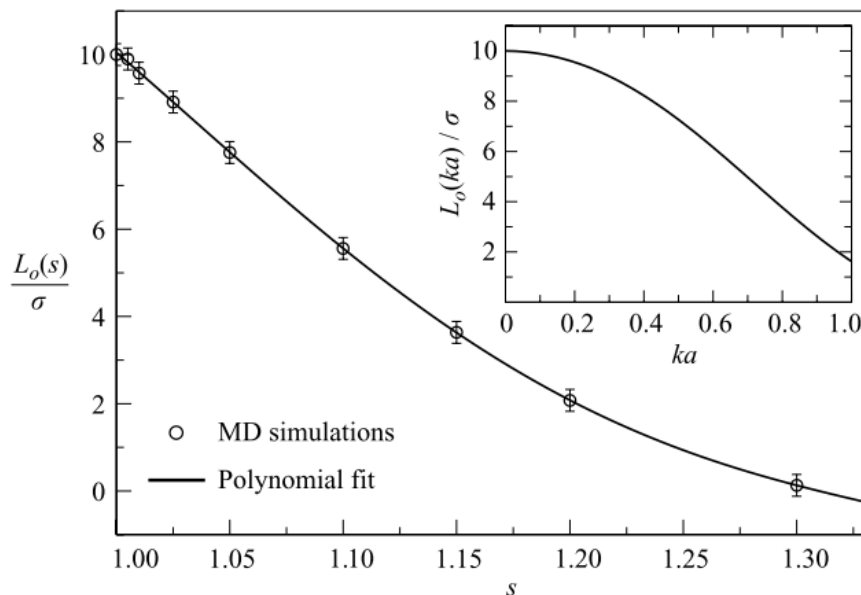


**Figure 2.14:** Slip length $L_0$ as a function of s and ka [84]

Niavarani and Priezjev [85] implemented a variation of the model described in the previous paragraph in order to study the rheological behaviour of polymers past sinusoidal rough walls. Instead of a simple fluid they used polymer chains ($N = 20$) with their monomers interacting with the Finite Extensible Nonlinear Elastic (FENE) potential [86]. They plotted

the slip length as a function of the wavenumber $ka$ for various values of the roughness wavelength $\lambda$ and compared the MD results with the solutions of the Navier-Stokes equations. Their results were found to be in agreement with [84] and it can be observed that the continuum results overestimate the slip length values estimated by the MD simulations. Moreover, the divergence between the two solutions is more pronounced for small values of the wavenumber $ka$ (Figure 2.15).
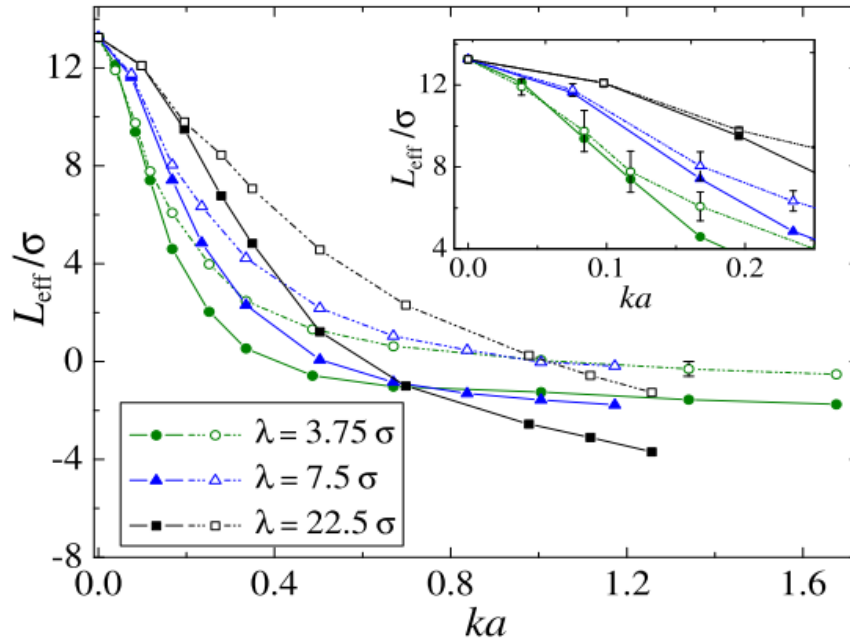


**Figure 2.15:** Effective slip length as a function of the wavenumber ka for various values of the wavelength λ. The dotted lines correspond to the continuum results and the continuum ones to the MD results [85]

Cao et al. [87] conducted a very concise Molecular Dynamics study on the effects of roughness on the gas flows on microchannels by means of NEMD Simulations. For the purpose of their analysis they modelled the rough wall topography using a) triangular, b) rectangular, c) sinusoidal and d) random triangular waves using argon as the gas. All of the rough profiles used shared a common amplitude $A$ and a common period $P$. The yielded results revealed that the roughness geometry plays an important role in the flow and friction characteristics. More specifically, for the four roughness types examined it was shown that the roughness effect increases with the following order of rough wall profiles:

1. Rectangular waves
2. Sinusoidal waves
3. Triangular waves
4. Random triangular waves

Finally, the authors proposed that there are two mechanisms through which the rough wall profiles may affect gas microflows: a) the streamlines in the vicinity of rough walls are

**2.3** MD simulations of liquids confined in nanochannels with rough walls

distorted and b) the penetration of argon atoms in the wall cavities is enhanced as well as the momentum exchange due to the increased collision of the trapped atoms.

Asproulis and Drikakis [43] investigated the effect of the roughness amplitude on the slip length in nanoflows. Their model was comprised of Argon particles confined by two solid walls. They modelled rough walls using rectangular protrusions with variable height and estimated the slip length $L_s$ as a function of the roughness amplitude for three values of the wall fluid interaction parameter $\varepsilon_{wf}$: a) $\varepsilon_{wf} = 0.2\,\varepsilon$, b) $\varepsilon_{wf} = 0.4\,\varepsilon$ and c) $\varepsilon_{wf} = 0.6\,\varepsilon$ as shown in Figure 2.16. Similarly to previous studies, it is shown that the slip length is higher for more hydrophobic surfaces (smaller values of $\varepsilon_{wf}$) and that it decreases exponentially with the roughness amplitude and the no-slip boundary condition becomes valid for $A > 2\,\sigma$.
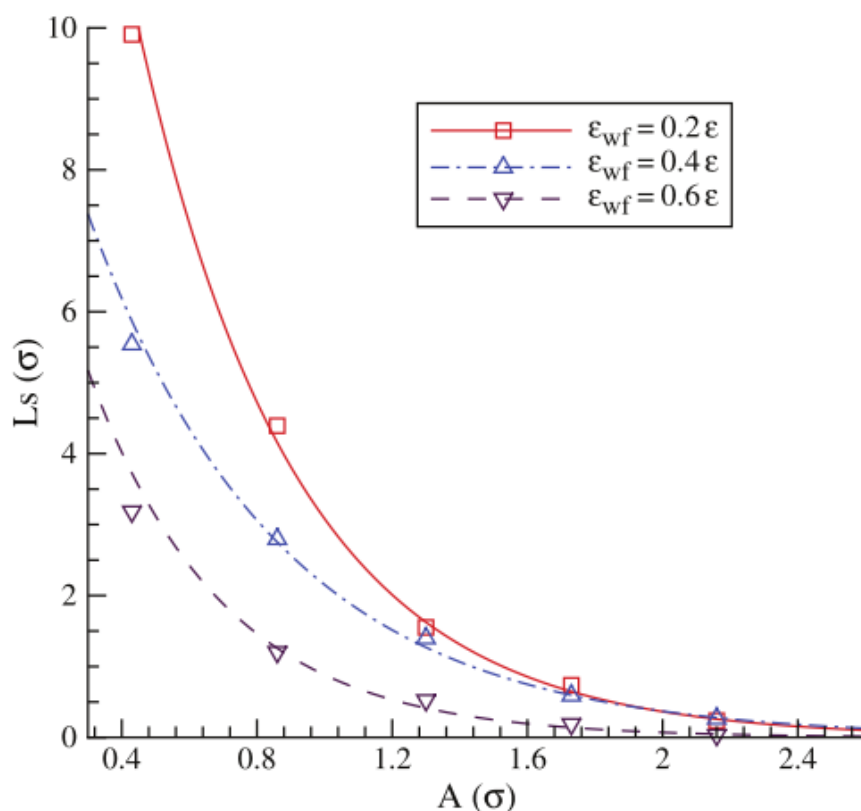


**Figure 2.16:** Slip length L$_s$ vs. corrugation amplitude A for various wall-fluid interaction parameters ε$_{wf}$ [43]

Chen et al. [81] investigated the dependence of the slip length on the fractal dimension $D$ which is indicative of a fractal to fill up space and adjust the complexity of the nanochannel walls: the larger the fractal dimension the more irregular the roughness geometry profile. In their study fluid atoms were confined by a fractally rough (lower) and a smooth (upper) wall on which a constant force was applied in order to create a Couette flow. They estimated the slip length as a function of the fractal dimension for various values of the average roughness height $\delta$. As far as the roughness height is considered, their results were in agreement with [43]: the slip length decreases with increasing average roughness height. Moreover, the slip length was found to be decreasing almost linearly with the fractal dimension due to the more frequent wall irregularities (Figure 2.17).
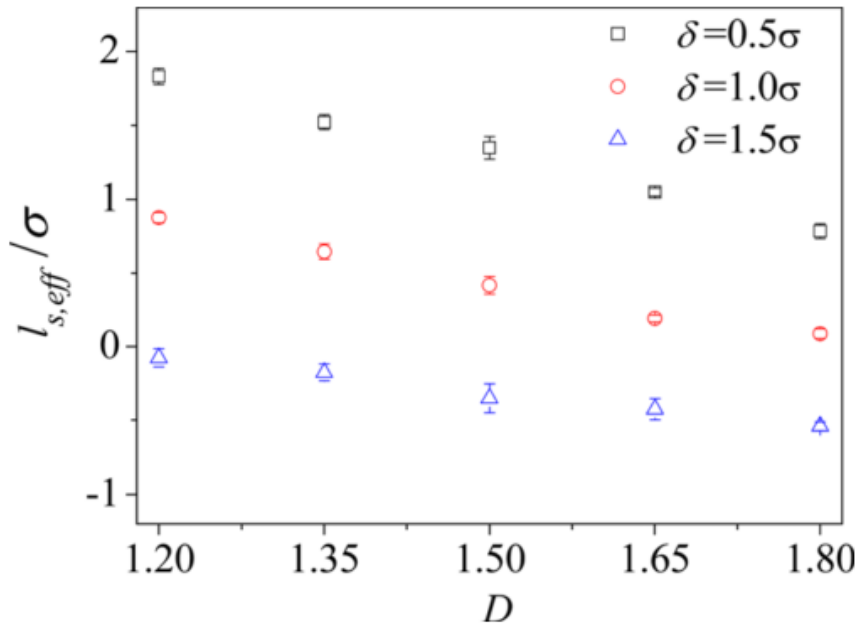
**Figure 2.17:** Slip length as a function of the fractal dimension for various values of the average roughness height [81]
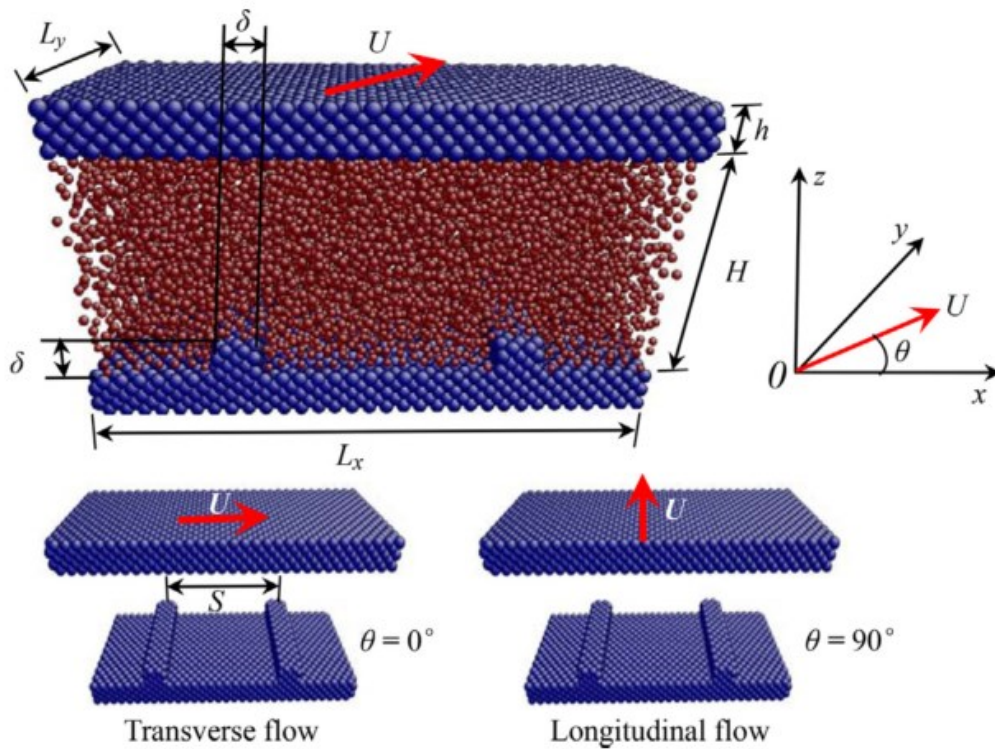


**Figure 2.18:** Schematic representation of the Molecular Dynamics model of Zhang and Chen [88]

A summarising 3-dimensional Molecular Dynamics study considering the effects of a) the roughness amplitude, b) the liquid-solid interaction strength and c) the orientation of the

shear flow was conducted by Zhang and Chen [88]. They investigated the Couette flow in a rough nanochannel with rectangular protrusions in the lower wall and a moving smooth upper wall (Figure 2.18). They confirmed the results of previous investigations as far as the liquid solid interaction and the roughness amplitude are considered [43] and additionally they showed that the roughness effect on the slip length depends on the shear flow orientation. In particular, the change from transverse to longitudinal flow contributes to the increase of the slip length as the obstruction of the flow due to the rectangular protrusions becomes weaker.

## 2.3.4 Viscosity

As it has been discussed in the two previous sections, rough nanochannels walls affect the rheological properties of confined liquids. The density and velocity profiles drawn by means of Molecular Dynamics simulations revealed that roughness induces significant variations in the liquid structure of confined liquids and enhances the momentum transfer in the boundary fluid layers. These observations in combination with some earlier experimental results [89], pointing out that the rheological properties of confined fluids are dependent on the wall topography, triggered computational researchers to focus on the effects of wall surface roughness on the fluid viscosity. Non-Equilibrium Molecular Dynamics simulations were mainly perdormerd for this purpose as the Green Kubo relations have been proven to ineffective for systems being far from equilibrium [90].

One of the first MD investigations for determining the surface roughness effects on the shear viscosity was conducted by Jabbarzadeh et al. [79]. The nanochannel under investigation consisted of two sinusoidal walls with amplitude $A$ and period $P$ and the effects of the aforementioned parameters on the fluid shear viscosity were examined. The yielded results showed that the shear viscosity increases monotonically for higher values of the roughness amplitude. The authors proposed that this was a consequence of the enhancement of density in the nanochannel centre induced by the increased roughness amplitude. However, they did not manage to distinguish a clear effect of the roughness period on the fluid viscosity.

The effect of the roughness amplitude on the shear viscosity was also examined by Yung et al. [91] who studied the Couette flow of a liquid crystalline polymer (LCP) melt confined by two sinusoidal walls. Similarly to [79] they found that the shear viscosity increases nonlinearly with increasing roughness amplitude $A$. They attributed this behaviour to the change in the LCP structure from the crystalline phase to the isotropic one and supported this allegation with a plot of the Orientational Order Parameter vs. the roughness amplitude (Figure 2.19 & Figure 2.20). They suggested that as the roughness amplitude increases the nanochannel becomes narrower and the binding effect of the walls on the LCP molecules becomes stronger giving rise to phase change.

A more recent NEMD study by Sofos et al. [90] focused on the effect of the roughness period on the shear viscosity in rough nanochannels with rectangular protrusions. Their model consisted of liquid argon confined by a smooth and a rough wall. They developed a Poiseuille flow by applying an external driving force on the fluid molecules and estimated the shear viscosity using Eq. 2.6. Their results showed that in all cases the shear viscosity in rough

nanochannels is higher than in smooth ones but the shear viscosity was not found to increase monotonically with the roughness period, a result which is consistent with previous investigations [79].
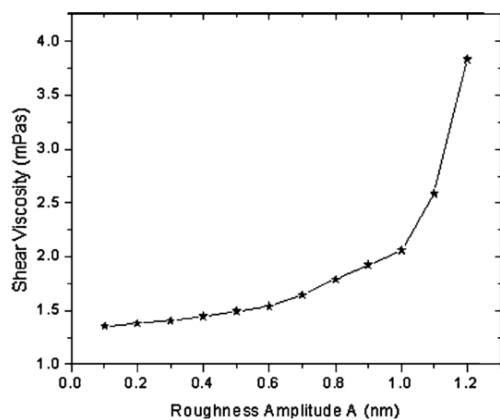


| **Figure 2.19:** Shear viscosity vs. the Roughness Amplitude [91] | **Figure 2.20:** Orientational Order Parameter vs. the Roughness Amplitude [91] |
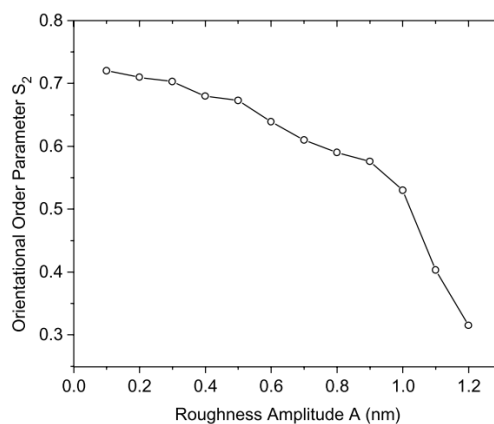
## 2.3.5 Interfacial Thermal Resistance

Despite the fact that the effect of many parameters on the thermal resistance such as the interaction strength ([65]), the wall bonding stiffness [67], the nanochannel wall temperature [69] and the heat flux [70] has been investigated by means of Molecular Dynamics Simulations, we cannot say the same for the effect of the Roughness Amplitude on the ITR which has only been investigated by a few researchers.

One of the first Molecular Dynamics studies focusing on the effects of surface roughness on the thermal resistance in nanochannels was performed by Shibahara and Takeuchi [92]. Their system was water confined by a smooth and a rough wall and the interactions between the water molecules were described using the SPC/E potential. Roughness was modelled using rectangular nanostructures with a constant height $h = 0.7\,nm$ and a varying clearance: $0 < L < 2.81\,nm$. It was found that the thermal resistance reached its minimum value for $L = 0.7\,nm$ and that ITR is not exclusively a function of the exposed solid surface area but also depends on the roughness geometry which affects the penetrability of the fluid atoms in the wall cavities.

Acharya et al. [93] studied how the thermal conductance is influenced by the surface roughness in a 3-dimensional system consisted of a central bilayer made of two self-assembled monolayers (SAMs) surrounded by water molecules as illustrated in Figure 2.21. The SAMs were held in position by attaching their edges (sulphur atoms) to the positions of a FCC lattice. Roughness was modelled by alternating the chain length of the SAMs and 5 different surface types were created: a) flat, b) grooved surface with width $w$ equal to 1 headgroup diameter and depth equal to 2 carbon diameters, c) grooved surface with width $w$ equal to 2 headgroup diameter and depth equal to 2 carbon diameters, d) grooved surface with width $w$ equal to 2 headgroup diameter and depth equal to 4 carbon diameters and e) sinusoidal surface (Figure 2.22). Their results showed that the interfacial thermal conductance increases under the

presence of roughness with the sinusoidal walls inducing higher thermal conductance compared to the walls with rectangular protrusions, a result which is consistent to [87].
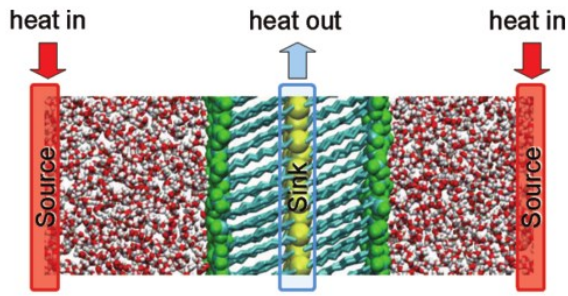


**Figure 2.21:** Molecular Dynamics system setup of [93] with water (red &white), alkane tails (cyan), headgroups (green) and sulphur (yellow)
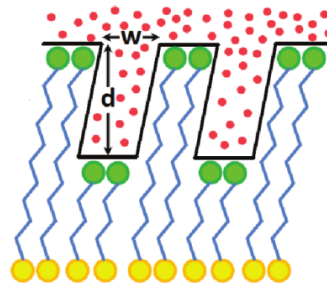


**Figure 2.22:** Schematic representation of the rough surface pattern [93]

Chen and Zhang [94] performed Molecular Dynamics simulations and investigated the effects of surface roughness on the thermal conductance in nanochannels. They simulated the movement of monatomic particles in a nanochannel with a smooth (upper) and a rough (lower) wall. Three rough surface profiles with the same statistical roughness $\delta$ were generated using the Cantor fractal by alternating the value of the fractal dimension $D$. In order to impose a temperature gradient, heat was added to the upper wall at a constant rate, while the lower wall was maintained at a steady temperature. The thermal conductance was estimated as a function of the fractal dimension and it was observed that it increases almost linearly with the fractal dimension. This is because larger fractal dimension contributes towards the increase of the liquid-solid interface area (even if the statistical roughness is constant) and the longer trapping time of the liquid atoms inside the wall asperities.

# 2.4 Conclusions
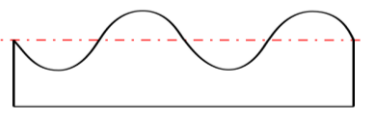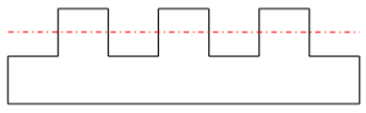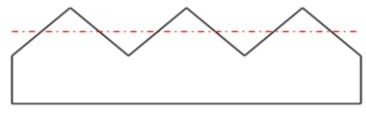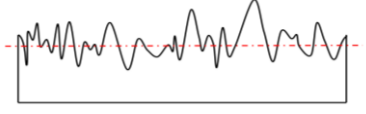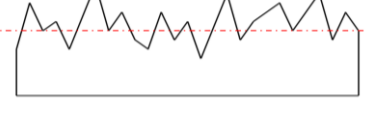
This chapter provides a brief overview of the state of the art in the Molecular Dynamics simulations of micro- and nanoflows. It is clear that in such small scales deviations from the continuum models appear as the volume over surface ratio decreases and consequently surface effects become dominant over volume effects. This fact gives rise to a number of phenomena that cannot be observed in macroscale and therefore cannot be explained via the continuum description. For example, in contrast to continuum flows, in micro- and nanoflows the slip flow should not be negligible.

The Molecular Dynamics simulation technique allowed scientists to shed light in the phenomena taking place in nanochannel flows. Molecular Dynamics simulations have enhanced our understanding of the effects of various parameters on the flow characteristics and the fluid properties, such as the slip length, viscosity and the interfacial thermal resistance. Later on, Molecular Dynamics studies focused on the wall surface roughness effects in nanoflows. There are clear indications that increased roughness contributes towards the reduction of the slip length, leads to higher values of the viscosity of confined fluids and enhances thermal conductance.

**2.4** Conclusions

Until now, various roughness models have been used for the generation of rough nanochannel walls as shown in Table 2.1. The first attempts to generate rough surfaces implemented periodic (rectangular, triangular and sinusoidal) patterns. For more realistic representation of the rough walls, scientists also used random patterns, such as fractals or random triangular waves. However, until today there have not been any 3-dimensional Molecular Dynamics models for the investigation of nanoflows and the properties of the confined liquids. Such a model would greatly improve our understanding of the mechanisms leading to the reduction of the slip length, the enhancement of the thermal conductance and the alternation of the viscosity when roughness is present.

| Roughness model | Pattern | Schematic representation | References |
|---|---|---|---|
| Periodic | Sinusoidal |  | [87] |
| | Rectangular |  | [43], [83], [87] |
| | Triangular |  | [87] |
| Random | Fractal geometry (2D) |  | [81], [95] |
| | Random triangular wave |  | [87] |

**Table 2.1:** Overview of roughness models implemented in Molecular Dynamics Simulations

Therefore, there are still some unanswered questions regarding the underlying physics that induce the aforementioned phenomena such as:

- How does the structure of the fluid change in 3-dimensions when roughness is introduced in the solid channel walls?
- Can Molecular Dynamics simulations predict the increase of the shear viscosity in the vicinity of the nanochannel walls, as pointed out by experimental investigations [89], when roughness is existent?
- How does 3-dimensional roughness affect the thermal conductance in nanoscale according to the Molecular Dynamics results?

In this PhD research the Molecular Dynamics method has been selected for the investigation of the aforementioned topics. The reason for this selection is that only a molecular resolution method will allow us to observe the behaviour and the structure of the fluid at very

**2.4** Conclusions

small scales. The main focus is turned on the effects of wall roughness on the flow behaviour and the fluid properties such as the slip length, the viscosity and the thermal conductance of confined liquids.

# 3  Methodology & Validation

## 3.1 Introduction

In this chapter, we will focus on the Methodology implemented for performing our Molecular Dynamics simulations of nanoflows and the validation of our model. The first paragraph is devoted to the basic theoretical background concerning the Molecular Dynamics method. In this paragraph the Molecular Dynamics algorithm will be explained and we will present the necessary steps for the setup and run of a MD simulation. Additionally, we will describe the basic principles of statistical mechanics which is the main tool for interpreting the results of MD simulations. We will also provide a general description of the multivariate Weierstrass-Mandelbrot function which will be later used for the generation of 3-dimensional fractal wall surfaces.

In the *Methodology* paragraph we will illustrate the methodology we followed for setting up our simulations for each chapter of the results. In general, we will describe the procedure followed for generating the rough wall topography, the interactions we used for modelling the interactions between the wall and the fluid atoms, the thermostating methods, and the mathematical relationships for calculating the various and some complementary simulation details.

Finally, in the *Validation and Verification* paragraph we will provide the reader with an overview of our model and check its validity. Finally, we will compare selected results of our simulations with results presented in the past in order to gain the reader's trust.

## 3.2 Basic Theory

### 3.2.1 Simulation setup

In this section we will describe the fundamental steps required for the initialisation of a Molecular Dynamics Simulation:

1.  Positioning of the wall atoms on the sites of a lattice.
2.  Energy minimisation for avoiding extra equilibration time.
3.  Definition of the boundary conditions.
4.  Definition of the appropriate forcefield.

#### 3.2.1.1 Lattice positioning

During the initialisation of a molecular simulation the initial position of the atoms has to be determined. This necessity lies in the fact that a random positioning of atoms would cause some equilibration issues due to the possible overlapping of atoms. Hence, a preferable solution instead of random positioning would be to place the atoms at the edges of a lattice (Figure 3.1). Depending on the number of dimensions characterising the problem a suitable lattice can be

used. The most common 2-dimensional lattices are the square and the hexagonal lattices while the most common lattice types used in 3 dimensions are the face centred cubic and the body centred cubic. All the 3-dimensional crystal systems can be categorised into 7 groups as presented in Table 3.1. Those 7 groups can be used as a basis for the generation of 14 lattice types, called Bravais Lattices which are illustrated in Appendix A.1.
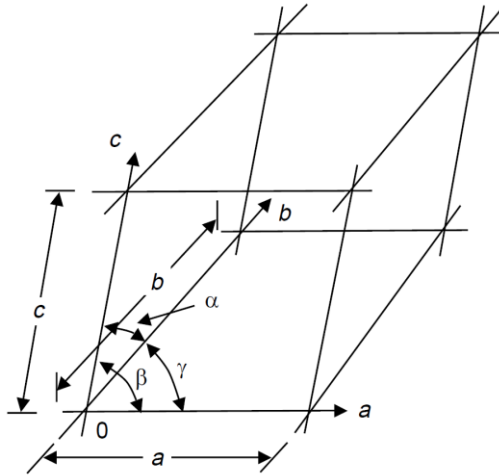


| Crystal system | Edge length | Interaxial angle |
|---|---|---|
| Triclinic | $a \neq b \neq c$ | $\alpha \neq \beta \neq \gamma \neq 90°$ |
| Monoclic | $a \neq b \neq c$ | $\alpha = \gamma = 90° \neq \beta$ |
| Orthorhombic | $a \neq b \neq c$ | $\alpha = \beta = \gamma = 90°$ |
| Tetragonal | $a = b \neq c$ | $\alpha = \beta = \gamma = 90°$ |
| Hexagonal | $a = b \neq c$ | $\alpha = \beta = 90°, \gamma = 120°$ |
| Rhombohedral | $a = b = c$ | $\alpha = \beta = \gamma \neq 90°$ |
| Cubic | $a = b = c$ | $\alpha = \beta = \gamma = 90°$ |

**Figure 3.1:** Unit cell          **Table 3.1:** Crystal systems

Besides avoiding the overlapping of atoms, lattices are used when modelling metals which are characterised by highly symmetrical structures and close-packed atoms. For example, in the case of nanochannel flows the wall atoms are usually placed on a lattice [6] in order to mimic a metallic surface. Most of the structural metals crystallise in 3 arrangements: a) face centred cubic lattice (FCC) b) hexagonal close packed lattice (HCP) and c) body centred cubic (BCC) (Table 3.2).

| Element | Crystal structure | Closest interatomic distance (nm) |
|---|---|---|
| Aluminium | fcc | 0.286 |
| Copper | fcc | 0.255 |
| Gold | fcc | 0.288 |
| Iron | bcc | 0.248 |
| Lead | fcc | 0.350 |
| Nickel | fcc | 0.249 |
| Silver | fcc | 0.289 |
| Titanium | hcp | 0.299 |
| Zinc | hcp | 0.266 |

**Table 3.2:** Crystal structure of some metals at room temperature

In order to denote directions and planes in a lattice the Miller indices are used. The procedure to determine the Miller indices is described in Appendix A.2.

In metals, plastic deformation occurs as close-packed crystal planes called "slip planes" slide past each other. This happens because the distance between the slip planes is larger than for any other parallel planes. This phenomenon facilitates the sliding between them due to weaker interaction. It has been observed that slip planes are characterised by high atomic

density. Similarly, it has been observed that in microflows the maximum slip length is obtained when the (111) plane of a FCC crystal structure is placed parallel to the direction of the flow [33].

### 3.2.1.2 Energy minimisation

Energy minimisation is a process widely used in molecular modelling and comprises of a group of techniques aiming to find an energetically favourable conformation of a group of atoms. This kind of geometry optimisation performs a walk on the potential energy surface in order to locate the closest valley to the starting point (Figure 3.2). Energy minimisation is mainly used to prepare a system for further simulations (MD or MC) in order to reduce the equilibration time and simultaneously avoid any initial conformations such as overlapping that could cause unwanted interactions between the atoms. This method is mainly implemented when modelling macromolecules where both bonded and non-bonded interactions contribute to the final expression of the potential energy as defined by the selected forcefield. There are 3 main minimisation methods which are briefly described in Appendix A.3: a) Steepest descent b) Conjugate gradient and c) Newton-Raphson.
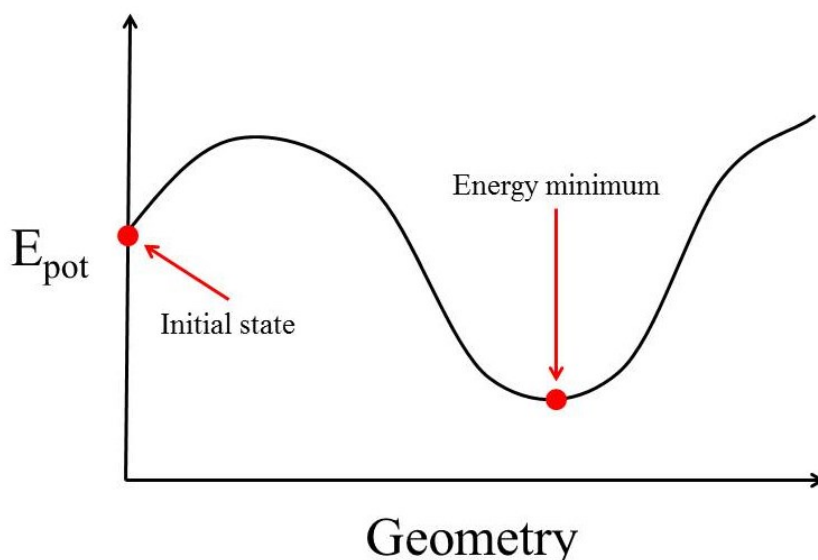


**Figure 3.2:** Energy minimisation in 2 dimensions

### 3.2.1.3 Boundary Conditions

### Periodic boundary conditions

The specification of the dimensions of the system under examination is one of the most important decisions that have to be taken during the initialisation of a molecular model. A large system would allow us to calculate its properties with relatively high accuracy compared to a small one but on the other hand this would require a high computational cost because of the increased number of atoms contained in it. In the imaginary case of a closed system containing a large number of atoms it would be possible to capture the typical behaviour of the confined atoms since the surrounding walls would not greatly affect their movement. However, in the case of a molecular dynamics simulation where only a small number of atoms can be included

in the simulation box, the interaction of the atoms with the surrounding walls would not allow us to calculate the bulk properties of the system.
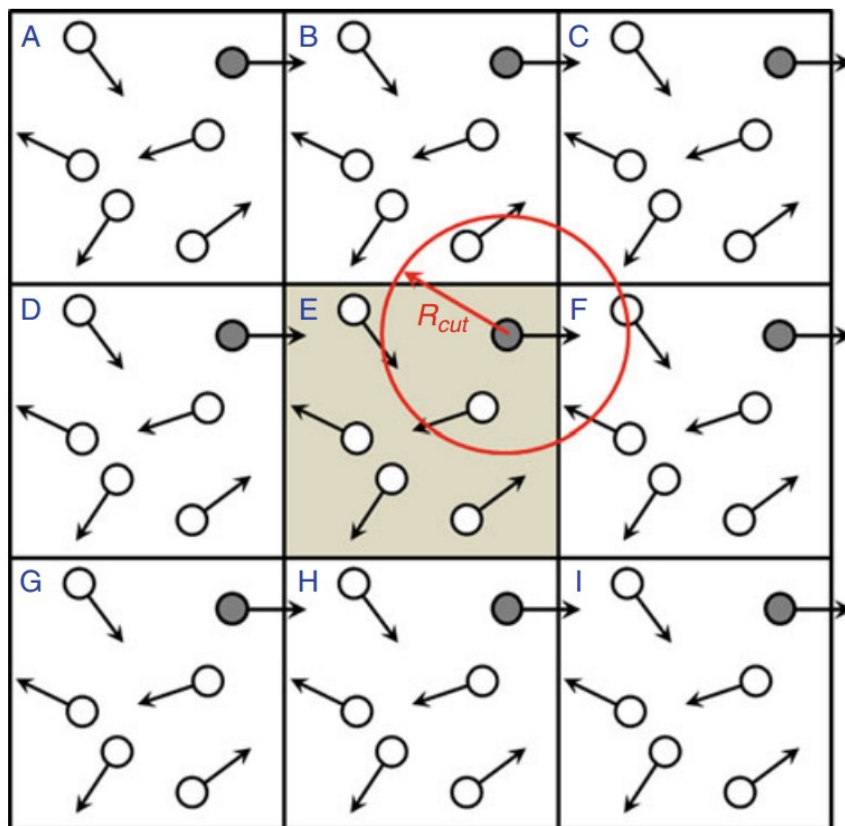


**Figure 3.3:** Periodic boundary conditions

This problem can be solved by using periodic boundary conditions which partially allow the simulation of a seemingly infinite system. Periodic boundary conditions (Figure 3.3) introduce identical copies of the simulation box along its surrounding. There are 2 basic conditions that have to be fulfilled in order to apply periodic boundary conditions to our system. The former states that if an atom leaves the simulation box passing through one of the boundaries then it immediately re-enters the simulation box through the opposite boundary. The latter one states that an atom lying close to one boundary of the simulation box interacts within a cutoff distance $r_c$ with the atoms lying in the opposite face, i.e., there is a wraparound effect.

During the course of a molecular dynamics simulation it is of great importance that the position of the atoms after each timestep is recorded and updated because if one atom has moved outside the simulation box, its position will have to be modified in order to bring it back inside. A schematic representation a simulation cell as well as the position vector of an atom $i$, $\boldsymbol{r}_i = r_{ix}\boldsymbol{\hat{\imath}} + r_{iy}\boldsymbol{\hat{\jmath}}$ are depicted in Figure 3.4. After each timestep the following tests have to be performed [96]:

- If $r_{ix} \geq L_x/2$, then $r'_{ix} = r_{ix} - L_x$
- If $r_{ix} < -L_x/2$, then $r'_{ix} = r_{ix} + L_x$

Similarly, if $r_{ijx}$ is the distance between two atoms $i$ and $j$:

- If $r_{ijx} \geq L_x/2$, then $r'_{ijx} = r_{ijx} - L_x$
- If $r_{ijx} < -L_x/2$, then $r'_{ijx} = r_{ijx} + L_x$
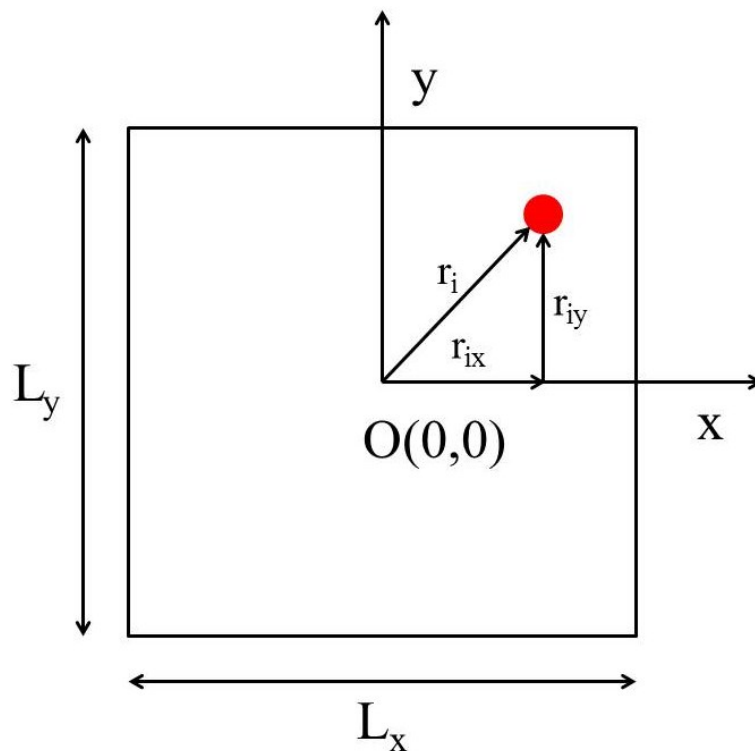


**Figure 3.4:** 2-dimensional simulation box

Despite the application of boundary conditions the finite size effects cannot be limited effectively when the number of atoms is not large enough. A reduced number of atoms can lead to large fluctuations in statistical averaging and non-accurate calculation of properties. For example, in the case of polymeric materials one can find that for many problems of interest, the system should at least contain $10^6$ atoms or even much more in order to obtain results corresponding to the real behaviour of the material. This is because polymer chains are usually consisted of thousands of atoms arranged in various conformations in space. Therefore, it can be concluded that the number of atoms in the simulation cell strongly depends on the characteristic length of the problem [97].

## Fixed boundary conditions

When simulating closed or confined systems fixed boundary conditions shall be used in at least one direction. Fixed boundary conditions can be applied via two ways:

- Continuous barrier potential: a virtual flat repulsive boundary is introduced through complex expressions such as the (10-4-3) Steele potential [98]:

$$V(z) = 4\pi\varepsilon_{wf}\rho_s\sigma_{wf}^2\left[\frac{1}{5}\left(\frac{\sigma_{wf}}{z}\right)^{10} - \frac{1}{2}\left(\frac{\sigma_{wf}}{z}\right)^4 - \frac{\sigma_{wf}^4}{6\Delta(z + 0.61\Delta^3)}\right] \quad \text{Eq. 3.1}$$

where $\rho_s$ is the density of the solid, $\varepsilon_{wf}$ and $\sigma_{wf}$ the wall fluid Lennard Jones parameters, $z$ is the shortest distance between the fluid particle and the solid wall and $\Delta$ is the interlayer spacing of the solid.

- Rigid atomistic walls: the coordinates of the wall atoms are fixed or attached to springs with high stiffness $k$ in order to maintain the wall structure rigid and simultaneously flexible enough when interacting with the confined atoms. In the case of wall atoms attached to springs the temperature of the wall and consequently the confined fluid can be controlled by applying a thermostat at the wall region in contrast to immobile wall atoms.

### 3.2.1.4 Force fields and interatomic potentials

Force fields in molecular modelling are being used to describe the time evolution of the interatomic interactions and estimate the potential energy of a system. They are sets of equations designed in order to reproduce molecular bonds (Appendix A.4) and experimental properties of molecules based on experimental observations and quantum mechanical principles. Force fields consist of empirical expressions of the interatomic interactions which are particularly important as they reduce the computational cost comparing to quantum mechanical treatment. The total potential energy of a system is given by a summation of the contributions from VdW, electrostatic, covalent, etc. interactions:

$$V_{tot} = V_{coul} + V_{vdW} + V_{covalent} + \cdots \qquad \text{Eq. 3.2}$$

In molecular modelling the calculation of each term in Eq. 3.2 is achieved with the help of force fields or interatomic potentials.

### Pair potentials

Pair potentials are being widely used to describe noble gases such as argon [49]. The simplest pair potential assumes that the total potential energy of the system depends only on the distance between two atoms $r_{ij}$:

$$V_{tot} = \frac{1}{2} \sum_{i \neq j=1}^{N} \sum_{j=1}^{N} V(r_{ij}) \qquad \text{Eq. 3.3}$$

In order to calculate the term $V(r_{ij})$ we have to account for the repulsion in short interatomic distances and the attraction in long ones. Therefore most of the interatomic potentials use two terms in order to describe this behaviour:

$$V(r_{ij}) = V_{repulsive} + V_{attractive} \qquad \text{Eq. 3.4}$$

The potential energy of a single atom on the system is given by:

$$V_i = \sum_{j=1}^{N_i} V(r_{ij}) \qquad \text{Eq. 3.5}$$

where $N_i$ is the number of the neighbours of the atom $i$.

The most well-known and widely used pair potential is the 12-6 Lennard-Jones potential:

$$V(r_{ij}) = 4\varepsilon \left[ \left( \frac{\sigma}{r_{ij}} \right)^{12} - \left( \frac{\sigma}{r_{ij}} \right)^{6} \right] \qquad \text{Eq. 3.6}$$

where $\varepsilon$ is the well depth being indicative of the bond strength and $\sigma$ is the interatomic distance for which the potential energy becomes equal to zero (Figure 3.5). The distance at which the potential energy obtains its minimum value (equilibrium bond length) is $r_m = 2^{1/6}\sigma$. In Eq. 3.6 the first term in the square brackets represents the interatomic repulsion and the second term the attraction. Another popular pair potential is the harmonic potential:

$$V(r_{ij}) = a_0 + k(r_{ij} - r_0)^2 \qquad \text{Eq. 3.7}$$

where $a_0$ is the equilibrium bond length and $k$ the spring constant.

There is no doubt that pair potentials are computationally effective and easy to be implemented. Moreover, during the past years the input parameters such as $\varepsilon$ and $\sigma$ have been precisely determined for many types of atoms [99]. However, they fail to describe effectively the behaviour of complex molecules or metals.
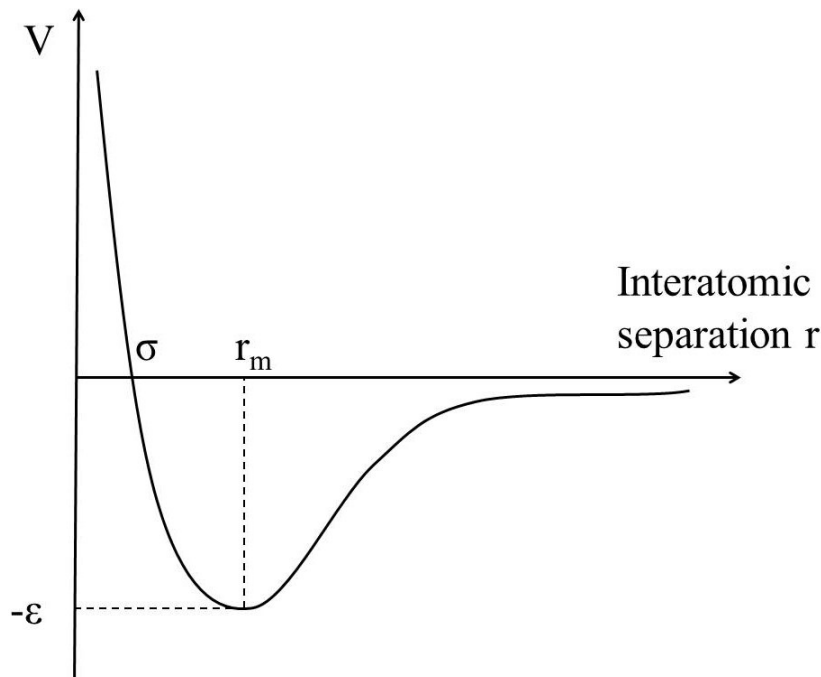


**Figure 3.5:** The 12-6 Lennard Jones potential

## Embedded Atom Model

As it has been mentioned in the previous section, pair potentials are incapable of reproducing reliable results for materials such as metals or hydrocarbons [100]. Their main defect lies in the fact that they cannot capture the difference between the forces exerted on

atoms close to the surface of a rigid body and atoms that belong to the bulk. This is because they do not consider the neighbours of an atom to determine the bond strength. To overcome this issue "many-body potentials" in which the interatomic force depends on a great number of neighbours have been developed. In the case of metals, accurate results can be produced using the EAM potential:

$$V_i = \sum_{j=1}^{N_i} V(r_{ij}) + f(\rho_i)$$    Eq. 3.8

where $\rho_i$ is the local electron density and $f$ the embedding function. Many-body potentials are capable of capturing the elastic behaviour of metals [101] and distinguishing the different interactions between atoms at the surface and in the bulk of a rigid body (Figure 3.6). However, when covalent bonding is dominant such as in the case of silicon or when there are any directional effects because of the material anisotropy, EAM is not an accurate method. Therefore, modified many-body potentials (MEAM) have been proposed which include the effects of directions on the electron density [102].
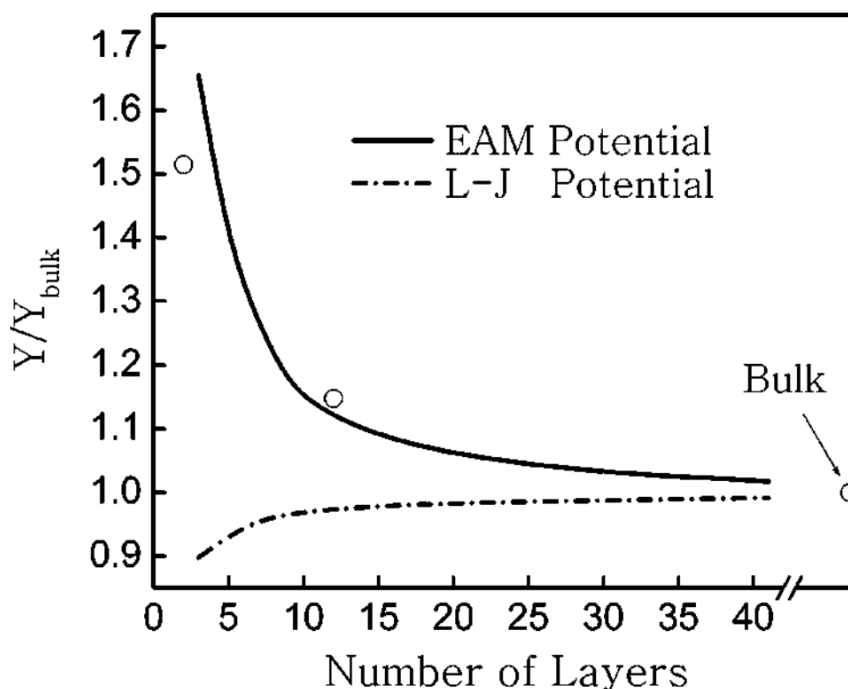


**Figure 3.6:** Young's modulus as a function of thickness of a nanoplate based on EAM and Lennard-Jones potentials [101]

Besides the pair potentials and the force fields presented in this paragraph researchers have also developed forcefields for polymers and forcefields aiming to describe chemical reactions. Details can be found in Appendix A.5 and Appendix A.6.

## 3.2.2 Statistical Mechanics

### 3.2.2.1 Introduction

Molecular modelling allows scientists to observe the trajectories of atoms in atomic scale. Molecular modelling methods such as Molecular Dynamics and Monte Carlo reproduce the dynamics of a system such as the positions, velocities or trajectories of atoms. However, this information is not enough to extract macroscopic properties such as the viscosity, the internal energy or the pressure of the system under examination. Statistical mechanics have been developed in order to convert the output of molecular models to macroscopically observable quantities.

Let us consider a particular point $\boldsymbol{\Gamma}(\boldsymbol{p}, \boldsymbol{q})$ in the phase space which is described by the sum of the possible values of position and momenta of the particles. In order to observe a macroscopic property $A(\boldsymbol{\Gamma})$ of a system, we have to calculate the average of $A(\boldsymbol{\Gamma})$ over a long observation time $t_{obs}$:

$$A_{obs} = \langle A \rangle_{time} = \langle A(\boldsymbol{\Gamma}(t)) \rangle_{time} = \lim_{t_{obs} \to \infty} \frac{1}{t_{obs}} \int_0^{t_{obs}} A(\boldsymbol{\Gamma}(t)) dt \qquad \text{Eq. 3.9}$$

However, calculating the complex time averages of a system over long time intervals is a very complex procedure that would require enormous computational time. However, it has been observed that a system being in equilibrium will flow through all the possible microstates defined by the imposed constraints over a time interval. The sum of all the possible microstates of a system as defined by the thermodynamic constraints imposed is called an ensemble. In order to avoid time averaging, Gibbs [103] suggested replacing the time average of a property $A$ with the ensemble average:

$$A_{obs} = \langle A \rangle_{time} = \frac{1}{N} \sum_{n=1}^{N} A_n \qquad \text{Eq. 3.10}$$

where $N$ is the total number of measurements and $A_n$ is the value of the property $A$ during the $n^{th}$ measurement. It has to be noted that the duration of measurements is infinitesimal so the $n^{th}$ measurement corresponds to a single microstate of the system. Thus, Eq. 3.10 can be transformed to:

$$A_{obs} = \sum_{n=1}^{N} \frac{1}{N} \left( \begin{array}{c} Number\ of\ times\ that\ state\ n\ is \\ observed\ in\ the\ total\ N\ observations \end{array} \right) A_n \qquad \text{Eq. 3.11}$$

where $A_n = \langle A \rangle_n = \langle n|A|n \rangle$ is the expectation value of the property $A$ when the system is in the microstate $n$. It is clear that the fraction:

$$\frac{Number\ of\ times\ that\ state\ n\ is}{\underline{observed\ in\ the\ total\ N\ observations}}$$
$$Total\ number\ of\ observations$$

is the probability $P_n$ of the system to spend time in the microstate $n$. Therefore Eq. 3.11 can be rewritten as:

$$A_{obs} = \sum_n \frac{1}{N} P_n A_n = \langle A \rangle_{ensemble} = \langle A \rangle_{time} \qquad \text{Eq. 3.12}$$

Systems that adhere to this principle are referred to as ergodic.

Finally, with the help of statistical mechanics, thermodynamic properties, such as temperature and pressure, can be connected to the kinetic and dynamic behaviour of the system particles as presented in Appendix A.7.

### 3.2.2.2 Common Statistical ensembles

The most common ensembles used in statistical mechanics are:

- the Microcanonical ensemble (NVE): constant number of atoms (N), volume (V) and Energy (E)
- the Canonical ensemble (NVT): constant number of atoms (N), volume (V) and Temperature (T)
- the Grand Canonical ensemble ($\mu$VT): constant chemical potential ($\mu$), volume (V) and Temperature (T)
- the Isothermal-isobaric ensemble (NPT): constant number of atoms (N), Pressure (P) and Temperature (T)
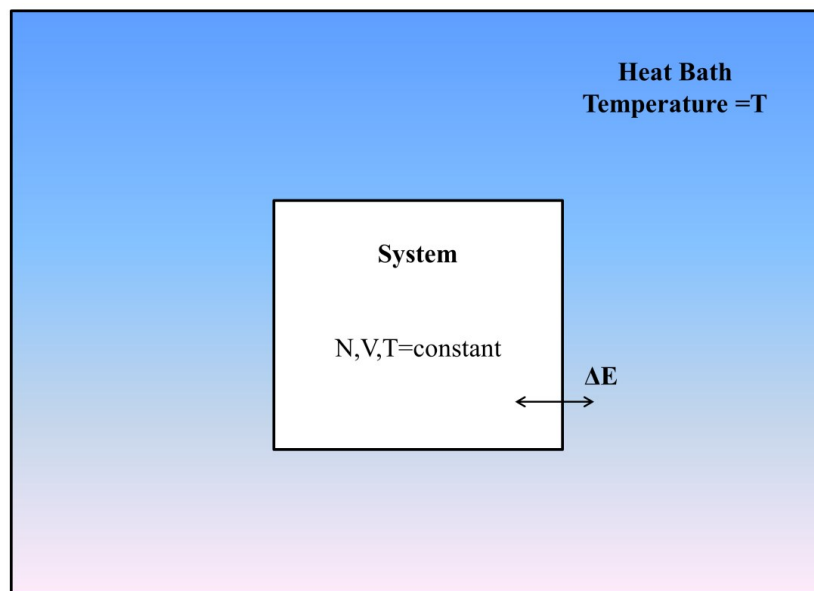


**Figure 3.7:** NVT ensemble

The selection of the appropriate ensemble depends strongly on the nature of the problem under examination. However, the above mentioned ensembles can be divided in two categories. In the Microcanonical, Canonical and Isothermal-Isobaric ensembles the number of atoms is maintained constant and consequently should be used only for closed systems. On the contrary, the Grand Canonical should be employed for open systems. In order to describe statistical

ensembles we have to derive their corresponding partition functions which represent all the thermodynamic and statistical information of a system in equilibrium (Appendix A.8).

# 3.2.3 Molecular Dynamics

## 3.2.3.1 Introduction

Molecular dynamics is a computational technique aiming to reproduce a realistic behaviour of physical systems observed in experiments by studying the movement, the deformation and the interactions between the atoms. In a typical molecular dynamics simulation the movement of particles obeys to the classical mechanics laws such as the Newton's laws of motion and the mass conservation while the interatomic interaction is described by interatomic potentials and forcefields. This method has been pioneered by Alder and Wainwright [25] who were the first to attempt to solve numerically the equations of motion of a system of particles. Nowadays, the MD method has been enriched by new interatomic potentials, force fields and simulation techniques. Moreover, molecular dynamics have found great application in a variety of physical problems because of their attribute to allow the user to determine all the simulation parameters from ab initio. However, because of the finite computer power MD simulations suffer from time and spatial limitations. For example in order to obtain accurate results for a polymeric system where the initial position of atoms (conformations) plays a significant role in the simulation results, the simulation has to be repeated several times in order to eliminate the effect of time and spatial restrictions [104]. On the other hand, MD simulations of liquids or gases can yield accurate results as the effects due to initial positioning of atoms can be offset by extending the simulation time.

Despite the aforementioned limitations, molecular dynamics have been successfully applied to study the behaviour of several materials:

- Fluids: slip flow, laminar flow, unstable flow, transport coefficients, fluid interfaces ([4], [105], [106])
- Metals: crack propagation, deformation mechanisms, mechanical properties [107]–[110]
- Polymers: crosslinking process, mechanical properties, glass transition, rheological properties ([85], [111], [112])

## 3.2.3.2 Methodology

Performing molecular dynamics simulations is very similar to the conduction of real experiments [113]. During the initialisation of a typical MD simulation a sample of the system is prepared by positioning the atoms in such a manner that there is no overlapping or configurations that might force the atoms to escape the simulation box. This is achieved by means of minimisation or lattice positioning while random positioning of atoms is not recommended. Moreover, an ensemble of velocities is assigned to the system particles. The next step is the equilibration process which is realised by solving the Newton's equations of motion for each particle until some properties of the system such as temperature, pressure or energy acquire a constant value. During the equilibration stage the motion of atoms is controlled by the application of one of the common statistical ensembles. More specifically, the velocities of particles are rescaled with a specified frequency to satisfy the constraints of

the ensemble selected by the user. Additionally, the total force exerted on each atom by its neighbours within a cutoff distance is estimated based on the interatomic potential used. Finally, the properties of interest are measured. It is reasonable that the longer the measurement duration the more precise the results due to the elimination of the statistical noise. The structure of a typical molecular dynamics algorithm is illustrated in Figure 3.8.
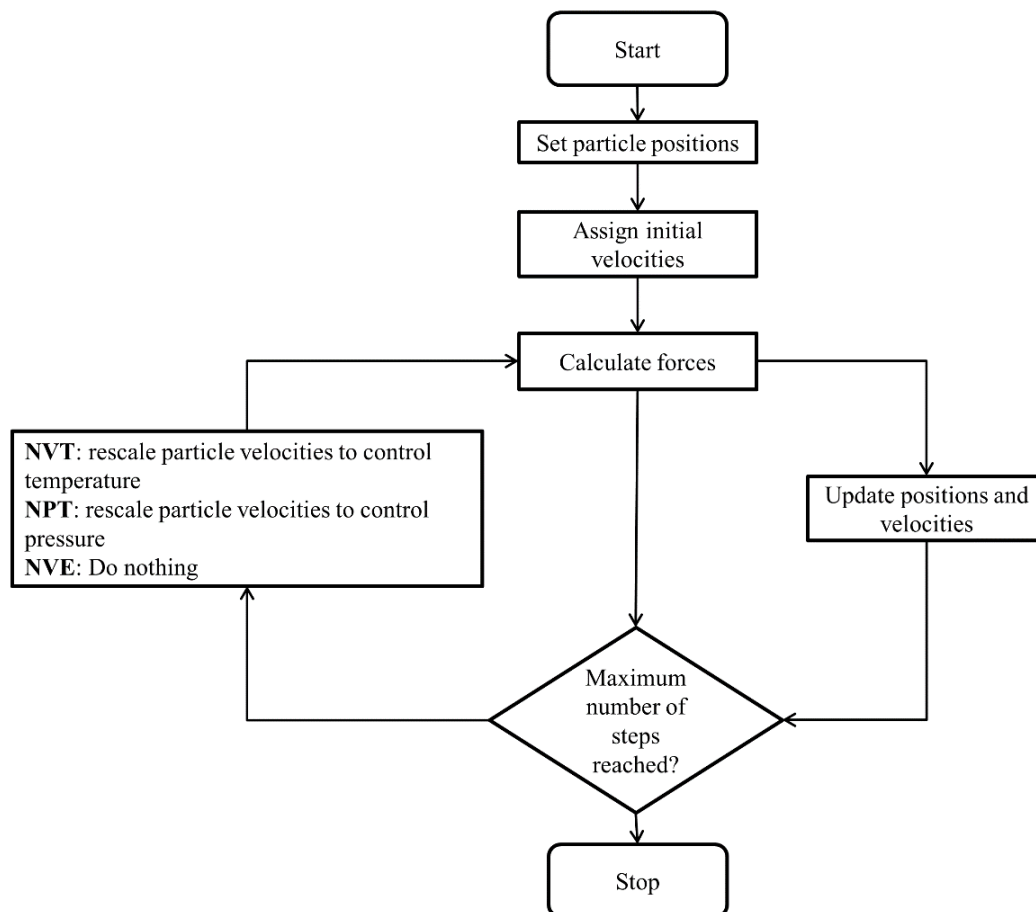


**Figure 3.8:** Flowchart of the Molecular Dynamics methodology [114]

### 3.2.3.3 The Verlet Algorithm

In Molecular Dynamics simulations the integration of the equations of motion is performed using the Verlet integration [115] which is a simple numerical method offering stability and time reversibility. The Taylor expansion of the coordinate of one particle around time $t$ gives:

$$r(t + \Delta t) = r(t) + u(t)\Delta t + \frac{f(t)}{2m}\Delta t^2 + \frac{\Delta t^3}{3!}\dddot{r} + O(\Delta t^4) \qquad \text{Eq. 3.13}$$

where $\Delta t$ is the timestep of the molecular dynamics simulation, $u(t)$ the velocity, $f(t)$ the force and $m$ the mass. Similarly, we obtain:

$$r(t - \Delta t) = r(t) - u(t)\Delta t + \frac{f(t)}{2m}\Delta t^2 - \frac{\Delta t^3}{3!}\dddot{r} + O(\Delta t^4) \qquad \text{Eq. 3.14}$$

Adding the two previous equations gives:

$$r(t + \Delta t) + r(t - \Delta t) = 2r(t) + \frac{f(t)}{m}\Delta t^2 + O(\Delta t^4) \qquad \text{Eq. 3.15}$$

or

$$r(t + \Delta t) \approx 2r(t) - r(t - \Delta t) + \frac{f(t)}{m}\Delta t^2 \qquad \text{Eq. 3.16}$$

The time symmetry used in the Verlet methods reduces the errors by cancelling out the first and third terms of the Taylor expansion and consequently is more accurate than the Taylor expansion. The calculation of the velocity does not require knowledge of the position and can be similarly obtained:

$$r(t + \Delta t) - r(t - \Delta t) = 2u(t)\Delta t + O(\Delta t^3) \Leftrightarrow$$

$$\Leftrightarrow u(t) = \frac{r(t + \Delta t) - r(t - \Delta t)}{\Delta t} + O(\Delta t^2) \qquad \text{Eq. 3.17}$$

It should be noted that the error in the velocity estimation is of the order of $O(\Delta t^2)$.

### 3.2.3.4 Thermostats

In a typical molecular dynamics simulation we can perform averaging only with the Microcanonical ensemble (NVE) which is the only "natural" ensemble. However, sometimes it is needed that simulations using other ensembles are performed. Therefore, there should be a modification of the dynamics of the system in order to satisfy the constraints imposed by each ensemble. This can be achieved through two ways. The first is by mixing Molecular Dynamics with stochastic moves while the second is based on the modification of the Lagrangian equations of motion. The most common thermostats applied are briefly described in Appendix A.9.

## 3.2.4 Fractal Characterisation of Rough Surfaces

It has been observed that natural surfaces possess multiscale properties, i.e. roughness at smaller scales is similar to that of macrosale although the length and height scale is different [82]. This property is called self-affinity. Self-affine surfaces cannot be described by Euclidean geometry and therefore fractal models are employed for this purpose. Mandelbrot [116] was the first to propose that fractal geometry could be used for the description of surfaces in nature. Moreover, according to Majumdar and Bhushan [117] there are two parameters that are important for the characterisation of a fractal surface: the fractal dimension $D$ and a scaling constant $G$ which is called roughness parameter.

One of the most common models for modelling 2-dimensional rough profiles is the Weierstrass-Mandelbrot function [118]:

$$z(x) = G^{(D-1)} \sum_{n=n_1}^{\infty} \frac{\cos(2\pi\gamma^n x)}{\gamma^{(2-D)n}}$$

Eq. 3.18

where $G$ is the roughness parameter, $1 < D < 2$ the fractal dimension and $\gamma > 1$ is a parameter controlling the roughness frequency and scaling. It has been shown that 1.5 or 5 are two suitable values of $\gamma$ for the generation of random roughness profiles. In Eq. 3.18 $n$ is the number of cosine shapes used and the created surface will be perfectly fractal if $n_{max} \rightarrow \infty$.

The Weierstrass-Mandelbrot model has been generalised to many variables by Ausloos and Berman [119] who used fractals for the description of surfaces characterised by 3-dimensional rough profiles in both large and small scales and developed a formula called "Multivariate Weierstrass-Mandelbrot" function:

$$z(x, y) = C \sum_{m=1}^{M} \sum_{n=0}^{n_{max}} \gamma^{(D_s-3)n} \left\{ \cos \Phi_{m,n} \right.$$

$$\left. - \cos \left[ \frac{2\pi\gamma^n \sqrt{x^2 + y^2}}{L} \cos \left( \tan^{-1} \left( \frac{y}{x} \right) - \frac{\pi m}{M} \right) + \Phi_{m,n} \right] \right\}$$

Eq. 3.19

$$C = L \left( \frac{G}{L} \right)^{D_s-2} \left( \frac{\ln \gamma}{M} \right)^{1/2}$$

where $2 < D_s = D + 1 < 3$ is the fractal dimension, $G$ is the roughness parameter, $\Phi_{m,n}$ is a $m \times n$ matrix to generate random phase, $L$ is the image size, $\gamma$ is a constant controlling the amplitude and frequency of the cosine shapes, $n_{max}$ is the number of the cosine shapes used to generate the surface profile and $M$ is the number of ridges used. Similar to the 2-dimensional W-M function, the generated surface will be perfectly fractal as $n_{max} \rightarrow \infty$. An appropriate number of cosine shapes can be selected using the following equation:

$$n_{max} = int \left[ \frac{\log(L_{MAX}/L_{MIN})}{\log \gamma} \right]$$

Eq. 3.20

where $L_{MAX}$ is the sample length and $L_{MIN}$ is the period length of the cosine shape with the highest frequency value. The multivariate W-M function has been widely used in contact theory ([120]–[122]).

By observing Eq. 3.19 it can be seen the roughness amplitude increases with increasing the roughness parameter $G$ and consequently the constant $C$. However, the effect of the fractal dimension value on the surface profile is slightly more complicated (Figure 3.9). The fractal dimension is indicative of the frequency of the components participating to the surface profile. For higher fractal dimension high-frequency components are more dominant than the low-frequency ones and vice versa. Moreover it can be seen that the roughness amplitude increases with reducing fractal dimension.

a)
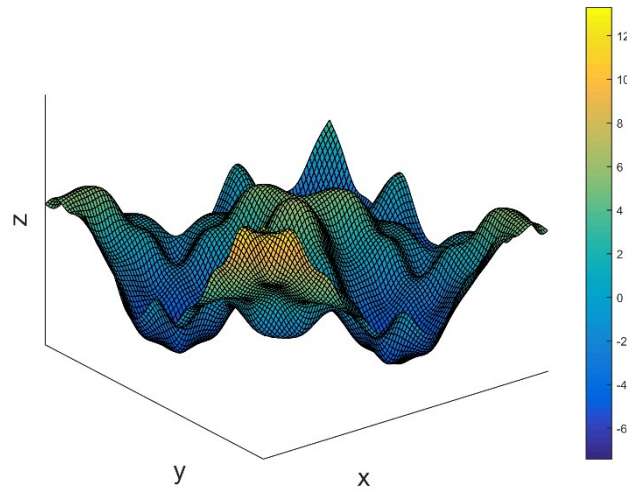
b)
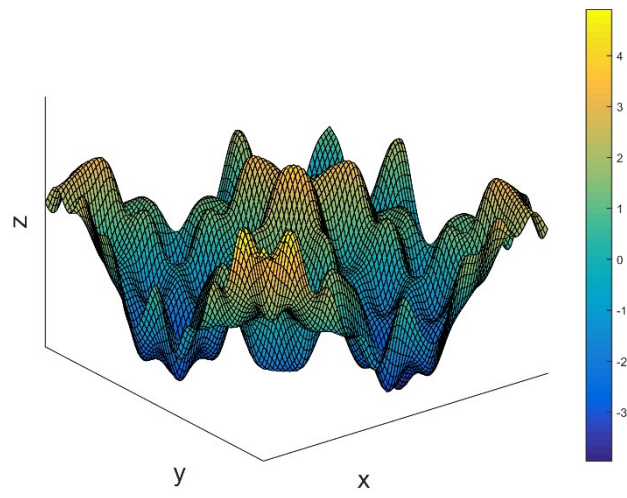
c)
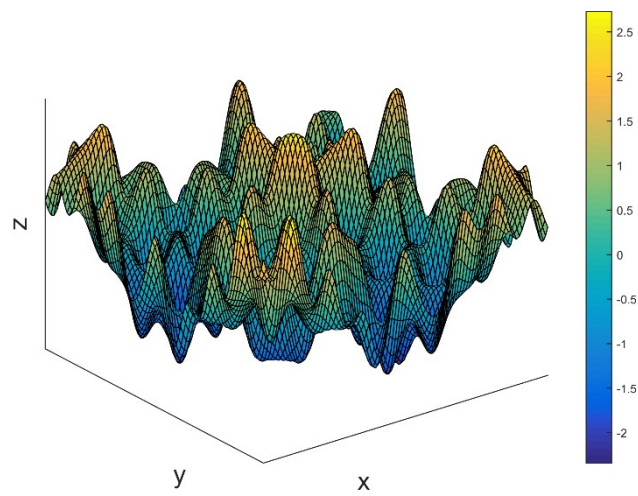
**Figure 3.9:** Effect of fractal dimension on the generated surface: a) $D_s$=2, b) $D_s$=2.5 and c) $D_s$ =3

# 3.3 Methodology

## 3.3.1 Introduction

In this paragraph we will describe the methodology implemented for our Molecular Dynamics simulations. More specifically we will define the following details for each simulation:

- Characteristics of the rough wall topography
- Dimensions of the simulation box
- Interatomic potentials
- Flow characteristics
- Thermodynamic properties (temperature, density)
- Run parameters (timestep, total duration etc.)
- Methods for the calculation of the results

## 3.3.2 Slip length

Our model for the estimation of the slip length in rough nanochannels consists of liquid argon confined by two solid walls (Figure 3.10). The dimensions of the simulation box in the $x$, $y$ and $z$ directions are $L_x = 18\sigma$, $L_y = 43.5\sigma$, and $L_z = 18\sigma$ respectively. The walls are normal to the $y$ direction, and periodic boundary conditions are used in the coplanar directions (i.e. $x$ and $z$).
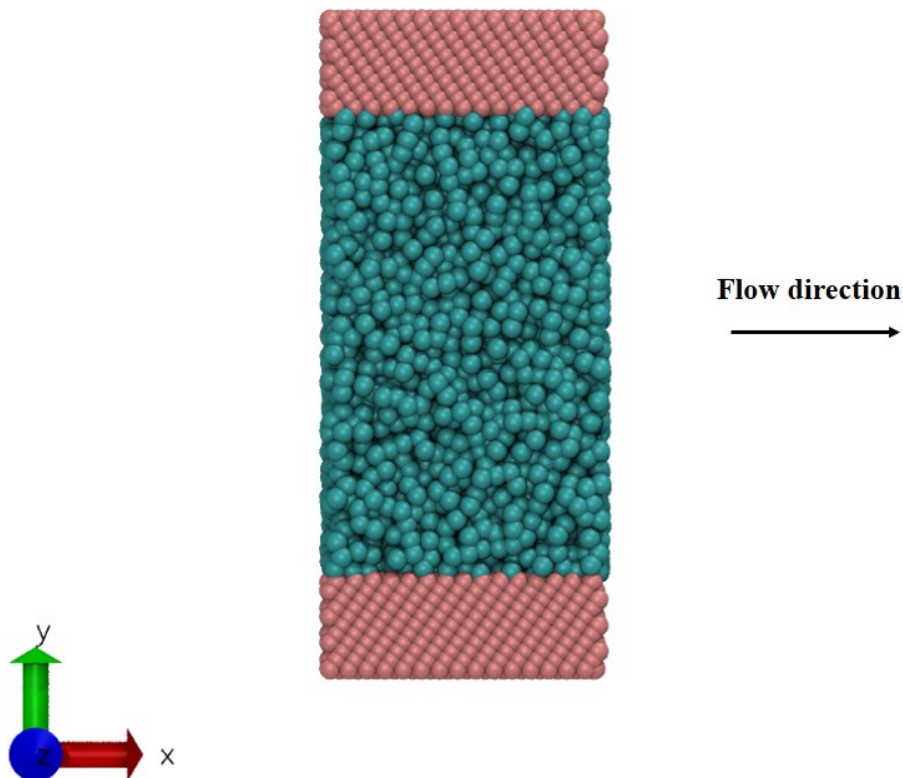


**Figure 3.10:** Simulation box

The multivariate W-M function (Eq. 3.19) has been used for the generation of the rough walls. More specifically, starting with a block of atoms, we calculated the W-M function and defined the centreline for all the rough profiles. Solid atoms on the outer side of the calculated surface (i.e. closest to the liquid) were deleted. It has to be mentioned that the solid atoms of the initial block were placed on a FCC lattice with the (111) plane direction parallel to the $xz$ plane and consequently to the flow direction. The second nanochannel wall was generated by mirroring the first one with respect to a midline. The roughness on the inner solid surfaces differs between the cases examined (Figure 3.11).
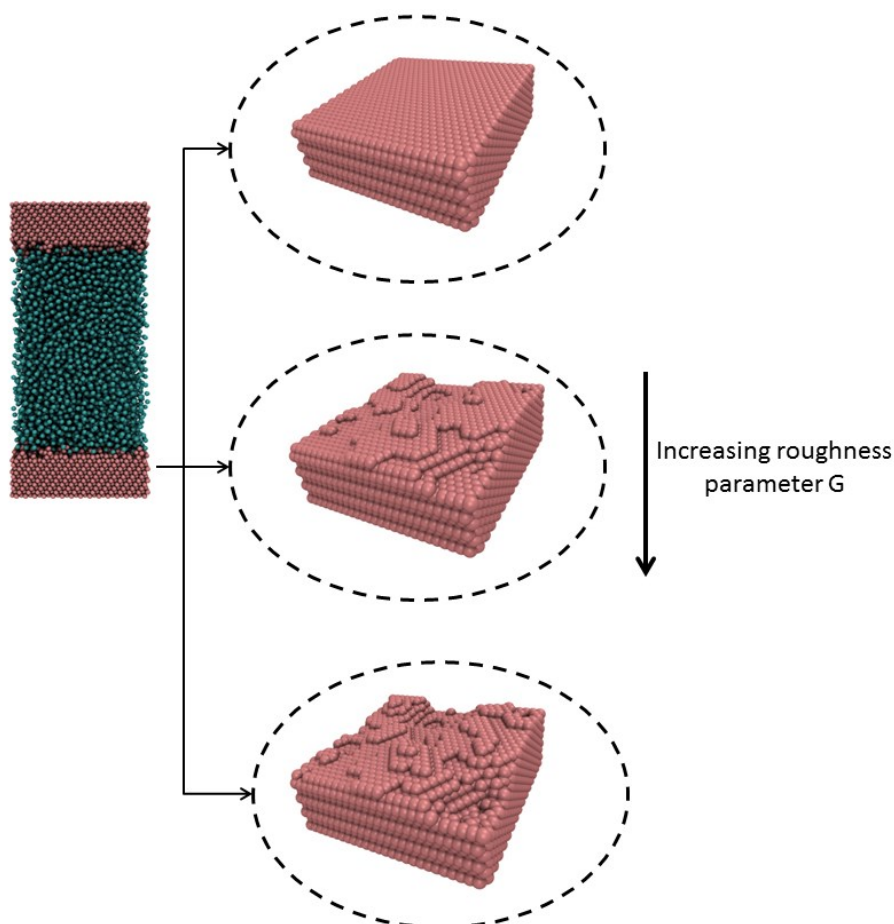


**Figure 3.11:** Our MD model illustrating liquid argon (cyan) confined by two solid walls (pink). The circled surfaces to the right show walls of different depths of roughness, obtained by adjusting the roughness parameter G

After preparing the walls, we randomly placed liquid atoms between them. Due to the complex nature of the wall geometry, we used dynamic Voronoi tessellation on the position of the atoms to calculate the volume of the channel. In turn, the number of liquid atoms varied between cases to keep a constant density of $\rho = 0.84 \, \rho\sigma^3$. The particle interactions were modelled using the 12-6 Lennard-Jones (LJ) potential:

$$v_{ij}^{LJ}\left(r_{ij}\right) = 4\varepsilon \left[ \left(\frac{\sigma}{r_{ij}}\right)^{12} - \left(\frac{\sigma}{r_{ij}}\right)^{6} \right]$$

Eq. 3.21

The LJ parameters for the liquid interactions are $\varepsilon_f = 1\varepsilon$ and $\sigma_f = 1\sigma$. The strength of the solid-liquid interaction, $\varepsilon_{wf}$, is of interest to this study and ranges between $0.2\varepsilon \leq \varepsilon_{wf} \leq 0.6\varepsilon$ while the molecular diameter is fixed at $\sigma_{wf} = 0.75\sigma$.

The solid atoms are fixed onto their initial lattice sites through the spring potential:

$$V_s = \frac{1}{2}kr^2 \qquad\qquad \text{Eq. 3.22}$$

where $k$ is the spring stiffness. For all the cases we consider here $k = 500\ \varepsilon\sigma^{-2}$.

To control the temperature of the system, the velocities of the wall atoms were rescaled every timestep. We did not tamper with the liquid atoms as this can result in unphysical behaviour [123]. Following an initial equilibration phase, the temperature of the system was set to $T = 0.72\ \varepsilon k_b^{-1}$. To develop a Poiseuille flow, we applied a force equal to $0.02\ \varepsilon\sigma^{-1}$ in the $x$-direction on all fluid molecules [124]. The timestep of the simulation was set equal to $\delta\tau = 0.001\ \tau$ and the system ran in the microcanonical ensemble (NVE). For the simulations we used the LAMMPS molecular dynamics simulator [125].

## 3.3.3 Shear Viscosity

Similarly to the previous paragraph, our model for the calculation of the shear viscosity consists of liquid argon confined by two silver walls. The dimensions of the simulation box in the $x$, $z$ and $y$ directions are $L_x = L_z = 7.4\ nm$, and $L_y = 14.4\ nm$ respectively. The multivariate W-M function (Eq. 3.19) has been used for the generation of the rough walls which consisted of 11 layers in the smooth wall case. We controlled the roughness amplitude via the roughness parameter $G$ and three wall geometries were examined corresponding to a) $G = 0$, b) $G = 0.75$ and c) $G = 1.5$ (Figure 3.12). We used comparatively large roughness parameters to ensure the distribution of the fluid particles close to the wall and consequently investigate the fluid properties in this region.

The wall atoms were modelled using the EAM potential (Eq. 3.8) and the lattice constant was set equal to 4.086 Å which corresponds to silver. After preparing the walls, we randomly placed liquid atoms between them. The wall-fluid and fluid-fluid interaction was modelled via the Lennard-Jones potential and the interaction parameters are given in Table 3.3. The cutoff distance was set equal to 7.495 Å. The silver and argon masses were set equal to $m_{Ag} = 107.9\ g/mol$ and $m_{Ar} = 39.948\ g/mol$.

| Interaction | $\sigma$ (Å) | $\varepsilon$ (eV) |
|:---:|:---:|:---:|
| Ag-Ag | 2.551 | 0.408 |
| Ar-Ar | 3.405 | 0.0104 |
| Ar-Ag | 2.978 | 0.006 |

**Table 3.3:** Molecular interaction parameters

$G = 0$

$G = 0.75$

$G = 1.5$
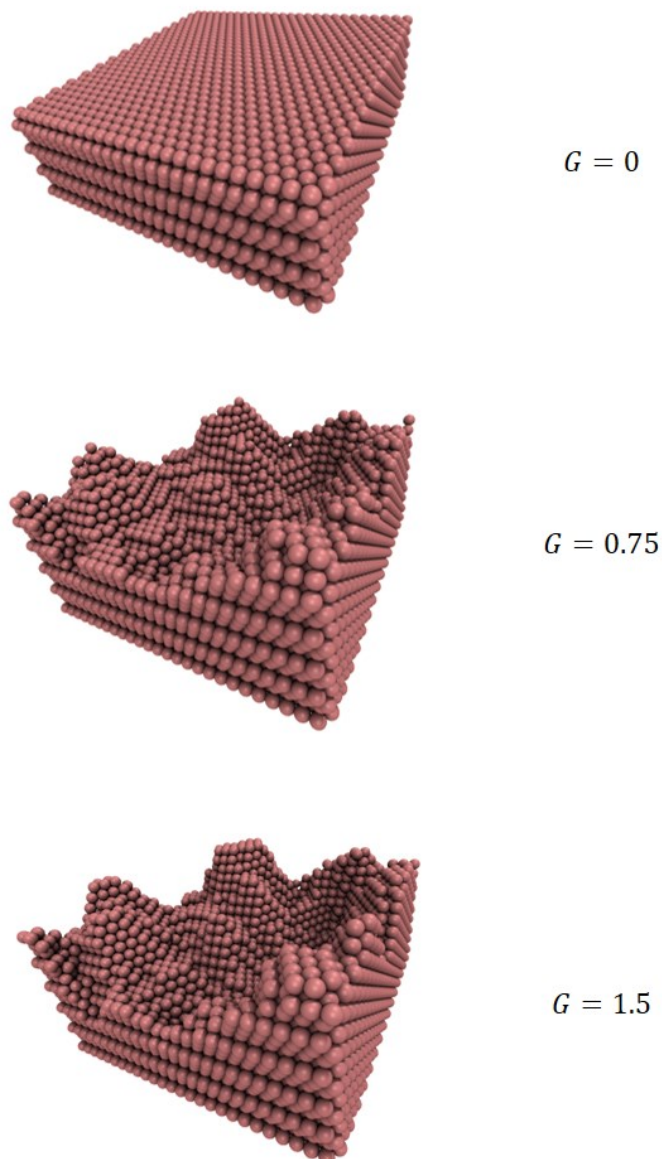
**Figure 3.12:** Nanochannel walls for various values of the roughness parameter G

In order to control the temperature we used the Langevin thermostat. More specifically we applied the thermostat on the first four outmost layers of both silver walls to maintain the temperature of the system at 115 K. The NVE ensemble was used during the equilibration phase and the timestep was set equal to $5 \cdot 10^{-2} \, ps$.

We performed non-equilibrium molecular dynamics simulations in order to simulate the flow. For the estimation of the diffusion coefficient we first calculated the mean square displacement (Eq. A.26). The channel diffusion coefficient was then calculated using Eq. A.27. After the equilibration stage, we applied a force equal to $10^{-5} \, Kcal/(mole \cdot Å)$ on each fluid particle in the x-direction and a Poiseuille flow was developed. In order to calculate the shear viscosity we used the following equation:

$$\eta = \frac{P_{xy}}{\dot{\gamma}} \qquad \text{Eq. 3.23}$$

where $\dot{\gamma} = \frac{\partial u_x}{\partial y}$ is the shear rate. In order to calculate the shear viscosity we divided the nanochannel into 100 bins across the y-direction and the pressure was estimated in each one of them according toEq. 3.24. We also used Voronoi tessellation in order to calculate the volume of each bin $V_{bin}$ due to the complex geometry of the walls.

$$P_{xy} = \frac{1}{V_{bin}} \left[ \sum_{i=1}^{N} m u_{ix} u_{iy} + \sum_{i=1}^{N} \sum_{j>i}^{N} r_{ijx} F_{ijy} \right] \qquad \text{Eq. 3.24}$$

We used the LAMMPS molecular dynamics simulator [125] for the MD runs.

## 3.3.4 Thermal Resistance

The 3-dimensional model we created to study the dependence of the Interfacial Thermal Resistance on the roughness amplitude consisted of liquid argon confined by two silver walls. Rough wall geometries have been generated using the multivariate W-M function (Eq. 3.19). Each wall consisted of 11 layers of particles while the roughness amplitude was determined through the roughness parameter $G$. Three wall geometries corresponding to a) $G = 0$, b) $G = 0.4$ and c) $G = 0.8$ were generated for the purposes of this study and the dimensions of the simulation box in the $x$, $z$ and $y$ directions were set equal to $L_x = L_z = 7.4\ nm$, and $L_y = 14.4\ nm$ respectively.

The interaction between the wall atoms was modelled using the EAM potential (Eq. 3.8) and the lattice constant was set equal to 4.086 Å which corresponds to silver. The liquid atoms were placed randomly between the walls and the interaction between them was described with the 12-6 Lennard-Jones potential. The same interaction potential has been used for the wall-fluid interaction while three different wettability cases were examined: a) $\varepsilon_{wf} = 0.002\ eV$ b) $\varepsilon_{wf} = 0.004\ eV$ and c) $\varepsilon_{wf} = 0.006\ eV$. The parameters for the fluid-fluid and wall-wall interaction are presented in Table 3.4. The cutoff distance was set equal to 7.495 Å and the silver and argon masses were set equal to $m_{Ag} = 107.9\ g/mol$ and $m_{Ar} = 39.948\ g/mol$. Due to the complex nature of the wall geometry, we used dynamic Voronoi tessellation on the position of the atoms to calculate the volume of the channel. In turn, the number of liquid atoms varied between cases to keep a constant density of 1.4 $g/cm^3$.

| Interaction | $\sigma$ (Å) | $\varepsilon$ (eV) |
|:---:|:---:|:---:|
| Ag-Ag | 2.551 | 0.408 |
| Ar-Ar | 3.405 | 0.0104 |

**Table 3.4:** Molecular interaction parameters

To control the temperature over the simulation box we used the Langevin thermostat which was applied on the first four outmost layers of both silver walls. In order to study the thermal conductance of the system we induced a temperature difference between the lower and

the upper wall and their temperature was set equal to $T_{low} = 90\ K$ and $T_{high} = 140\ K$ respectively. Before the averaging process the system was equilibrated for $10^6$ timesteps using the NVE ensemble. The timestep was set equal to $5 \cdot 10^{-2}\ ps$.

In order to measure the temperature across the nanochannel we used the equipartition theorem:

$$T = \frac{2}{3Nk_b} \cdot \langle E_{kin} \rangle \qquad \text{Eq. 3.25}$$

where $\langle E_{kin} \rangle$ is the total kinetic energy, $N$ the total number of atoms and $k_b = 1.38 \cdot 10^{-23}\ m^2 kgs^{-2}K^{-1}$ the Boltzmann constant. One can measure the interfacial thermal resistance by estimating the Kapitza length (Figure 3.13) which is given by:

$$L_k = \frac{\Delta T}{\left. \frac{\partial T}{\partial n} \right|_{liquid}} \qquad \text{Eq. 3.26}$$

In Eq. 3.26 $\Delta T = T_{liquid} - T_{wall}$ is the temperature jump at the interface, and $\left. \frac{\partial T}{\partial n} \right|_{liquid}$ is the gradient of the liquid temperature profile. Due to the irregular wall geometry we used the roughness centreline as the boundary between the wall and the fluid region. Therefore the temperature jump was measured at the centrelines of the upper and lower wall regions in the y-direction ($cl_{low} = 4.32\ nm$ and $cl_{high} = 10.08\ nm$ respectively).
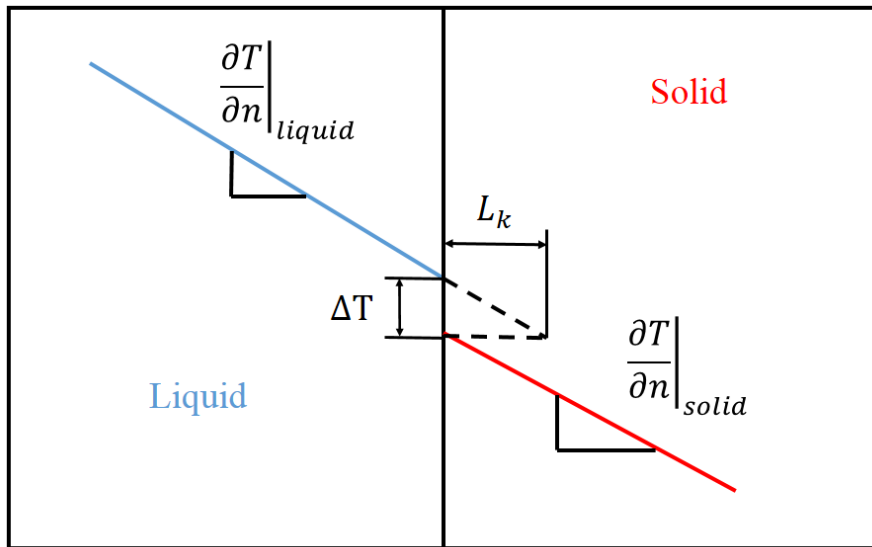


**Figure 3.13:** Schematic representation of the Kapitza length

# 3.4 Validation and Verification

## 3.4.1 Validation

In this paragraph we will try to validate the results obtained from our Molecular Dynamics Simulations. For this purpose, we will use the criteria proposed by van Gunsteren and Mark [126]:

1. The quality of the theory or model
2. The accuracy of the interatomic potential or force field
3. The degree of sampling, statistics and convergence reached in the simulation
4. The quality of the simulation software
5. How competently the simulation software is used

In the following lines we will try to describe how well and accurately our model addresses the issues raised by the above mentioned criteria.

### Quality of theory or model

The Molecular Dynamics simulations performed for this PhD study are 3-dimensional and consequently more accurate than the 2-dimensional ones. This is because they include a larger number of atoms compared to the 2-dimensional simulations, a fact which is very important for the realistic representation of nanochannels and for the averaging procedure (larger sample leads to better averaging). Moreover, our roughness model is 3-dimensional and based on fractals, trying to imitate the self-affinity of natural surfaces. Finally, we have tried to control the temperature of the system by applying thermostats on the wall atoms and not intervening in the motion of the fluid atoms.

### Accuracy of the interatomic potential or force field

As far as the interatomic potential between the argon and the wall atoms is considered we have used the 12-6 Lennard Jones potential which has been proven to be effective for the description of noble gases. In our simulations, we have used two ways of modelling the interaction between the wall atoms. The first one implemented the use of a nonlinear spring potential in order to attach the solid atoms to the sites of a lattice. The second one is based on the EAM potential which accurately reproduces the properties of metals [127].

### Degree of sampling, statistics and convergence reached in the simulation

As discussed in the Methodology paragraph, we performed NEMD simulations. Therefore we have made sure that:

1. The selection of the timestep is appropriate, i.e. large enough to save computer expenses but smaller than the fastest oscillation period of the system.
2. The system has reached equilibrium before applying an external stimulation (force, temperature gradient) to the system.
3. Before performing averaging the system has reached a steady state in order to avoid calculation errors.

4. The averaging time is large enough to capture efficiently the behaviour of the system.

## Quality of the simulation software

We have selected LAMMPS [125], which stands for *Large-scale Atomic/Molecular Massively Parallel Simulator*, as our simulation software. LAMMPS is the most widely applied Molecular Dynamics code nowadays as it provides the user with a number of significant comparative advantages:

1. Open source software
2. Excellent parallel performance
3. Excellent Documentation
4. Incorporation of numerous interatomic potentials and Force Fields
5. Programming flexibility
6. Active online community and support

## Competent use of the simulation software

For this purpose we have carefully selected the input parameters for our simulations based on the results of previous investigations. Table 3.5 shows the references based on which we selected the corresponding parameters.

| Reference | Parameters |
|:---:|:---|
| [115] | Lennard Jones parameters for argon |
| [43] | Spring stiffness for wall atoms |
| [36] | Parameters of EAM potential for silver atoms |
| [124] | Driving force (Poiseuille flow) |

**Table 3.5:** References for parameter selection

# 3.4.2 Verification

Before proceeding to the presentation of our results we will verify our model by comparing it with the results of previous investigations. We will verify our model according to the following three criteria: 1) the liquid structure, 2) the flow behaviour and 3) the shear viscosity. In this way, we will be certain that our model is accurate as far as the rheological properties and the transport coefficients are considered.

In order to verify our model according to the first two criteria determined, we will try to reproduce the results of the Molecular Dynamics simulations performed by Asproulis and Drikakis [43]. Their model consisted of Argon particles confined by two solid walls. The dimensions of their simulation domain are $16.97\,\sigma$, $34.64\,\sigma$ and $6.54\,\sigma$ in the x, y and z direction respectively. They used the 12-6 Lennard Jones potential to describe the interactions between the argon and the wall particles:

$$V_{ij}^{LJ} = 4\varepsilon \left[ \left(\frac{\sigma}{r_{ij}}\right)^{12} - \left(\frac{\sigma}{r_{ij}}\right)^{6} - \left(\frac{\sigma}{r_c}\right)^{12} + \left(\frac{\sigma}{r_c}\right)^{6} \right] \qquad \text{Eq. 3.27}$$

where $r_c$ is the cutoff distance. They wall atoms were attached to the positions of a FCC lattice using a nonlinear spring potential which is described by Eq. 3.22. They controlled the wall temperature using velocity rescaling while a Langevin thermostat was applied to the liquid atoms in the z direction in order not to affect the motion of atoms in the flow direction. Finally a Poiseuille flow was developed by applying a constant force to each liquid particle in the x-direction. The values parameters used in [43] are described in Table 3.6.

| Parameter | Description | Value |
|:---:|:---:|:---:|
| $r_c$ | Cutoff distance | $2.2\ \sigma$ |
| $k$ | Spring stiffness | $600\ \varepsilon\sigma^{-2}$ |
| $\rho_w$ | Wall density | $4\ m\sigma^{-3}$ |
| $\rho_f$ | Fluid density | $0.75\ m\sigma^{-3}$ |
| $\varepsilon_{wf}$ | Wall-fluid interaction parameter | $0.2, 0.4$ and $0.6\ \varepsilon$ |
| $\varepsilon_{ff}$ | Fluid-fluid interaction parameter | 1 |
| $\sigma_{wf}$ | Wall-fluid distance parameter | 0.75 |
| $\sigma_{ff}$ | Fluid-fluid distance parameter | 1 |
| $T_w$ | Wall temperature | $1.1\ \varepsilon k_b^{-1}$ |
| $T_f$ | Fluid temperature | $1.1\ \varepsilon k_b^{-1}$ |
| $f_x$ | Driving force | $0.02\ \varepsilon\sigma^{-1}$ |
| $\Gamma$ | Langevin thermostat friction term | $1.0\ \tau^{-1}$ |
| $\delta t$ | Timestep | $0.001\ \tau$ |
| $N$ | Number of timesteps | $1.2 \cdot 10^6$ |

**Table 3.6:** Simulation parameters used in [43]

In order to verify the accuracy of our model as far as the liquid structure and the flow behaviour are considered we reproduced the simulation performed by Asproulis and Drikakis [43] and compared the density and velocity profiles obtained.

a)

b)
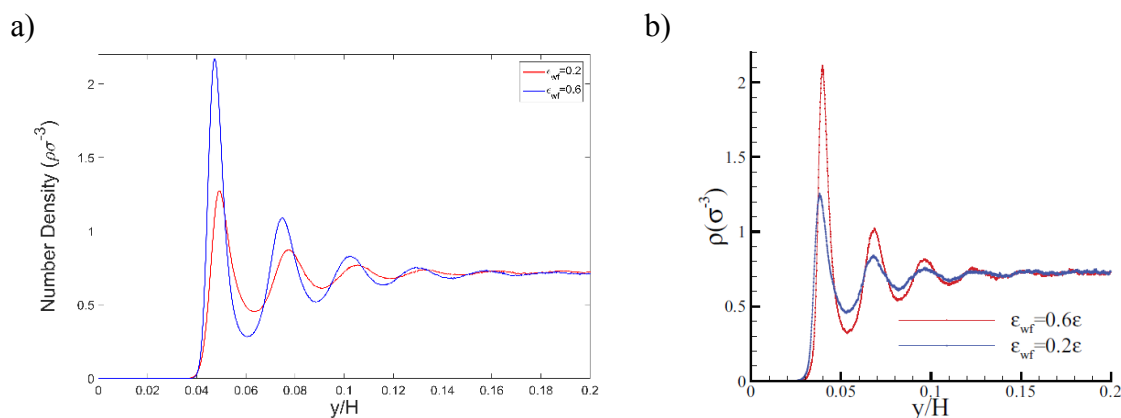
**Figure 3.14:** Density profiles of a) the current model and b) Asproulis and Drikakis [43]

By observing Figure 3.14a & b we can see that the two diagrams are almost identical in terms of maximum density, density in the nanochannel centre and pattern. However, we can see that in Figure 3.14a the density profile corresponding to $\varepsilon_{wf} = 0.2$ is slightly shifted to the right compared to the one corresponding to $\varepsilon_{wf} = 0.6$. This phenomenon can be attributed to the stronger repulsive forces in the case of weaker wall-fluid interaction. However, this

behaviour is not observed in Figure 3.14b. We believe that this divergence is because of some variations in the application of the velocity rescaling thermostat.

a)                                                    b)
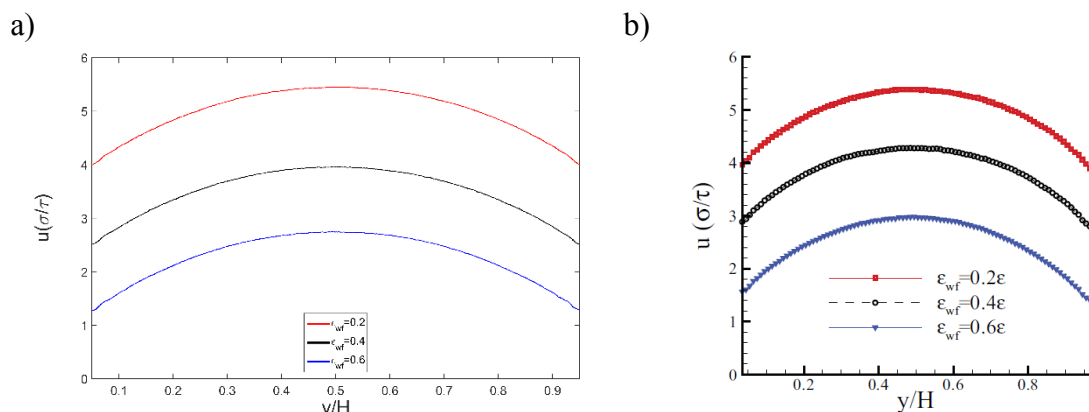


**Figure 3.15:** Velocity profiles of a) the current model and b) Asproulis and Drikakis [43]

In Figure 3.15 we compare the velocity profiles obtained from our simulations with the ones presented by Asproulis and Drikakis [43] and it can be observed that the two diagrams generally agree with the exception that in our model the velocity profiles are shifted slightly downwards compared to the ones of Asproulis and Drikakis. This behaviour is enhanced for higher values of the wall fluid interaction $\varepsilon_{wf}$. We also attribute this behaviour to the way of applying the velocity rescaling thermostat to the walls. In contrast to our model where only the wall atoms are being thermostated, we believe that in the investigation of Asproulis and Drikakis the velocity rescaling thermostat has been applied to the wall region and as a consequence, the motion of fluid atoms intruding this area is affected (and the boundary condition as well). This also explains the increased divergence of the two models for higher values of the wall fluid interaction, as more fluid atoms approach the wall region when the attractive forces become larger.

In order to provide the reader with a complete verification of our model we also focused on the ability of our model to provide accurate results for the transport coefficients of argon. In our model the temperature has been set equal to $115\ K$, the argon density is $1.39\ g/cm^3$ and the estimated shear viscosity at the nanochannel centre is $1.95 \cdot 10^{-4}\ Pa \cdot s$ as presented in Chapter 5. In this context we compared our results with the values of the shear viscosity presented by Heyes [128] for similar conditions (Table 3.6). The reduced units of this study have been converted to real units corresponding to argon using:

- $T = 119.8 \cdot T^* \ K$
- $\rho = 1.6802 \cdot \rho^* \ \dfrac{g}{cm^3}$
- $\eta = 0.9034 \cdot 10^{-4} \cdot \eta^* \ Pa \cdot s$

As shown in Table 3.6 the shear viscosity in our model is higher by 9.74 % compared to [128]. This small deviation can be explained with the slight increase of the shear viscosity due to the confinement which leads to higher pressure. It has to be noted that pressure does not affect the shear viscosity as much as temperature.

|  | **Heyes [128]** | **Our Model** |
|---|---|---|
| **Temperature ($K$)** | 112.61 | 115 |
| **Density ($g/cm^3$)** | 1.34 | 1.39 |
| **Viscosity ($10^{-4}\ Pa \cdot s$)** | 1.76 | 1.95 |

**Table 3.7:** Shear viscosity verification against [128]

## 3.5 Summary

In the beginning of this chapter (Paragraph 3.2) the basic techniques of molecular modelling have been reviewed. The topics covered describe the methodology employed to properly set up a molecular dynamics simulation and the statistical mechanics tools used for averaging during the evolution of the simulation. Moreover, the molecular dynamics techniques for integrating the Newton's equations of motion have been discussed as well as the main thermostating techniques. We have also focused on the Weierstrass-Mandelbrot function which has been widely employed for the description of fractally rough surfaces.

In Paragraph 3.3 we illustrated the methodology followed to setup the MD simulations for each chapter of the results. We presented all of the simulation parameters used including the interatomic potentials, the thermostating methods and the run parameters. Additionally we described the mathematical relationships used for the estimation of our results.

In the end of this chapter we validated our model taking the following criteria under consideration: a) the quality of the theory or model, b) the accuracy of the interatomic potential or force field, c) the degree of sampling, statistics and convergence reached in the simulation, d) the quality of the simulation software and e) how competently the simulation software is used. Finally, we verified our model and our results were found to be in a very good agreement with the results presented by other authors. Based on these facts we can now proceed to the presentation of our results.

# 4  Impact of Roughness on Slip length

## 4.1 Introduction

Disciplines ranging from engineering to medicine are showing increasing interest in micro- and nanoflows. This, along with the technical complications and financial/time expense of appropriate experiments, creates a need for accurate theoretical models. The Navier-Stokes equations, cornerstone of fluid mechanics, can usually make adequate predictions, even at such small scales [129]. For the numerical solution of the equations, Computational Fluid Dynamics (CFD) often employ the no-slip boundary condition that prescribes zero velocity for the fluid directly in contact with a solid surface. Although experiments have found a non-zero fluid velocity over hydrophobic surfaces ([130], [131]), for most applications of industrial interest the slip-length is minor compared to the system's dimensions, justifying such boundary conditions for larger scales. However, in micro- and nanofluidic systems, the slip length can be comparable to the system dimensions in which case the no-slip condition results in an inaccurate description of the flow field.

Molecular models have successfully associated system properties with the velocity slip ([38], [46], [132]). However, most of them consider atomically flawless surfaces, which is unrealistic in view of the limitations of micro- and nano-fabrication techniques to a precision of approximately ten nanometres. Contemplating the irregular nature of a material's surface, subsequent models introduced protrusions onto their solid walls concluding that, as these increase in depth and frequency, the no-slip condition begins to arise ([43], [88], [133]). Although a substantial improvement with qualitatively correct conclusions, the produced geometries are overly simplistic and far from random; the surface roughness was usually produced by extruding trivial patterns from an initially smooth geometry.

A more accurate model used fractal theory to design a complex and randomly prepared roughness on the walls of a two-dimensional channel [81]. The authors varied the fractal dimension, a parameter quantifying the ability of a fractal to fill up space, to adjust the complexity of the walls: the larger the fractal dimension, the smoother the surface of the walls. The paper concluded that the velocity at the boundary decreases as the complexity of the wall geometry increases, even if the depth of the cavities are statistically the same. Despite the important outcomes of the investigation, we believe that the roughness in the spanwise direction in a real channel significantly supplements the effects of the streamwise roughness. As a result, a two-dimensional model might not be able to fully capture the effects of surface roughness on the fluid slippage.

In this chapter the boundary velocity of a flow over a three-dimensional, fractal-based surface will be investigated. Qualitatively agreeing with previously published data, we observe that introducing surface roughness significantly reduces the fluid velocity. We show that this decrease is a result of additional shear stress, induced by a break-up of the liquid strata, found

close to smooth solid surfaces, into a discontinuous and random array of obstacles. Finally, we compare the three-dimensional model with its two-dimensional parallel. This juxtaposition reveals that the two-dimensional model underestimates the slip-length, justifying our initial assumption, and strongly suggesting that future studies should use roughness models of three-dimensional character.

## 4.2 Results

First, we investigated the fluid velocity across the channel with 3 different values of wettability ($\varepsilon_{wf} = 0.2\varepsilon$, $\varepsilon_{wf} = 0.4\varepsilon$, $\varepsilon_{wf} = 0.6\varepsilon$), for different depths of roughness (Figure 4.1). All cases demonstrate the anticipated parabolic profiles, none of which has a vanishing velocity at the wall. The larger the depth of the roughness, the lower the velocities across the channel. The most notable observation is a five-fold decrease of the boundary velocity as we introduce roughness ($G = 0.005$) onto the smooth channel ($G = 0$). Although increasing the depth of the roughness further decreases the fluid velocity, the mere existence of surface irregularities seems to be the dominant factor. As wettability increases the maximum velocity corresponding to each value of the roughness parameter decreases.

a)



b)



60
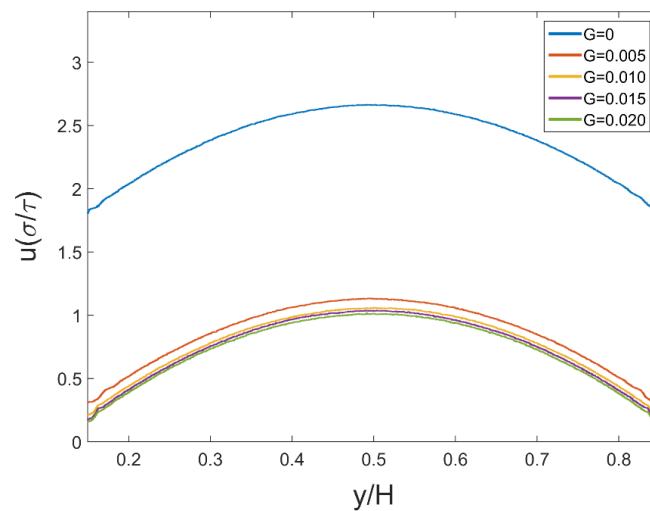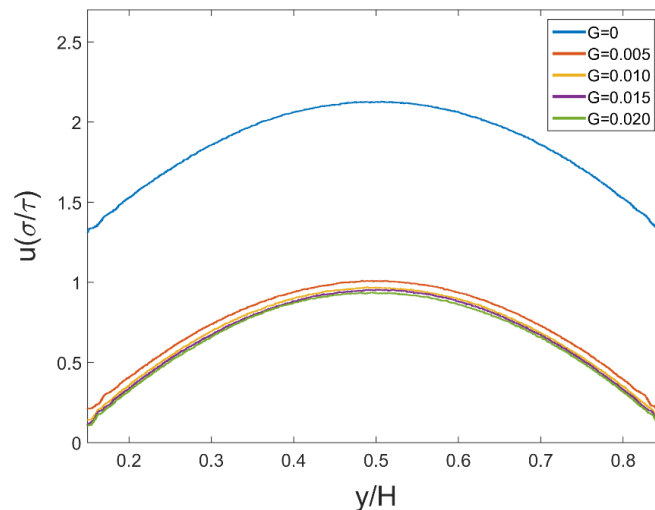
c)
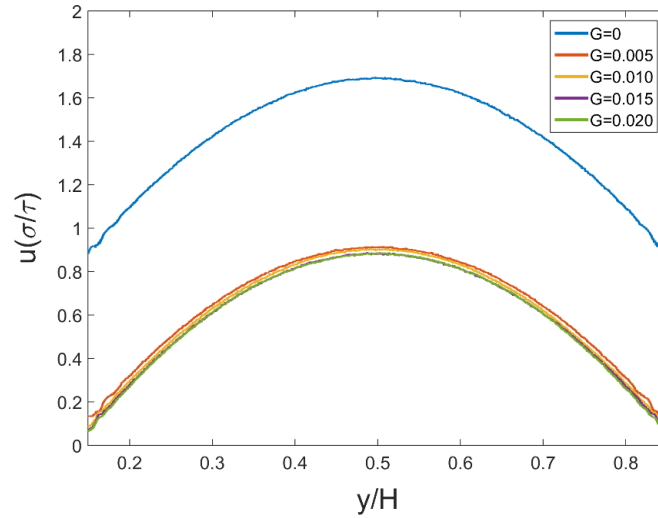


**Figure 4.1:** Fluid velocity through a channel with a) $\varepsilon_{wf} = 0.2\varepsilon$, b) $\varepsilon_{wf} = 0.4\varepsilon$ and c) $\varepsilon_{wf} = 0.6\varepsilon$. The different curves correspond to a roughness of different depth, with $G = 0$ corresponding to a perfectly smooth wall and $G = 0.02$ corresponding to the wall with the deepest protrusions considered here. As we introduce roughness on the initially smooth geometry, the velocity profiles experience a large reduction. Although this decrease continues with increasing roughness depth, it continuously becomes less significant.

Before proceeding with an in-depth analysis of these results, we studied how the wetting properties of the solid change the effect of the roughness on the fluid flow. We know from previous studies on smooth walls (which we validate ourselves in Figure 4.2a), that increasing the wettability of the solid is accompanied by a decrease in the boundary velocity [132]. Our results additionally show that, regardless of the type of wall used, introducing roughness reduces the velocity substantially (Figure 4.2b & c). In fact, a visual inspection, which we refine more rigorously later, suggests that the same change in roughness depth decreases the velocity proportionally, for all levels of wettability (i.e. for all wetting properties, the boundary velocity is reduced by approximately 15 times when transitioning from the smooth to the roughest channel). Therefore, the choice of channel material has little or no effect on how the roughness affects the fluid flow.

a)
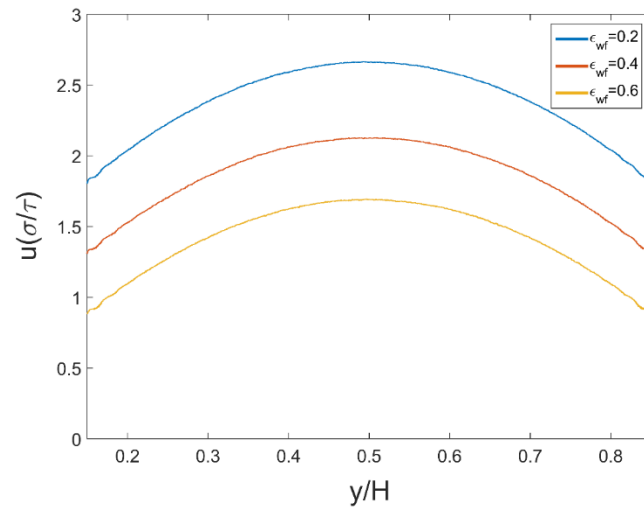


b)
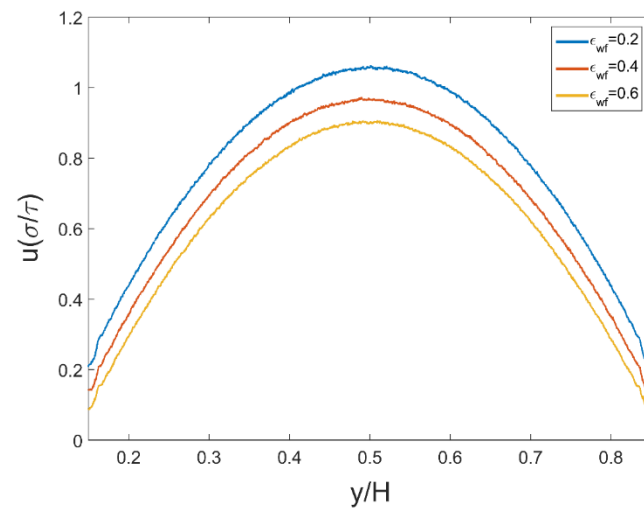


c)
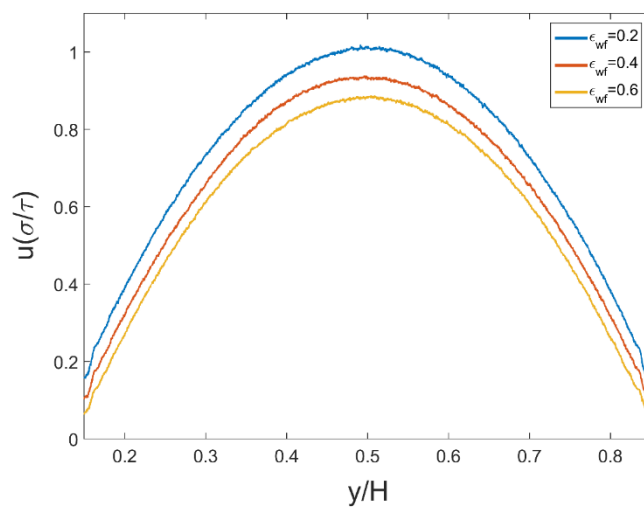


**Figure 4.2:** Velocity profiles of the liquid for different wetting properties of the channel walls with a) G = 0 b) G = 0.01 and c) G = 0.02. As the wettability of the solid increases, the velocity across the channel decreases. The effect of the wetting property of the solid on the velocity profiles is proportionally similar to the case with the smooth walls.

**4.2** Results

To give a quantitative description of the above, we consider how the surface geometry influences the slip-length, the distance past the wall where the extrapolated velocity vanishes. For all the cases we consider, the slip-length decays exponentially with increasing roughness-depth (Figure 4.3). Although studies using trivially patterned surfaces found similar descending trends, the results of their simulations showed a gradual decrease that is more evenly spaced across the various depths they considered [43]. Instead, here, the slip-length experiences a large and sudden jump as we introduce shallow irregularities (i.e. between $G = 0$ and $G = 0.005$). This is followed by a smooth and gradual reduction as the depth increases (i.e. between $G = 0.005$ and $G = 0.20$). We attribute the discrepancy between the two studies to the level of complexity of the employed geometry, which we know to affect the slip-length [88]. For the realistic geometries that we consider, the existence of the roughness has the greatest effect on the fluid flow, not the average depth.

Normalising the slip-length by its value in the smooth channel, $L_0$, reveals a dependence between the wetting properties of the solid and the effect of the roughness on the boundary velocity (Figure 4.4). In channels with higher wettability, the velocity drops faster as the depth of the roughness increases. However, the difference is small and seems to decrease with increasing roughness height.
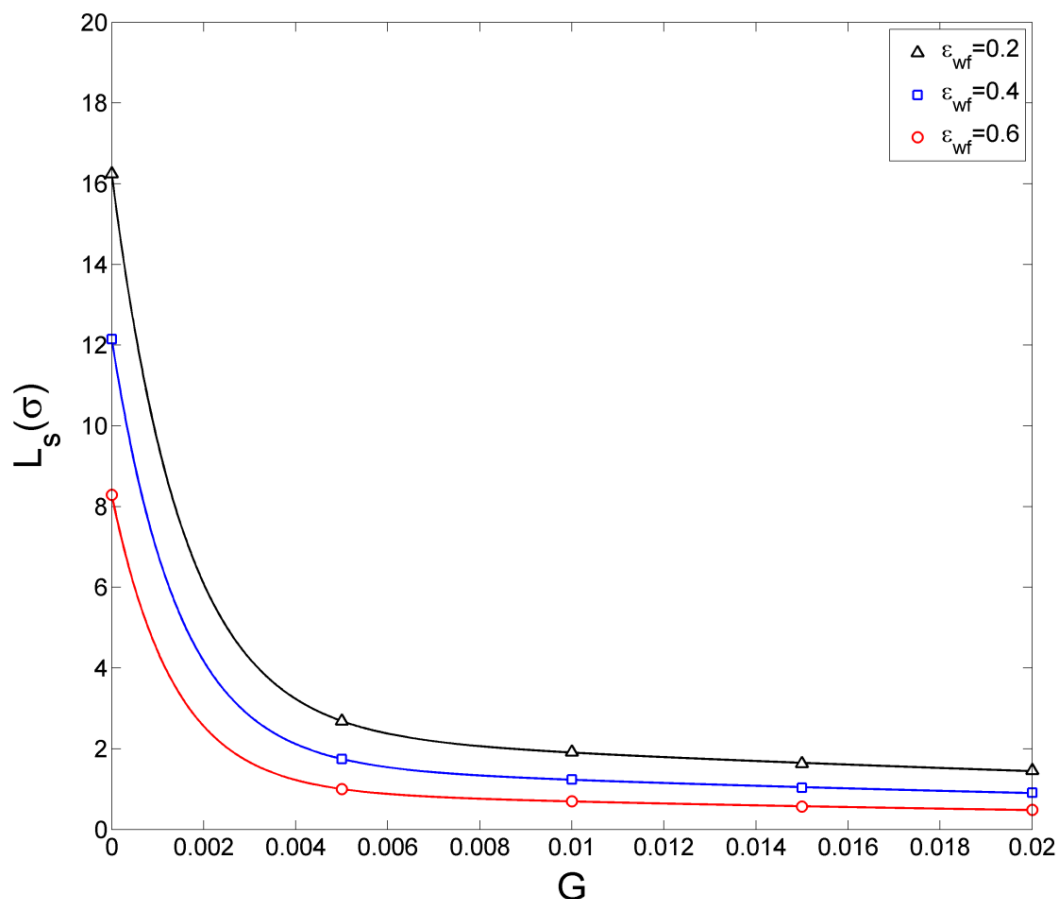


**Figure 4.3:** Slip length vs. roughness parameter G
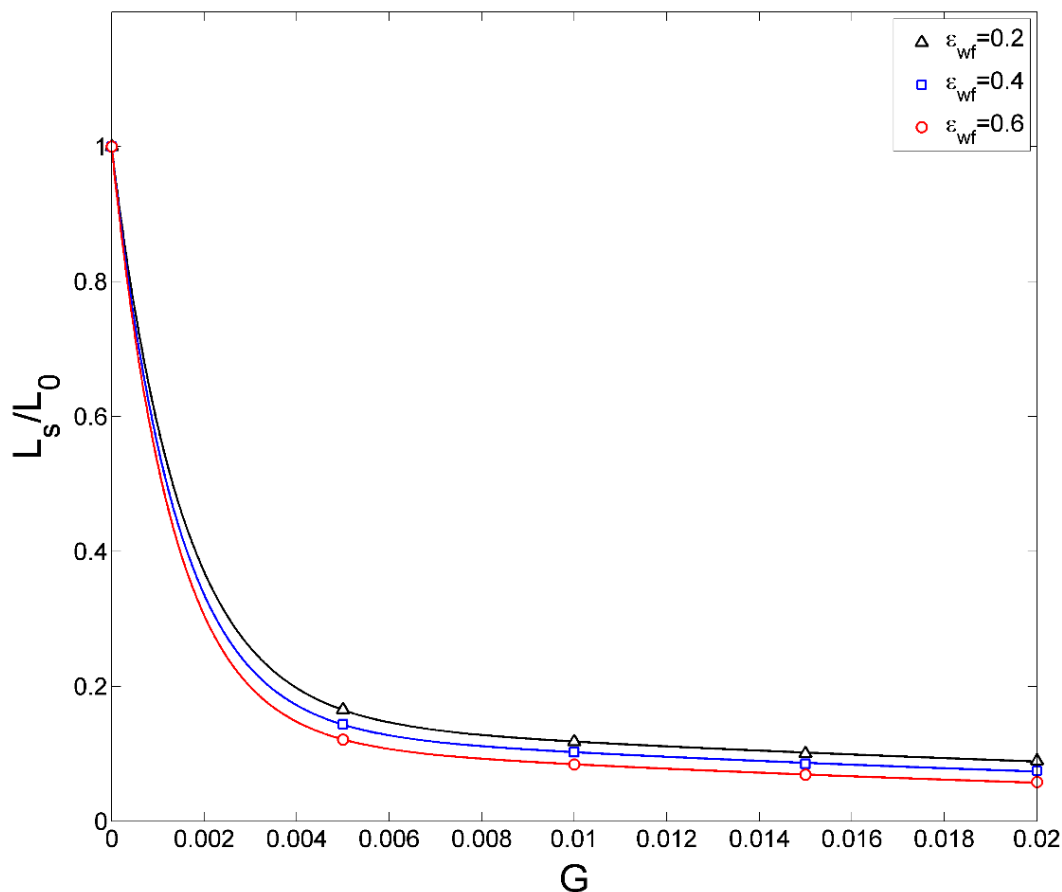
**Figure 4.4:** Normalised slip length vs. roughness parameter G

We now proceed to study the underlying physical processes that link the surface roughness to the flow velocity. More than the absolute associations that we have made so far, such information will allow us to conceptualise these ideas, generalise the concepts to different systems (i.e. different materials) and prepare more accurate theoretical models.

Previous studies have shown that the liquid forms organised layers close to smooth walls, influencing the system's properties, including the fluid slip [44]. We will investigate how these structures change in the presence of a rough wall. As traditionally the case with MD studies on micro- and nanoflows, we initially investigated the fluid structure using one-dimensional density profiles. The expected fluid strata, which translate into density oscillations, appear regardless of the wall geometry and wetting properties (Figure 4.5a, b and c). However, the shape of these layers significantly changes depending on the wall roughness.

Starting with the least wettable nanochannel walls (Figure 4.5a), the smooth case presents well-defined density layers, the first of which begins approximately 1.5 nanometres away from the wall (for the smooth case, the boundary of the wall is located at $y/H \approx 0.133$). This gap suggests minimal contact between the solid and liquid, and a low collision frequency between the two types of atoms. Instead, they interact almost exclusively through the van der Waals forces that are weak for $\varepsilon_{wf} = 0.2\varepsilon$. Therefore, the liquid glides over the solid surface with little resistance; this is the source of the higher boundary velocity.

In rough channels, a minor density peak appears beyond the beginning of the wall, showing that the liquid intruded the solid cavities (In the rough cases, we cannot define one point along the $y$ direction that marks the beginning of the channel. However, the maximum point reached by the lower rough walls is approximately $y/_H \approx 0.146$). The direct contact between the solid and liquid reflects a higher number of collisions at the interface. Macroscopically we interpret this as greater shear stress which is the source of the velocity decrease. A minor digression: it is important to note that this peak is not isolated from the rest of the liquid (as indicated by the non-vanishing density between the two leftmost layers). If that were the case, the trapped liquid would not slow the flow in the channel. Continuing with our analysis, as the depth of the roughness increases, the number of trapped atoms increases by a small amount (compare the curves in Figure 4.5a). This explains the slow decrease of the slip-length following the initial introduction of roughness (Figure 4.3). Further away from the wall, the liquid layers that appear distinct and well separated in smooth channels, lose definition in the presence of irregularities; a few additional peaks are even created in between layers. This increases the viscous forces between the liquid particles, which also contributes to the velocity reduction at the boundary.

a)



b)
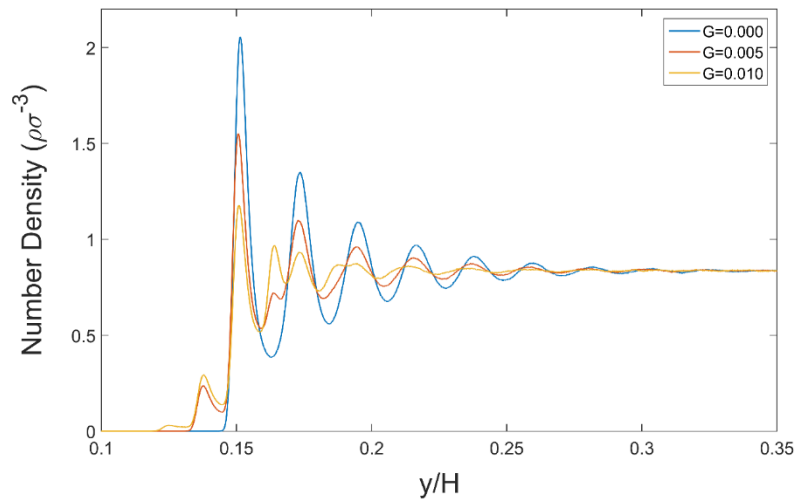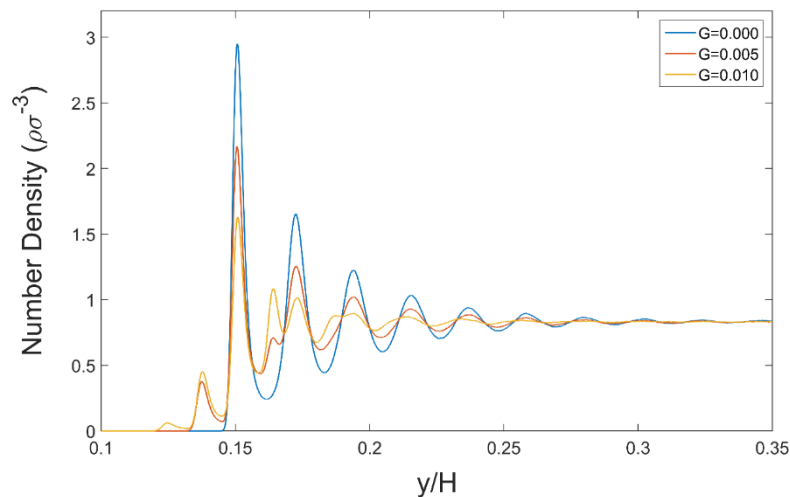
c)
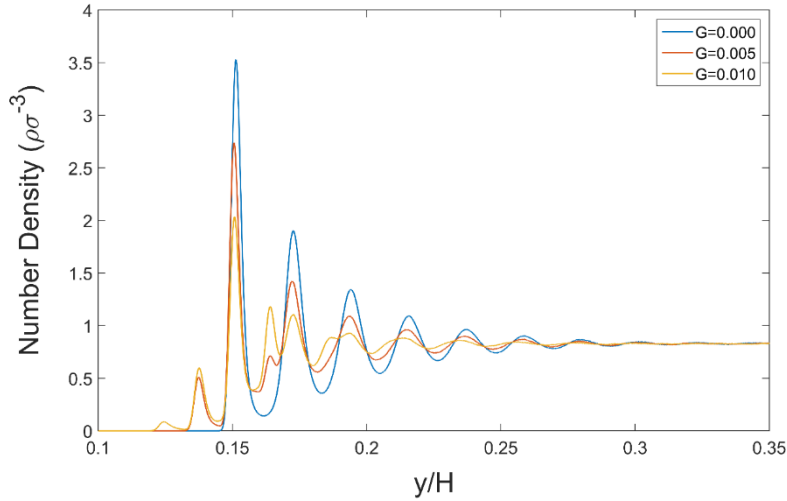


**Figure 4.5:** Density profiles vs. roughness parameter G for a) $\varepsilon_{\text{wf}} = 0.2$ b) $\varepsilon_{\text{wf}} = 0.4$ and c) $\varepsilon_{\text{wf}} = 0.6$

As we increase the adhesive forces (i.e. by increasing $\varepsilon_{wf} = 0.2\varepsilon$ to $\varepsilon_{wf} = 0.4\varepsilon$ and $\varepsilon_{wf} = 0.6\varepsilon$) the walls attract more atoms and the density of all liquid layers almost doubles (Figure 4.5 b & c). When considering smooth walls, the first layer is still at a distance from the wall, similar to the low-wetting case. The number of collisions between the solid and liquid atoms is still quite low. However, the Van der Waals forces are now much stronger which is why the boundary velocity decreases with increasing wettability. As we introduce roughness, the structure of the fluid is affected in a proportionally similar manner to the less wettable channel (i.e. ignoring any numbers, Figure 4.5a, b & c look very similar). The number of atoms directly in contact with the walls, however, increases significantly. We believe this is the source of the dependence of the wetting properties on the effect of the roughness on the slip-length (Figure 4.4).

The one-dimensional density profiles that we consulted so far, provide a visually simple description of the system. However, the spatial averaging in one (for a two-dimensional simulation) or two (for a three-dimensional simulation) directions filters out potentially important information in anisotropic systems. Under the irregular geometries that we consider, the one-dimensional density profiles present two problems. The first lies within the wall cavities, where the bins used for calculating the profiles will contain both, liquid and solid atoms. Since the liquid atoms occupy only part of the volume of this bin its liquid density will be underestimated. Secondly, we cannot expect the non-uniform surface geometry to produce uniform liquid layers. Yet, the averaging along two directions ($x$ and $y$ for our cases) gives the illusion of parallel liquid layers of smaller density.

For a more detailed description of the fluid distribution, we consider three-dimensional density iso-surfaces for the value $\rho = 1.2 \, \rho\sigma^{-3}$ for the channel with the lowest wettability ($\varepsilon_{wf} = 0.2$). In a smooth channel, four parallel and well-spaced surfaces form parallel to the walls (Figure 4.6). These correspond to the four points of intersection that the line $\rho = 1.2 \, \rho\sigma^{-3}$ has in the equivalent one-dimensional density profile. The planes show a

homogeneous and isotropic density in the coplanar directions. This justifies studying one-dimensional profiles for channels with smooth walls.
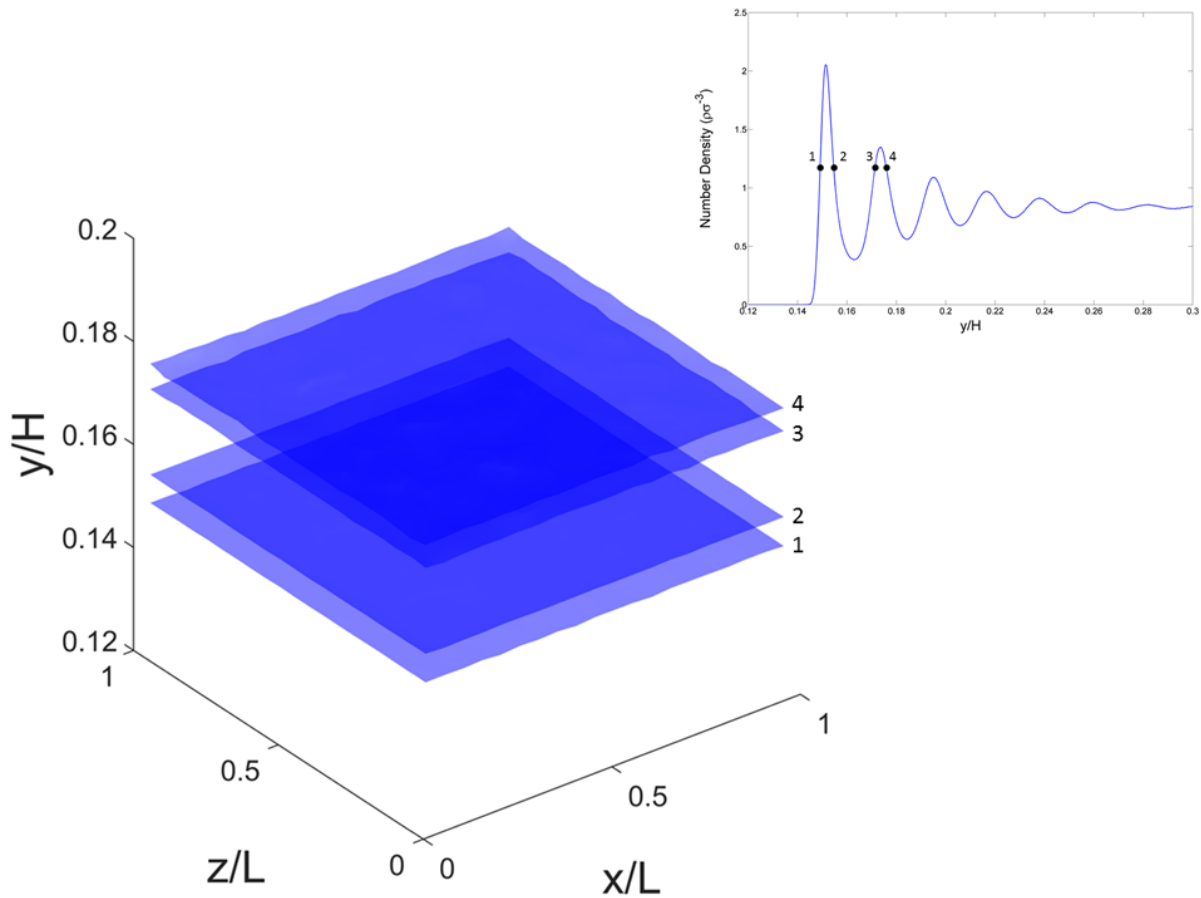


**Figure 4.6:** 1D vs. 3D density profiles for $\varepsilon_{wf} = 0.2$

In the presence of surface roughness, there is no evident structure; the iso-surfaces portray a discontinuous, intertwined collection of patches, oriented at different angles from the wall (Figure 4.7 b & c). The well-ordered planes promoted by the one-dimensional density profiles are an illusion caused by the spatial averaging. In some regions the surface irregularities bridge the formerly-parallel surfaces. This mixing of layers is neatly manifested as pocket-like structures in the iso-surfaces (more evident at the lower values of $y$ close to the intersection point of the $x$ and $z$ axes in Figure 4.7c). The direct contact between the liquid planes increases the shear stress and in turn obstructs the liquid flow. Figure 4.8 depicts the side views of the 3D density profiles of Figure 4.7 to clearly illustrate the mixing of layers phenomenon.

**4.2** Results

a)
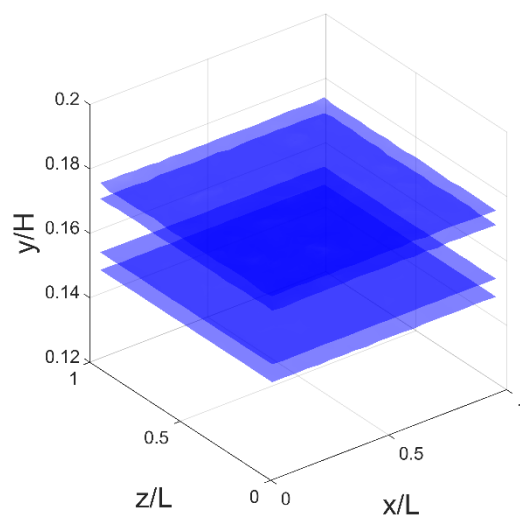


b)
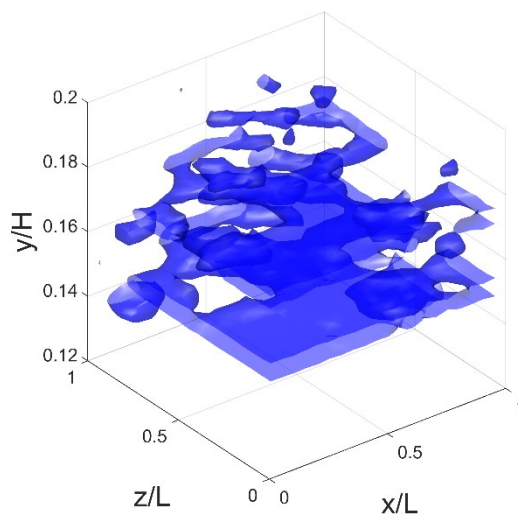


c)
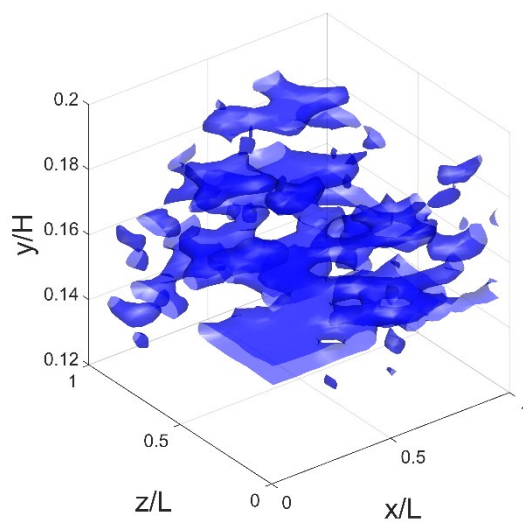


**Figure 4.7:** Perspective views of 3D density profiles for a) G = 0, b) G = 0.05 and c) G = 0.010

a)



b)



c)
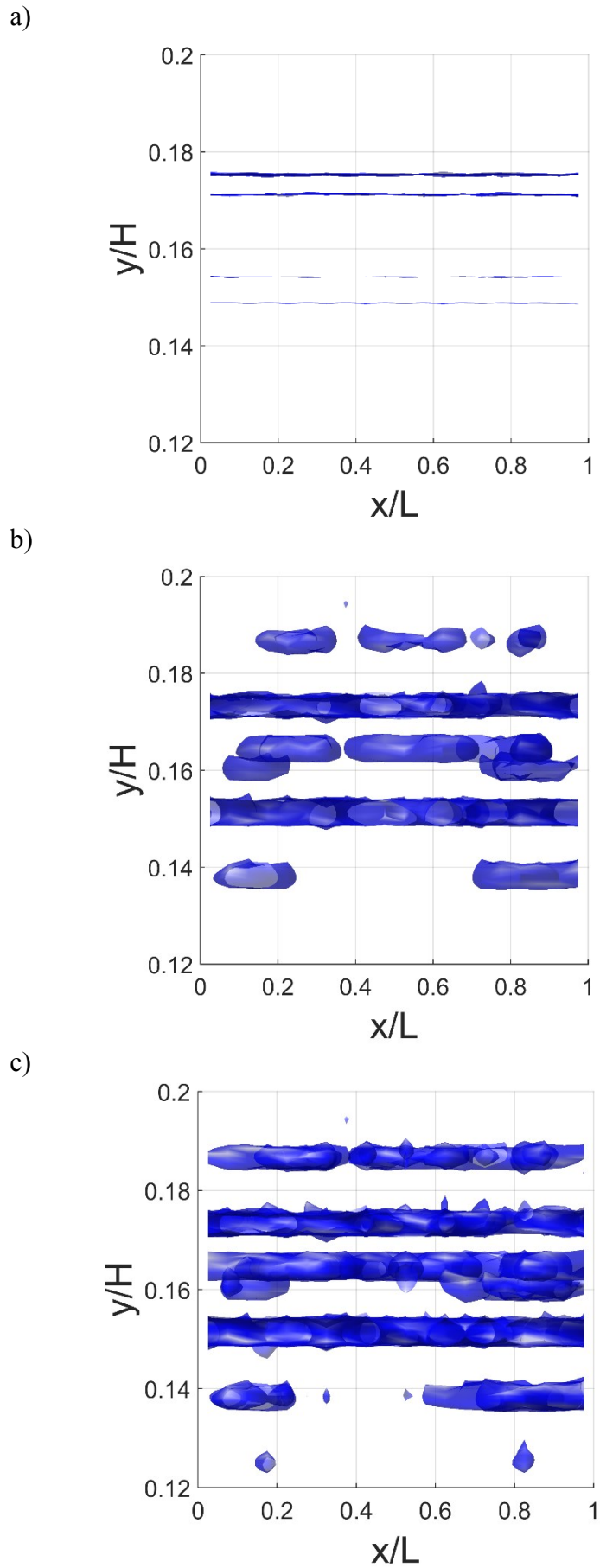


**Figure 4.8:** Side views of 3D density profiles for a) G = 0, b) G = 0.05 and c) G = 0.010

The discontinuous patches in rough channels span a much larger percentage of the width compared to the parallel planes found over smooth surfaces. The particles come much closer, and even enter the wall cavities, leaving no gap between the solid and liquid. In the case of $G = 0.01$ the one-dimensional density profiles completely failed to quantify the extent of packing of the particles in these regions, predicting a maximum density of approximately $0.25 \, \rho\sigma^{-3}$ (Figure 4.5a). Instead, we see that the liquid densities reach (and even go beyond) the value of $1.2 \, \rho\sigma^{-3}$ (Figure 4.7c). Furthermore, the one-dimensional profiles of the equivalent case suggest that high liquid densities are not evident approximately beyond the relative width of 1.2; in reality they extend up to approximately 2.0.

While interpreting the iso-surfaces, it is important to keep in mind that they correspond to a single value of the density. Considering the full spectrum of liquid densities, the structure is even more chaotic with little empty space between the liquid structures. However, the plots become visually unappealing and complicated to interpret which is why we did not directly consider a wider range of values.

Finally, we study whether two-dimensional roughness models are suitable for representing the three-dimensional systems in question. We now use the two-dimensional W-M function (Eq. 3.18) to prepare surface geometries equivalent to the three-dimensional ones. We selected the parameters to yield roughness properties parallel to our three-dimensional cases. Specifically, we changed the fractal dimension to its two-dimensional equivalent, where $D_{2D} = D_{3D} - 1 = 1.5$ (in the 2-dimensional case, $1 \leq D_{2D} \leq 2$). The values of $G$ were also selected accordingly to produce analogous average roughness amplitudes.

In a similar fashion to its three-dimensional counterpart, the slip-length in the two-dimensional model decays exponentially as the depth of the roughness increases (Figure 4.9). The decrease, however, is much more gradual, and more closely resembles the behaviour of the slip in trivially patterned geometries. This shows that the flow field is dependent on the additional surface complexity in the span-wise direction.

This is because each fluid particle has a larger number of surrounding constituents (liquid or solid atoms). The randomness of the irregularities implies that particles can move at different speeds, get derailed from their intended trajectories, collide, and exchange momentum in the span-wise direction. On the contrary, in smooth channels, the isotropy in the directions parallel to the walls gives the system a two-dimensional character. Particles at a similar distance from the wall, move on average with the same speed. Therefore, although collisions do occur, there is no significant change in momentum. This is why the two- and three-dimensional model for smooth channels yield the same results (first point in Figure 4.9).

We believe that ignoring the roughness in the span-wise direction can still produce qualitatively accurate results. The involvement of the surface complexity in the fluid velocity, identified previously by a two-dimensional fractal model [81], is at the heart of the design of our model and the analysis of our results. However, we have shown that roughness has a three-dimensional nature that two-dimensional models cannot accurately capture. We therefore

conclude by suggesting that future studies should seriously consider employing three-dimensional models for a more accurate description of micro- and nano- fluidic systems.
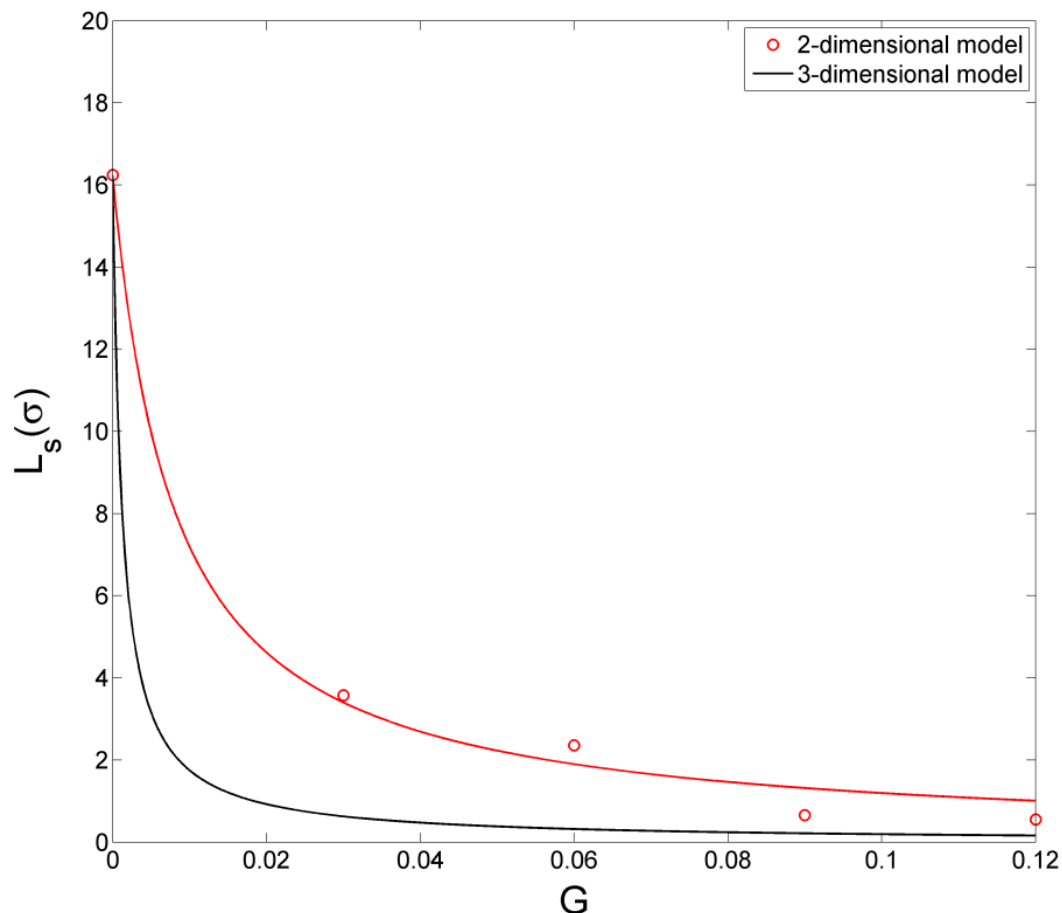


**Figure 4.9:** Slip length as a function of the roughness depth for the two- and three-dimensional models with the same roughness qualities. Although both curves decay exponentially, the slip-length decreases much more gradually in two-dimensional models.

## 4.3 Conclusions

Motivated by the lack of understanding of a fluid's velocity close to a solid boundary, we study how the surface roughness affects the flow field. We use fractal theory to model realistic surface geometries and show that the existence of roughness significantly reduces the boundary velocity. Increasing the depth of the roughness further decreases the velocity, albeit marginally.

We attribute this reduction in velocity to the catastrophic effect that the surface irregularities have on the liquid structure. In smooth channels, the liquid forms parallel, well-spaced layers, with a significant gap between the first layer and the solid walls. The flow finds little resistance due to the reduced contact between the solid-liquid and liquid-liquid particles. On the contrary, the surface irregularities break the ordered fluid planes into discontinuous and chaotic collection of arbitrary-shaped volumes, many of which come close to, and even intrude

the wall cavities. This produces significant friction at the boundary, which results in a reduction in velocity.

Increasing the wettability of the solid results in by a sharp drop in the boundary velocity, regardless of the surface geometry. However, the surface roughness has a slightly greater effect on the decay of the velocity for more wettable geometries. We attribute this to the greater number of fluid particles that enter the wall cavities as the solid-liquid interaction increases in strength.

Finally, through a direct comparison of the results produced by the equivalent two- and three-dimensional models, we conclude that a three-dimensional model is necessary in order to accurately encapsulate the system properties.

# 5  Impact of Roughness on Bulk Properties

## 5.1 Introduction

As discussed in the previous chapter when roughness is introduced to the nanochannel walls the liquid structure close to the walls is greatly affected. The liquid layers observed in smooth nanochannels change their shape when roughness is existent because of the irregularities of the wall geometry. The 3-dimensional density profiles drawn reveal that there is a mixing of layers phenomenon observed close to the walls, where pocket-like structures take the place of well-structured density layers. We showed that the alternation of the fluid structure close to the wall affects the slip behaviour but the observations made pushed us towards the direction of investigating if and how the rough wall geometry affects the transport properties of fluids.

The fluid structure at the vicinity of the rough nanochannel walls has been investigated by a number of researchers by means of Molecular Dynamics simulations. Kim and Darve [134] studied how the rough wall geometry affects the diffusion coefficient of water molecules. They found that the diffusion is anisotropic close to the wall region and obtains reduced values inside the grooves of their sinusoidal wall geometry profile. Studies have also been focused on the effect of rectangular [90] or sinusoidal [79] roughness profiles on the shear viscosity. Jabbarzadeh et al. [79] suggested that the effect of the sinusoidal roughness period on the viscosity is not obvious in contrast to the roughness amplitude which clearly contributes to the enhancement of the viscosity in the vicinity of the walls. Sofos et al. [90] reported that the diffusion coefficient decreases as the number of the wall cavities increases. Moreover they found that the shear viscosity in rough nanochannels is always higher compared to the smooth walls case.

In this chapter we will discuss the effects of fractal roughness on the diffusion coefficient and the viscosity of the fluid. We show that the diffusion coefficient decreases close to the walls as the roughness parameter increases. On the contrary, viscosity increases close to the nanochannel walls and gradually decreases towards the nanochannel centre. Similar behaviour has been observed in experimental investigations [135]. We believe that this behaviour is due to the increase of shear forces in this area and strongly connected to the appearance of pocket like structures and the mixing of layers phenomenon.

## 5.2 Results

First we investigated the mean square displacement (MSD) for the different values of the roughness parameter in all 3 directions (Figure 5.1). The mean square displacement has a rather small value in the y-direction (Figure 5.1b) which is normal to the walls compared to the other two coordinates (Figure 5.1a & c). The reduced mobility of the fluid particles in the y-direction

is because of the non-periodic boundary condition in the y-direction. Moreover, it can be seen that the MSD in the y-direction increases with increasing roughness parameter $G$ contrary to the other two directions. This because as the roughness amplitude increases the layered structure of the fluid in the y-direction is weakened and the mixing of layers phenomenon becomes apparent allowing the atoms to move freely in the y-direction. Moreover, this is because of the increased number of collisions induced by the rough wall profiles. The decreasing MSD in the other two directions is because the trapping time of the fluid particles inside the wall cavities is increased..

a)



b)
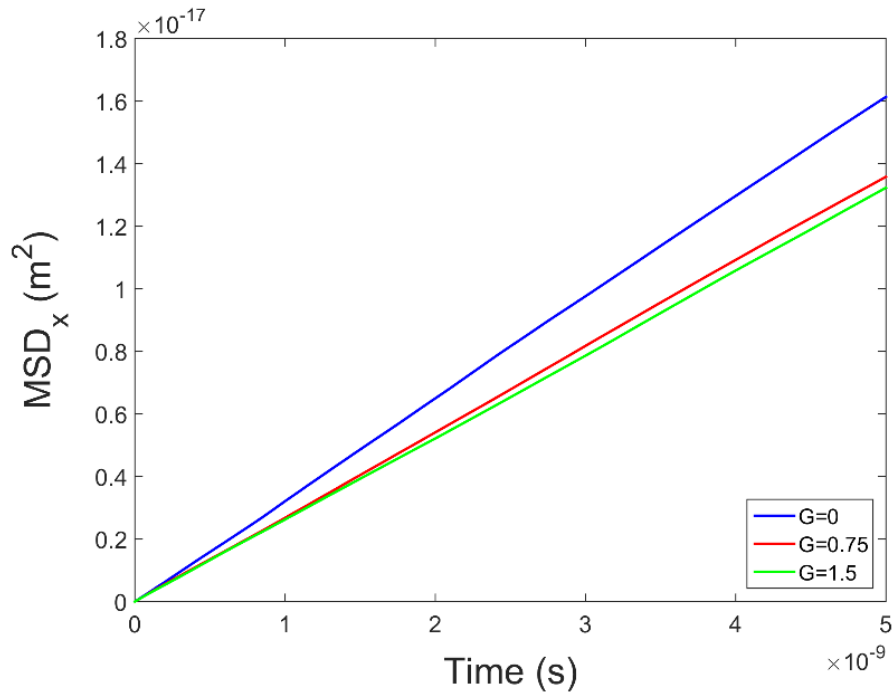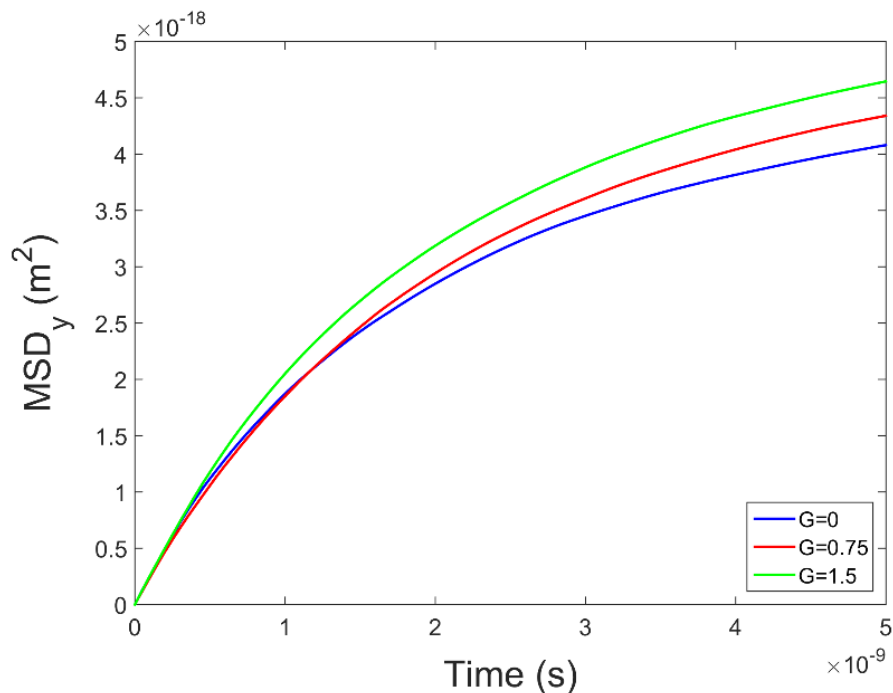
c)
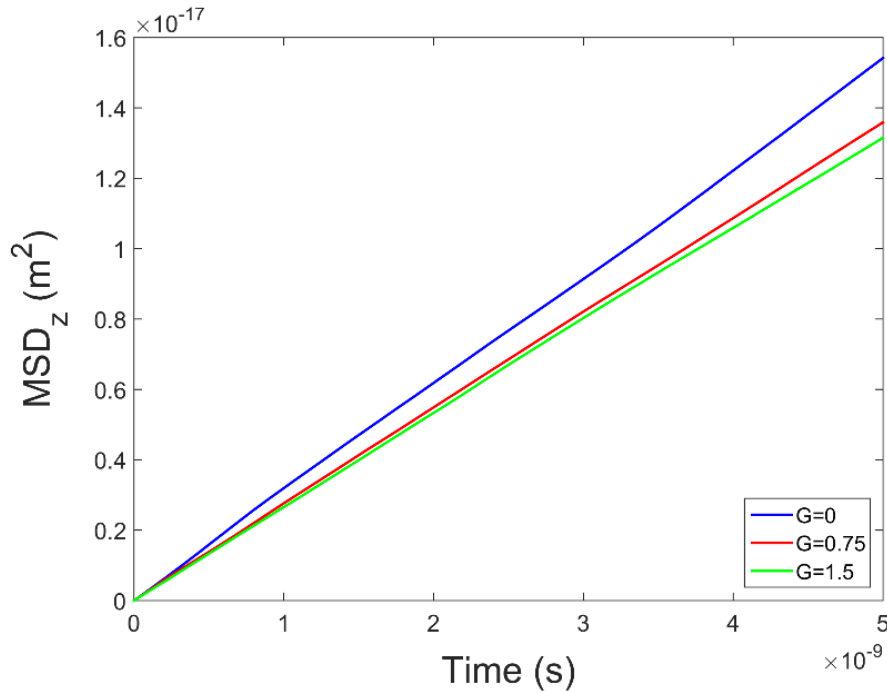


**Figure 5.1:** Mean square displacement in the a) x-, b) y- and c) z- directions

In Figure 5.2 we can see that the channel mean square displacement $MSD_{ch}$ and consequently the diffusion coefficient reduce as $G$ increases. It can therefore be concluded that the increase of the trapping time has a more dominant effect on the mobility of atoms than the mixing of layers phenomenon
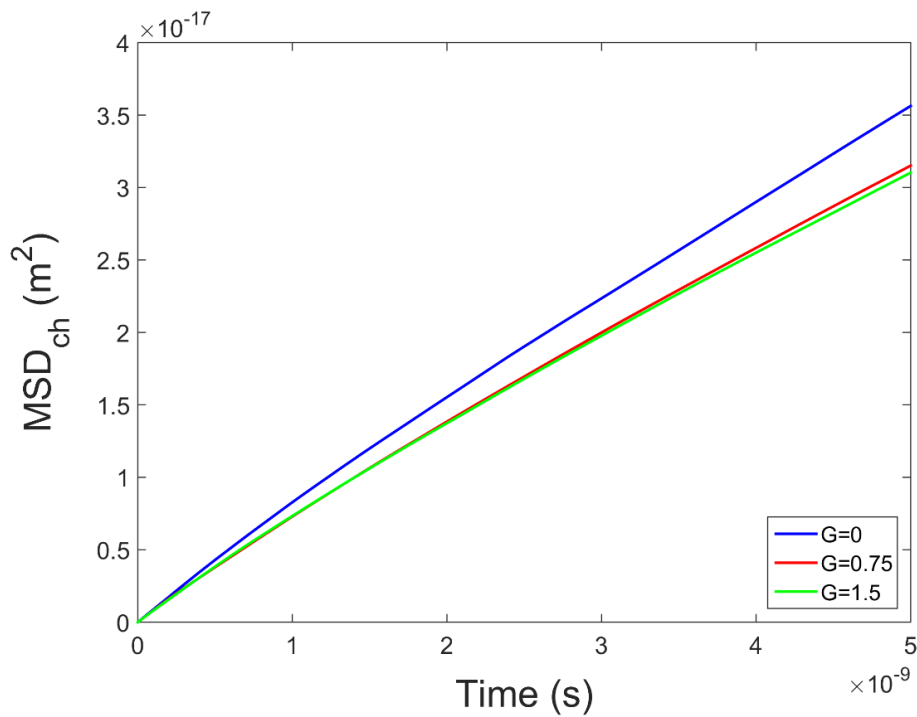


**Figure 5.2:** Channel mean square displacement

**5.2** Results

The next step was to investigate the roughness effect on the diffusion coefficient across the nanochannel. For this purpose we divided the nanochannel in spatial bins in the y-direction and calculated the diffusion coefficient in each one of them. Figure 5.3 shows that the diffusion coefficient has low values in the regions close to the walls and gradually increases towards the centre of the nanochannel in the case of rough walls. When the walls are perfectly smooth the diffusion coefficient is approximately constant across the nanochannel. This result is in agreement with previous findings ([90], [134]) supporting that the diffusion coefficient obtains low values in the vicinity of rough walls.
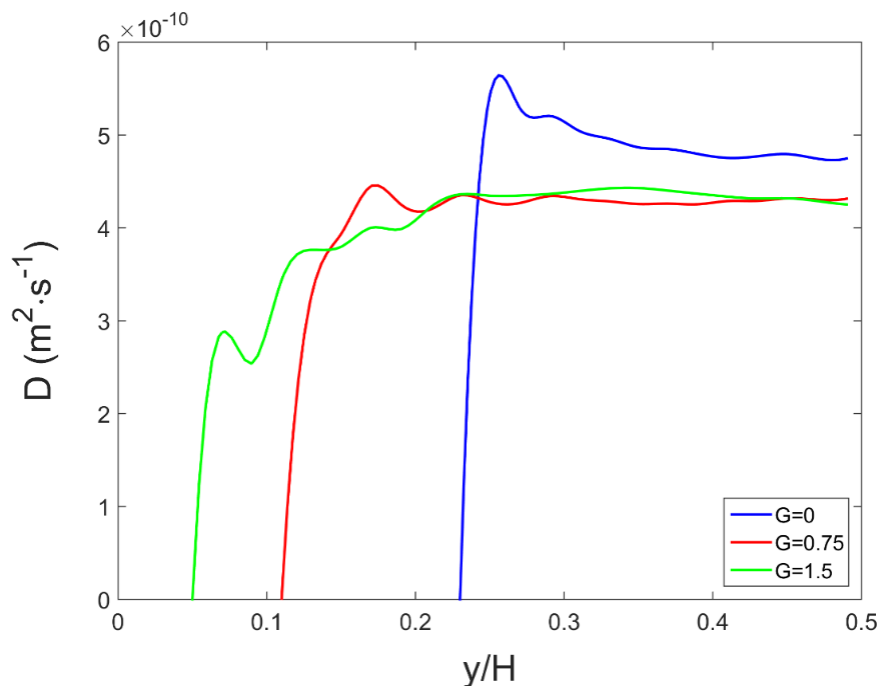


**Figure 5.3:** Diffusion coefficient profile for different values of the roughness parameter G

In order to calculate the shear viscosity we performed spatial averaging in the y-direction in order to estimate the off-diagonal pressure term $P_{xy}$ and the strain rate $\dot{\gamma}$. Our results show that when roughness is introduced to the model the strain rate profile becomes nonlinear close to the walls (Figure 5.4). This implies that for $G = 0.75$ or $G = 1.5$ the velocity profiles cannot be fitted by a parabola at the vicinity of the wall. The non-linearity of the velocity profiles can be attributed to the fact that the irregular topography at the walls imposes some obstacles to the flow and therefore the fluid velocity increases gradually as we approach the centre of the channel.
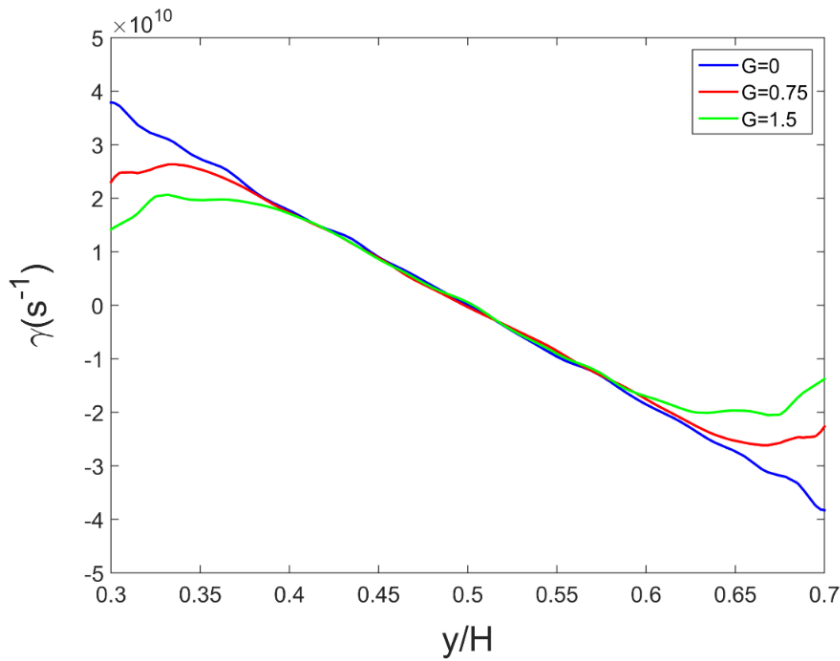
**Figure 5.4:** Strain rate profiles for different values of the roughness parameter G

We estimated the off-diagonal pressure term $P_{xy}$ for each bin in the y-direction using Eq. 3.24. We can observe that the pressure profiles are very similar to the strain rate profiles with the exception that the reduction of $P_{xy}$ as approaching to the wall centreline is less steep compared to the corresponding reduction of the strain rate. The gradual decrease of $P_{xy}$ in the vicinity of the walls is because of the mixing of layers phenomenon. As the roughness parameter increases the layered structure characterised by higher potential energy diminishes and therefore the off-diagonal pressure term $P_{xy}$ obtains lower values close to the walls.
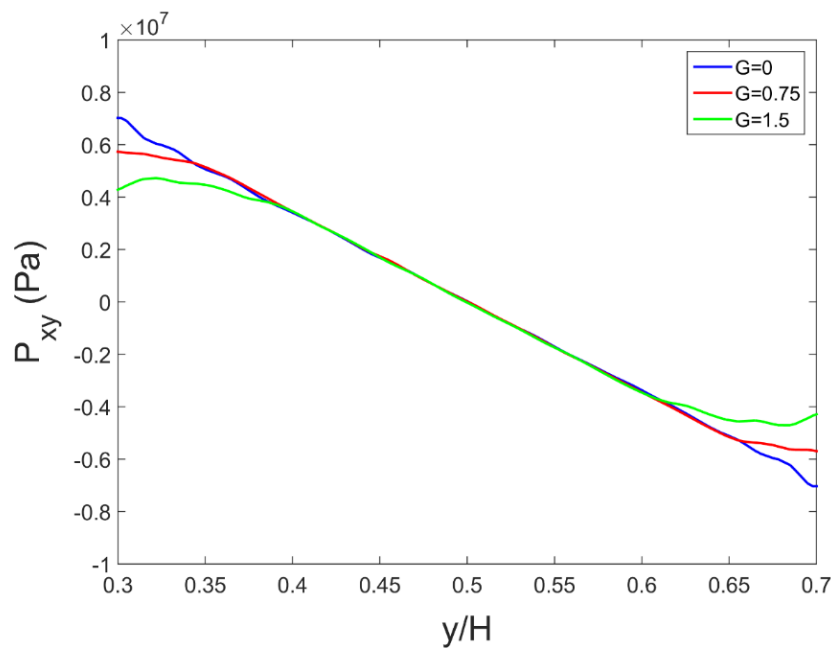


**Figure 5.5:** Pressure profiles for different values of the roughness parameter G

We obtained the shear viscosity across the nanochannel by combining the strain rate and pressure profiles according to Eq. 3.23 (Figure 5.6). We can observe that as the roughness parameter increases, shear viscosity obtains higher values towards the nanochannel walls, a result which is in agreement with the experimental investigations of Mala and Li [89] who proposed a roughness-viscosity model stating that the viscosity near the wall has a higher value and gradually diminishes towards the centre of the channel. The reason for this increase of the shear viscosity in the region close to the walls is the appearance of the pocket-like structures illustrated in Figure 4.7. These closed geometries appearing in the 3-dimensional density profiles suggest that the liquid flow is slightly obstructed in the x-direction compared to the case parallel layers observed in the smooth wall case. Therefore we can conclude that the mixing of layers phenomenon can be considered responsible for the increase of the shear viscosity at those regions.
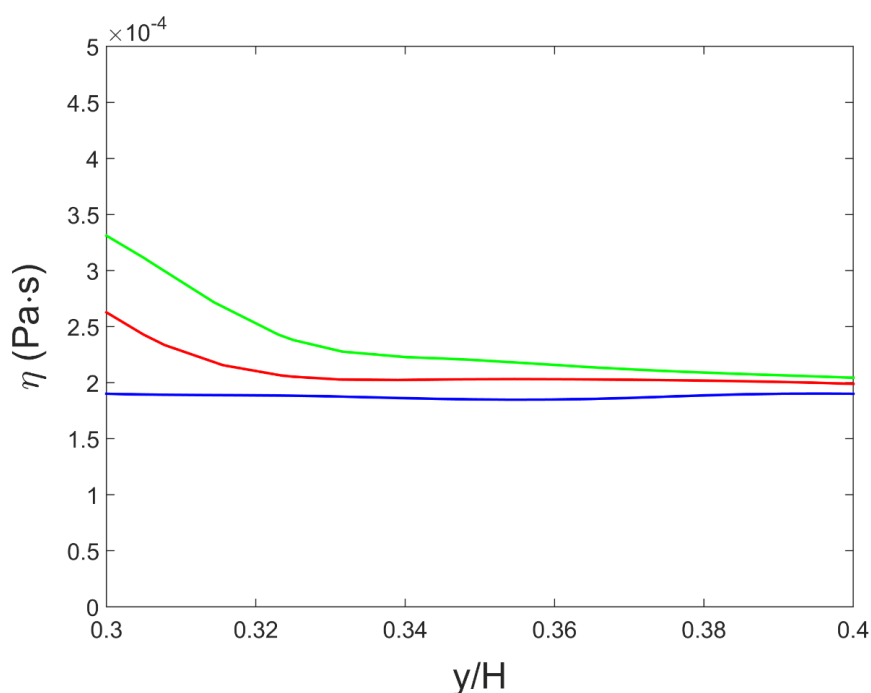


**Figure 5.6:** Viscosity profiles for different values of the roughness parameter G

## 5.3 Conclusions

The results of the fluid flow study presented in Chapter 4 and especially the observation that fluid structure is radically alternated in the vicinity of the walls has been the spark for further investigation of the roughness effects on the fluid behaviour in nanochannels. Therefore we performed non-equilibrium molecular dynamics simulations to study the roughness effects on the shear viscosity. For the description of rough walls we used the multivariate Weierstrass-Mandelbrot function similarly to Chapter 4.

First, we calculated the mean square displacement for different values of the roughness parameter and showed that atoms are trapped inside the wall irregularities leading to a reduction of the MSD in the x- and z- directions in which periodical boundary conditions are applied. Moreover the MSD diagrams revealed that there is an increased mobility of the fluid

particles in the normal to the walls direction for higher values of the roughness amplitude. This is because of the increased scattering due to the wall irregularities. However the channel MSD reduces as the roughness parameter increases. Correspondingly, results showed that the diffusion coefficient is decreased in the vicinity of the walls as the roughness amplitude increases supporting the argument of increased trapping time. Moreover we observed that both the absolute values of the strain rate $\dot{\gamma}$ and the off-diagonal pressure term $P_{xy}$ in those regions decrease for higher values of the roughness coefficient $G$. However the shear viscosity obtains higher values in the vicinity of the walls for large roughness amplitude. This observation has been attributed to the mixing of layers phenomenon which initiates the formation of pocket-like structures replacing the well-structured density layers of the smooth wall case.

# 6  Impact of Roughness on Kapitza length

## 6.1 Introduction

According to classical heat transfer temperature is continuous across the liquid-solid interfaces. However, it has been proven that this assumption does not hold in nanoscale but there is a sudden temperature jump at the solid-liquid interface. This is because there is an interruption in the crystal on which phonons propagate at the liquid-solid interface. Two of the most well-known methods for the investigation of the phonon transport at the fluid-solid interface are the Acoustic Mismatch Model (AMM) and the Diffuse Mismatch Model (DMM) [136].

An alternative but efficient means of studying thermal transport in nanoscale is Molecular Dynamics. Researchers have utilised Molecular Dynamics simulations to study the ITR and the parameters that can affect it. Studies haves shown that the temperature jump reduces with decreasing nanochannel height [137] and that high liquid-solid interaction parameters lead to enhanced thermal conductance [66], [138]). Moreover it has been shown that thermal conductance is significantly affected by the properties of the wall, such as mass and stiffness [139]. Recent studies have also been focused on the effect of rough walls on the ITR in the nanoscale ([93], [94]), and results indicate that thermal conductance is enhanced as the roughness amplitude increases.

In this chapter we use 3-dimensional fractal geometry to describe the nanochannel wall roughness and investigate the thermal behaviour of confined liquids. Similarly to the chapters 4 and 5 the multivariate W-M function has been used for the generation of the two symmetric rough walls and non-equilibrium molecular dynamics have been employed to study the temperature distribution across the nanochannel and to obtain the Kapitza length for different values of the wall-fluid interaction parameter $\varepsilon_{wf}$. Results indicate that the thermal conductance is higher for increased roughness amplitude. This is because of the combination of the restructure of the fluid in the vicinity of the walls when roughness is introduced and the increase of the wall-fluid contact area.

## 6.2 Results

First, we obtained the liquid density profiles by averaging over $10^4$ bins in the y-direction (Figure 6.1). As presented in chapter 4, organised layers of fluid particles are formed close to the nanochannel walls [44]. We can observe that as the roughness amplitude increases the fluid particles intrude the wall cavities and the mixing of layers phenomenon discussed in Chapter 4 becomes dominant. Moreover we can see that the increase of the wall-fluid interaction parameter leads to higher density peaks in the vicinity of the walls due to the increase of the adhesive force. However the main difference between the density profiles presented in Figure 6.1 and the ones illustrated in Figure 4.5 is asymmetry. We can observe that the density peaks on the left of each diagram which corresponds to the wall with the lower temperature ($90\,K$)

reach higher values than the ones on the right, a result which is in agreement with [36]. Moreover if we focus on the linear part of the density profiles at the centre of the nanochannel we can observe that there is a negative slope with an increasing absolute value for higher values of the wall-fluid interaction (Figure 6.2). As other researchers have pointed out, the density at the nanochannel centre is slightly reduced for higher values of the wall-fluid interaction parameter [43] due to the increased adhesive forces which attract the fluid atoms towards the nanochannel walls. We can make corresponding conclusions by observing the effect of increasing roughness amplitude on the density profiles at the nanochannel centre (Figure 6.3). Therefore we can say that the increase of both the roughness parameter and the wall-fluid interaction in combination with the temperature difference at the channel walls contribute to the asymmetry of the density profiles.

a)
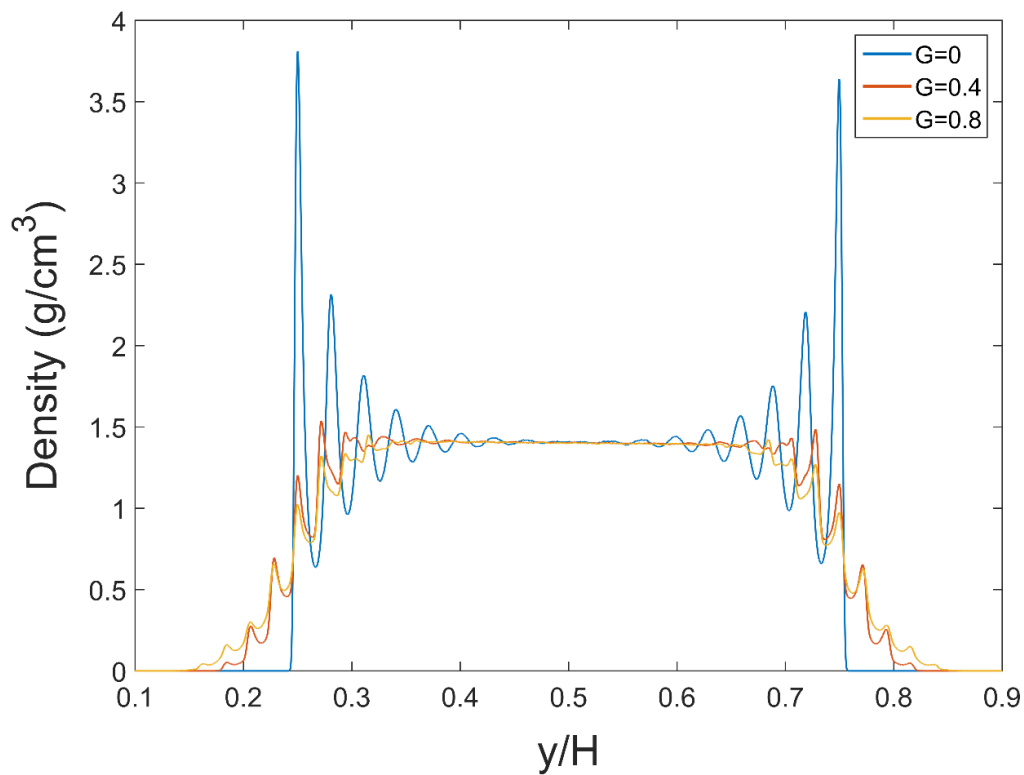
b)
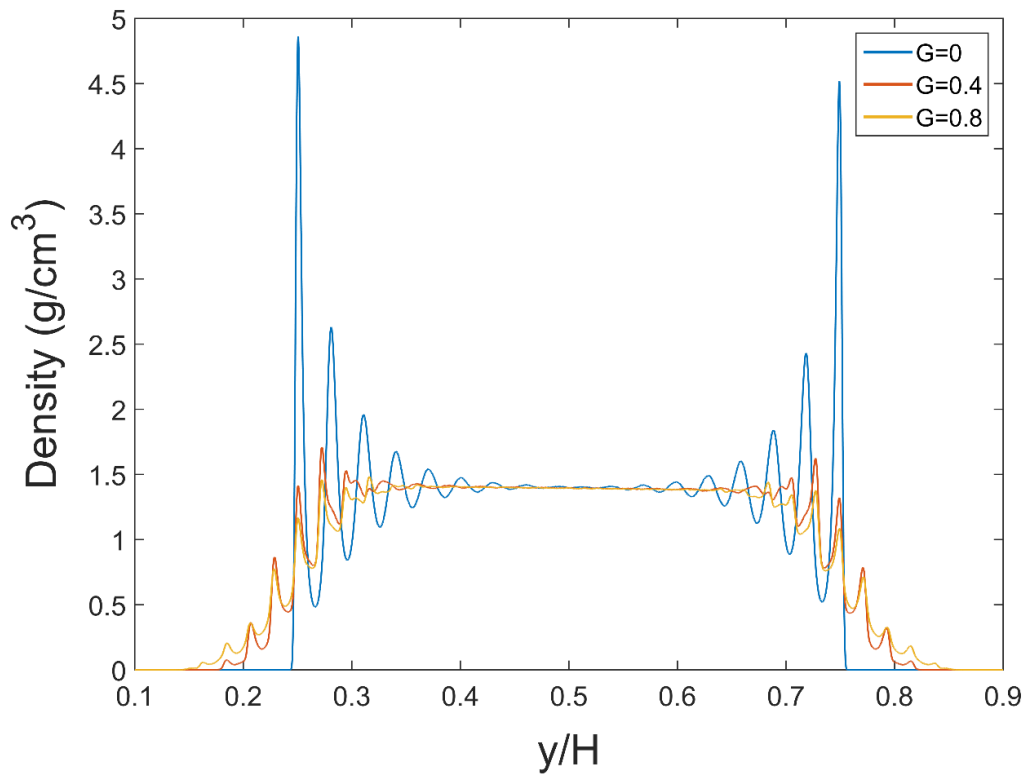


c)
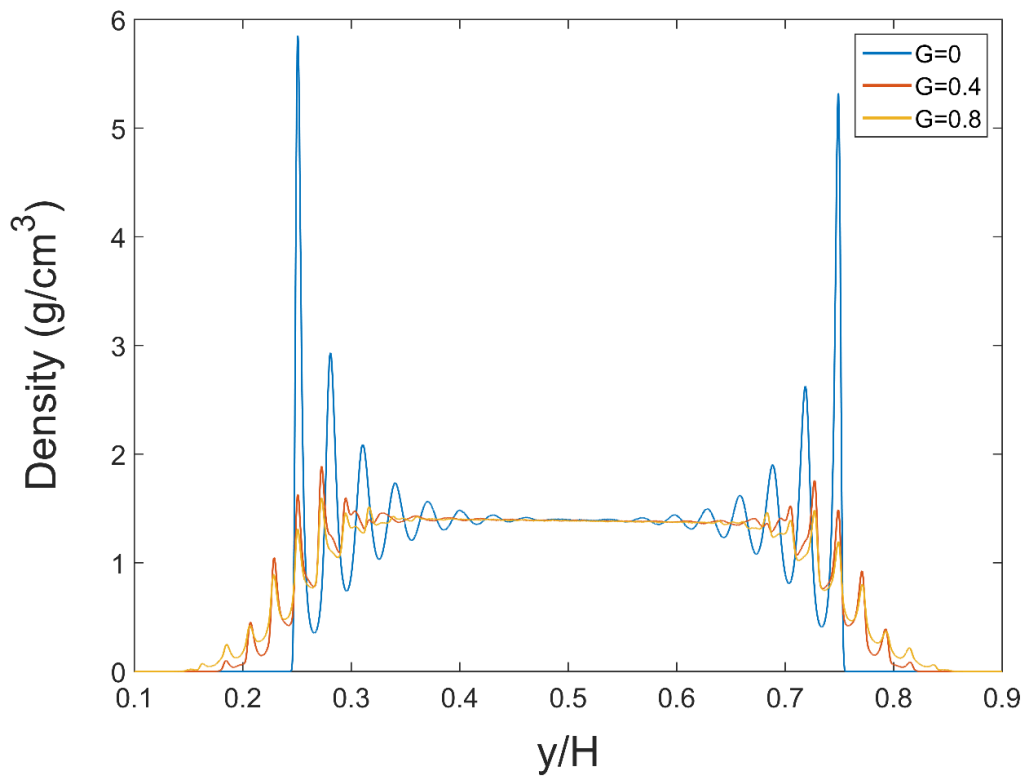


**Figure 6.1:** Density profiles vs. roughness parameter G for a) $\varepsilon_{wf} = 0.002$ eV b) $\varepsilon_{wf} = 0.004$ eV and c) $\varepsilon_{wf} = 0.006$ eV
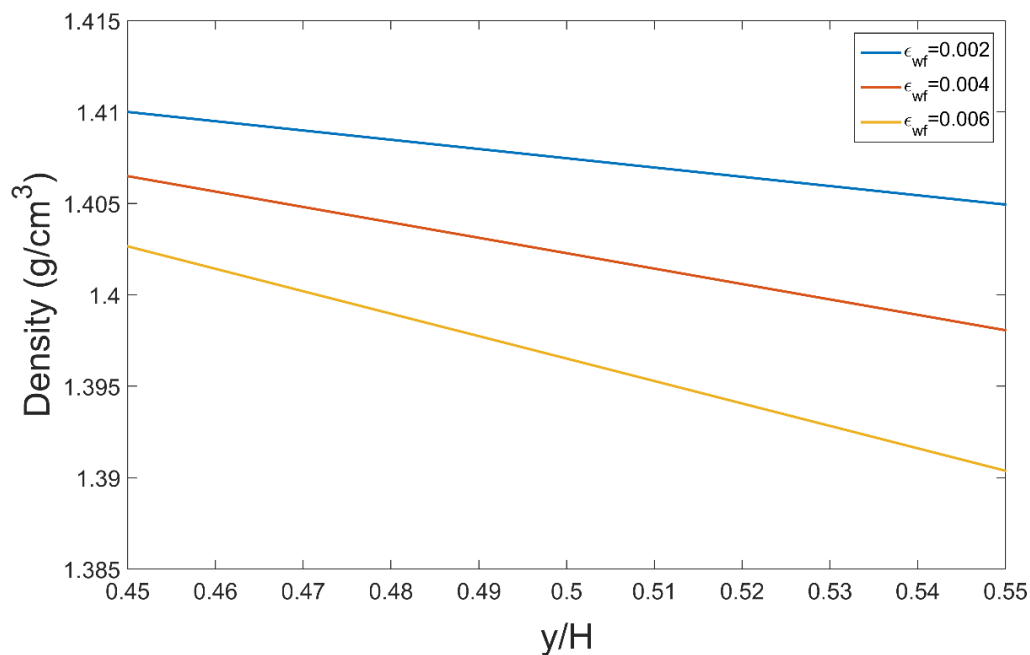
**Figure 6.2:** Extrapolated density profiles vs. wall-fluid interaction parameter at the centre of the nanochannel for G=0
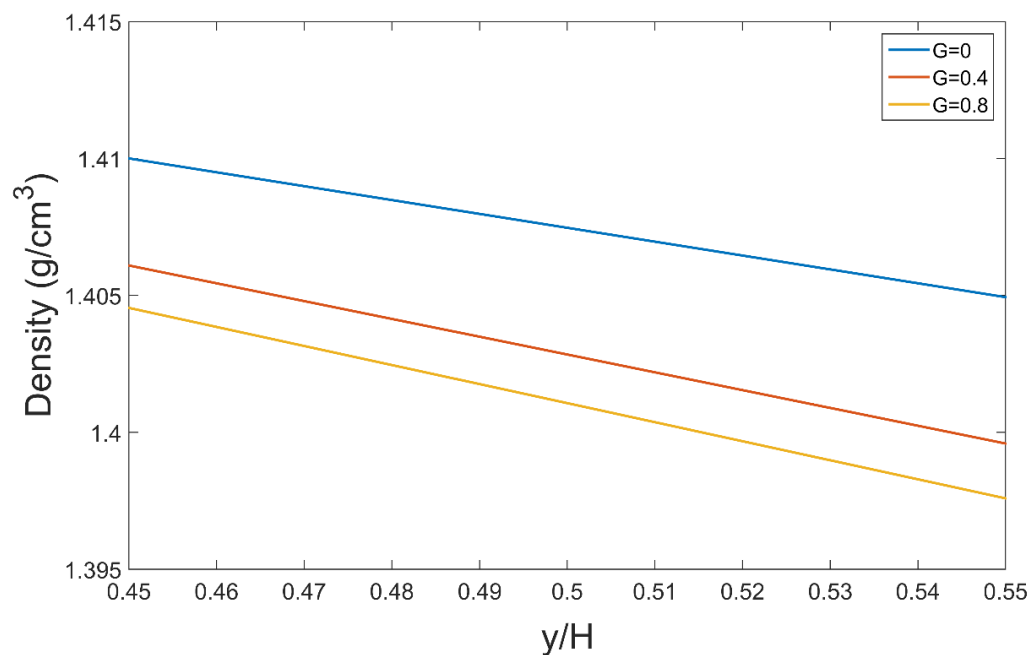


**Figure 6.3:** Extrapolated density profiles vs. roughness parameter G at the centre of the nanochannel for $\varepsilon_{wf} = 0.002$ eV

As mentioned in the introduction of this chapter, one of the factors that can affect the thermal conductance is the wall-fluid contact area. However the density profiles presented in Figure 6.1 do not provide any information on the contact area between the fluid and the solid atoms. For this reason we estimated the Radial Distribution Function (RDF) between the wall and the fluid atoms for each case according to Eq. A.21. The RDF profiles can be indicative of

**6.2** Results

the contact area as the more the fluid particles lying around the wall atoms the larger the contact area. The time averaged RDF profiles are plotted against the roughness parameter for different values of the wall-fluid interaction parameter (Figure 6.4).

a)



b)
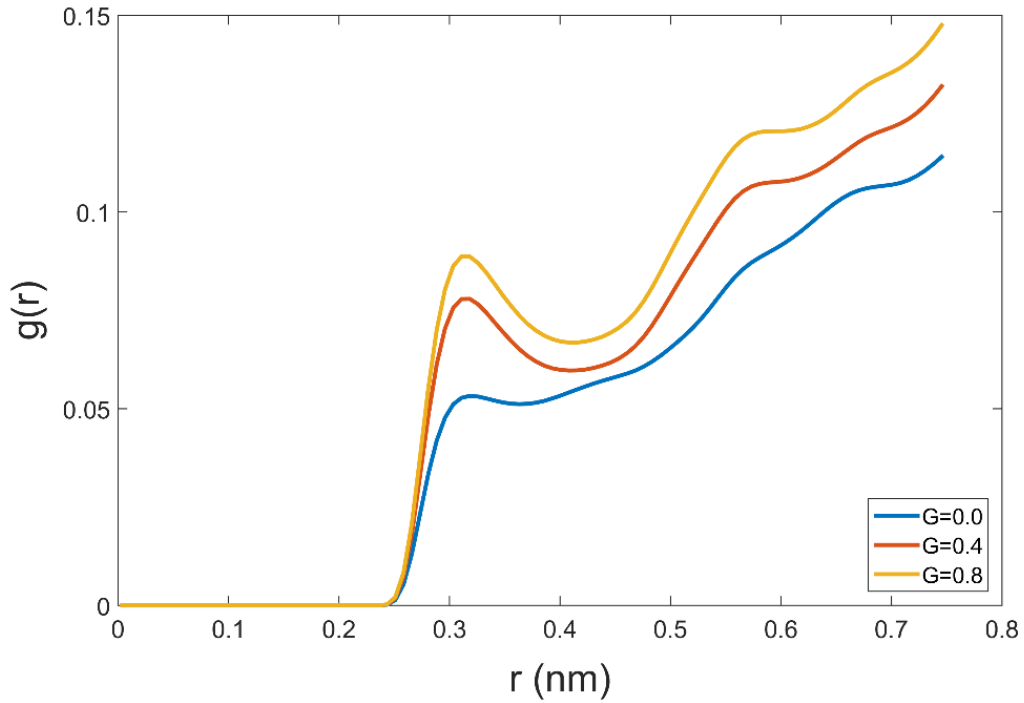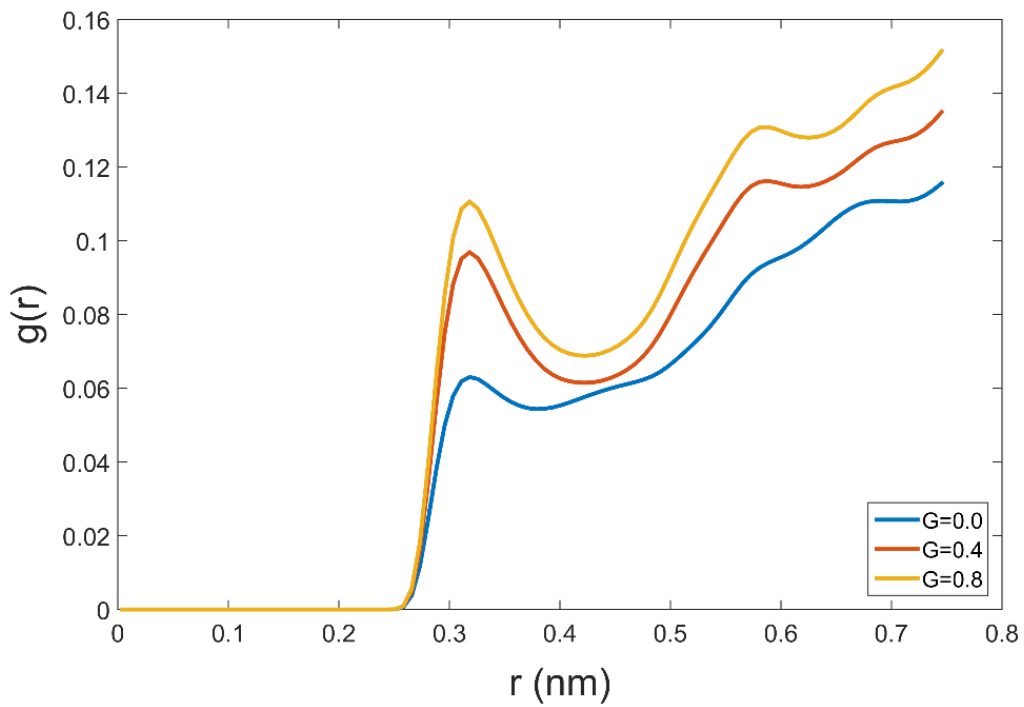
c)
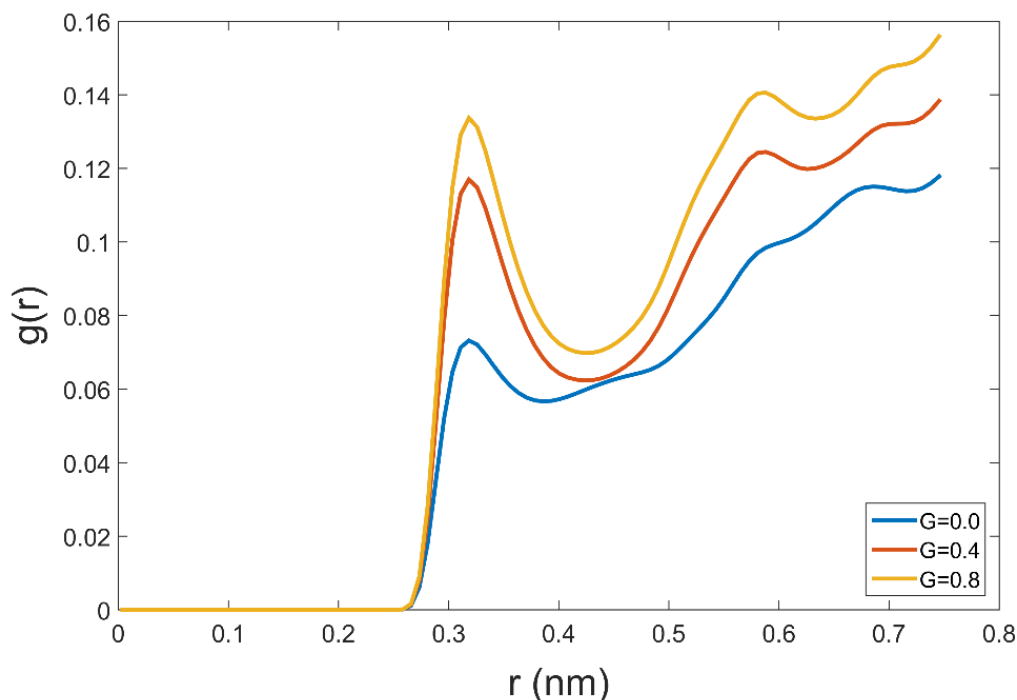


**Figure 6.4:** RDF profiles vs. roughness parameter G for a) $\varepsilon_{wf} = 0.002$ eV b) $\varepsilon_{wf} = 0.004$ eV and c) $\varepsilon_{wf} = 0.006$ eV

Figure 6.4 illustrates the dependence of the RDF on the roughness parameter and the wall-fluid interaction. We can observe that the RDF obtains higher values as the roughness parameter increases because of the increase of the contact area between the wall and the fluid. Moreover, for the same values of the roughness parameter $G$, $g(r)$ is higher as $\varepsilon_{wf}$ increases due to the increase of the adhesive forces. Based on these observations we should expect higher thermal conductance for increasing $G$ and $\varepsilon_{wf}$.

To obtain the temperature profiles across the nanochannel we divided the computational domain in 100 bins and the temperature was estimated according to Eq. 3.25. In Figure 6.5 temperature profiles are plotted against the roughness parameter $G$. The upper and lower limits of the x-axis correspond to the lower and upper wall centrelines respectively. We can observe that the temperature jump at both the lower and upper wall centrelines decreases as the roughness amplitude increases. This is because of the increase of the contact area between the fluid and the solid. Moreover, the temperature jump at both ends is reduced for higher values of $\varepsilon_{wf}$ for the same value of the roughness parameter. This result is consistent with the observations of Barisik and Beskok [72]. The asymmetry of the temperature profiles in Figure 6.5 is because of the asymmetric distribution of atoms across the nanochannel as illustrated in Figure 6.1.

## 6.2 Results

a)
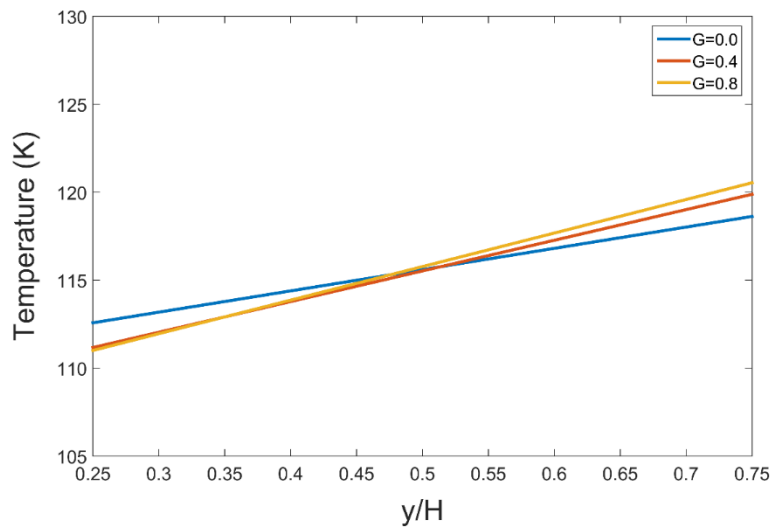


b)
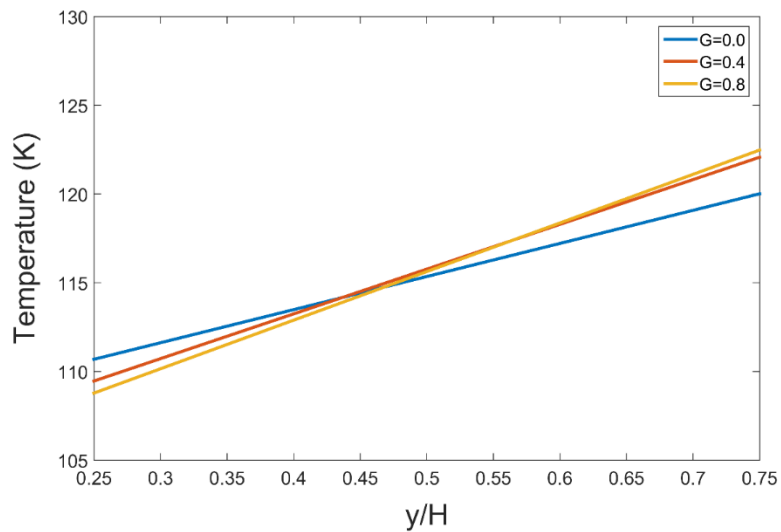


c)
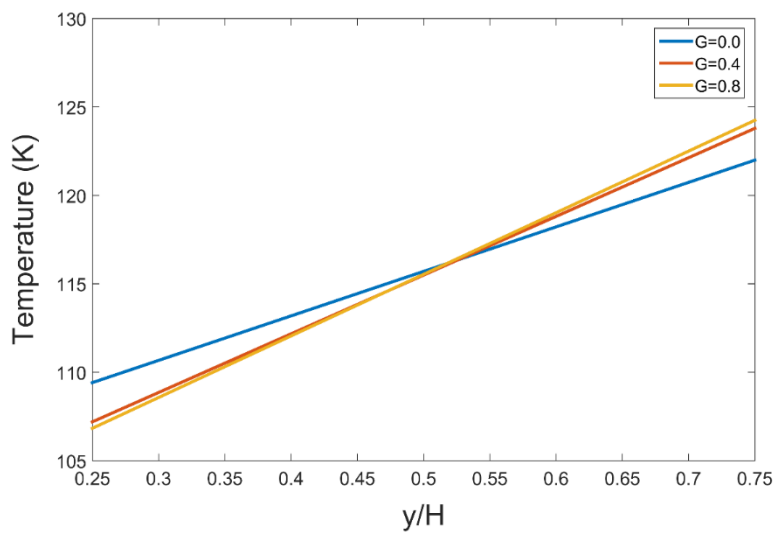


**Figure 6.5:** Temperature profiles vs. roughness parameter G for a) $\varepsilon_{wf} = 0.002$ eV b) $\varepsilon_{wf} = 0.004$ eV and c) $\varepsilon_{wf} = 0.006$ eV

## 6.2 Results

Finally, we evaluated the Kapitza length corresponding to the hot and cold wall surfaces according to Eq. 3.26. In Figure 6.6a & b the Kapitza length of the cold and hot interfaces respectively is plotted against the roughness parameter $G$ for the three different values of the wall-fluid interaction parameter. We can see that that both stronger wall-fluid interaction and increased roughness amplitude contribute towards the reduction of the Kapitza length which gradually approaches zero as the roughness amplitude increases. Moreover we can see that the Kapitza length values corresponding to identical wall-fluid interaction and roughness parameter are slightly larger for the cold surface which is consistent with [72]. Therefore we conclude that the wettability and the roughness parameter greatly affect the ITR in contrast to the surface temperature.

a)
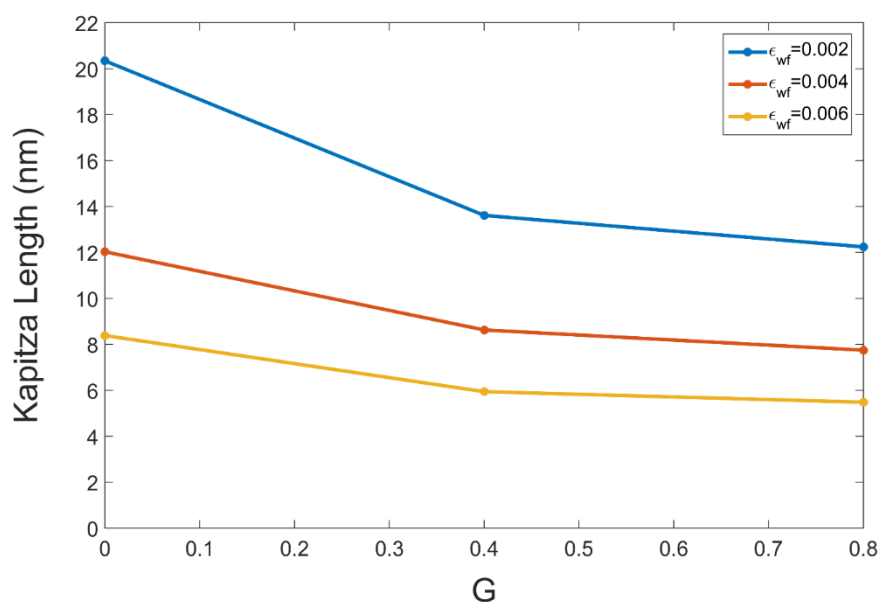


b)
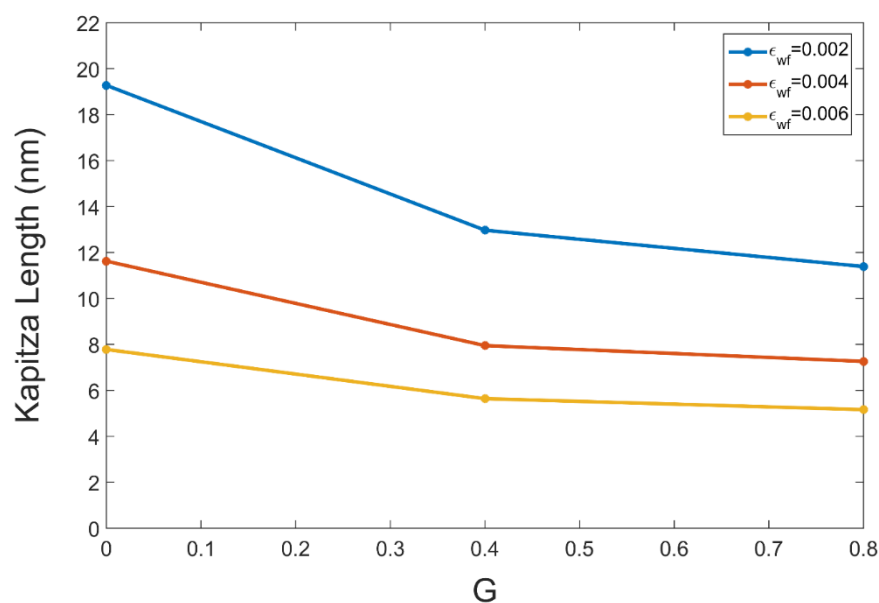


**Figure 6.6:** Kapitza Length vs. roughness parameter G and $\varepsilon_{wf}$ for a) the cold and b) the hot interface

# 6.3 Conclusions

In this chapter we performed non-equilibrium Molecular Dynamics simulations in order to study the thermal behaviour of confined liquids in rough nanochannels. We used the W-M function to generate the rough wall geometry. A temperature difference was induced by applying the Langevin thermostat on the four outermost layers of each wall resulting in a temperature gradient at the fluid region.

We first obtained the fluid density profiles across the nanochannel width which in this case are asymmetric despite the fact the nanochannel walls are perfectly symmetric between them. This asymmetry was attributed to the temperature gradient at the fluid region and resulted in the distribution of the fluid particles closer to the cold surface. Then, we estimated the RDF between the wall and fluid particles and noticed that its values were increased for higher roughness amplitude. Therefore it was safe to conclude that the interface contact area increases for rougher wall geometries. Moreover, the RDF profiles were increased for higher values of the wall-fluid interaction parameter. The temperature profiles drawn confirmed that roughness amplitude and wettability are two of the main parameters enhancing thermal conductance in nanochannels. Finally, we estimated the Kapitza length of the cold and hot interfaces respectively against the roughness parameter G for the different values of the wall-fluid interaction parameter. Results showed that the ITR is mainly affected by the roughness amplitude and the wettability in contrast to the surface temperature which is not a dominant factor.

# 7 Conclusions and Future Work

## 7.1 Conclusions

The recent and rapid development of micromachining has led to very accurate processing techniques which can be utilised for the fabrication of MicroElectroMechanical Systems (MEMS). MEMS are microscopic devices whose characteristic length ranges from 1 millimetre (mm) to 1 micrometre (μm). Nowadays, MEMS have a great variety of applications while some of the most popular ones are microchannel heat sinks and micropipes. It has been reported that the physical behaviour of fluids at such small length scales often deviates from the continuum behaviour as described by the Navier-Stokes equations. This is because in such small scales the properties depending on the volume of the system become less important and the surface effects become more dominant. It is therefore of great importance to utilise new methods for studying the physical behaviour of fluids in these scales.

A very efficient method successfully applied on nanoscale flows is Molecular Dynamics simulations which is based on the integration of the equations of motion of atoms interacting between them via forcefields or interatomic potentials. A significant number of forcefields has been developed over the last few years and Molecular Dynamics simulations have yielded accurate results for various physical problems ranging from material stress-strain analysis to nanochannel flows. In this PhD research we have implemented the Molecular Dynamics technique aiming to cover the existing knowledge gaps in the rheological and thermodynamic properties of monatomic fluids confined in nanochannels with rough walls described by the multivariate Weierstrass-Mandelbrot function. More specifically, we focused on the effect of the roughness amplitude on the fluid flow, viscosity and thermal conductance.

Generally, our nanochannels consisted of two solid walls made of atoms placed on the sites of a FCC lattice, using either springs or the EAM potential for this purpose. In order to generate walls with 3-dimensional rough geometry we first created a rectangular block of atoms and then deleted the atoms lying outside of the rough surface defined by the multivariate W-M function. In our simulations, we used a Lennard Jones fluid (liquid argon) and applied periodic boundary conditions in the directions being coplanar to the walls ($x$ and $z$). Since the wall geometry was complex, we used the dynamic Voronoi tessellation on the position of the liquid atoms to make an accurate estimation of the liquid volume. Depending on each simulation performed and the desired outcomes, we used different values of the wall-fluid interaction parameters, the temperature, the timestep and the roughness amplitude. For the integration of the Newton's equations of motion we used the LAMMPS Molecular Dynamics simulator.

Before presenting the results of our investigations we considered very important to provide the reader with a convincing and detailed validation and verification of the simulation methodology. In Paragraph 3.4 we validated our model taking the following criteria under consideration: a) the quality of the theory or model, b) the accuracy of the interatomic potential

or force field, c) the degree of sampling, statistics and convergence reached in the simulation, d) the quality of the simulation software and e) how competently the simulation software is used. Moreover, in the same paragraph, we verified our model and our results were found to be in a very good agreement with the results presented by other authors.

As far as the slip behaviour is considered, we found that roughness as well as wettability play a significant role in the pattern of the velocity profiles. Our results indicated that the maximum value of the velocity in a Poiseuille flow reduces for higher roughness amplitude and higher values of the wall-fluid interaction parameter. As a result there is a sudden decrease in the slip length when roughness is introduced to the model. The slip length then gradually reduces to a non-zero value for increasing roughness height. Moreover we found that in channels with higher wettability, the slip length drops faster as the depth of the roughness increases. We also compared the cases of 3-dimensional and 2-dimensional wall roughness profiles characterised by the same amplitude and wavelength and concluded that ignoring the wall irregularities in the spanwise direction can lead to an underestimation of the slip length. As far as the liquid structure is considered, we found that more oscillations appear in the 1-dimensional density profiles and the maximum density decreases as the roughness amplitude increases. However, we cannot consult the 1-dimensional density profiles to make safe conclusions for the liquid structure as detail is averaged out. This is because averaging in one dimension gives the illusion of parallel liquid layers of smaller density which does not reflect reality in the case of 3-dimensional roughness. Based on this observation we decided to draw 3-dimensional density profiles using isosurfaces to denote the surfaces with the same density. The most critical observation made in Chapter 4 is that pocket-like structures are formed in the vicinity of the walls when roughness is present in our model, replacing the well-defined density layers of the smooth wall case. Therefore we concluded that the mixing of layers phenomenon is induced by the irregular wall geometry leading to higher friction in the wall region and reduction of the slip length correspondingly. To our understanding the mixing of layers phenomenon is the key mechanism affecting the amount of interfacial slip.

In Chapter 5, stimulated by the alteration of the fluid structure in the vicinity of rough walls, we investigated the roughness amplitude effect on the fluid viscosity. We performed non-equilibrium Molecular Dynamics simulations and results showed that higher roughness amplitude results in the reduction of the diffusion coefficient in the region close to the nanochannel walls. This is consistent with the increased friction due to the mixing of layers phenomenon and can also be justified by the high trapping time of the fluid particles inside the wall cavities. In order to estimate the shear viscosity across the nanochannel we estimated the corresponding pressure and strain rate profiles. In the smooth wall case both of the aforementioned profiles were linear. However, for higher values of the roughness amplitude both the pressure and strain rate profiles became increasingly nonlinear in the vicinity of the walls as a sudden decrease, in terms of absolute value, appeared in this region. We attributed this behaviour to the obstacles imposed by the rough wall topography and to the weakening of the layered fluid structure, observed in the case of smooth walls, which is characterised by higher potential energy. As a result, shear viscosity appeared to be also increasingly nonlinear for higher values of the roughness amplitude. More specifically, we observed that the shear

viscosity obtains higher values in the vicinity of the walls and it gradually diminishes towards the nanochannel centre when the walls are rough. We also found that this behaviour is enhanced for higher values of the roughness amplitude while in the case of smooth walls the viscosity profile is linear. This observation agrees with the experimental investigations of Mala and Li [89]. We attributed this phenomenon to the alteration of the layered fluid structure in the vicinity of rough walls which triggers the mixing of layers phenomenon. In this way the movement of particles in this region is more obstructed compared to the case of smooth walls where parallel fluid layers are free to slide over each other.

In Chapter 6, we investigated the effect of the wall roughness height on the fluid thermal conductance. One interesting outcome was that the fluid density is not symmetric across the nanochannel when there is a temperature difference between the nanochannel walls. We observed that the density peaks in the vicinity of the cold wall reach higher values compared to the ones in the vicinity of the hot walls. Density profiles focusing on the centre of the nanochannel revealed that the absolute value of the slope becomes higher for increasing wettability and roughness parameter. The estimated temperature profiles showed that thermal conductance is enhanced with higher wall-fluid interaction parameters or roughness amplitude. This was attributed to the increase of the contact area and the restructure of the fluid particles in the vicinity of the walls. In order to prove this allegation we estimated the RDF profiles and as expected, we observed that $g(r)$ is shifted upwards (the fluid particles approach more closely the walls – the contact area increases) for higher values of the wall fluid interaction parameter and the roughness amplitude. In order to illustrate the dependence of the thermal resistance on wettability and the wall topography we estimated the Kapitza length as a function of the roughness amplitude for various values of the wall fluid interaction parameter. It was shown that the Kapitza length decreases for increasing roughness amplitude and increasing wall-fluid interaction parameter. Finally, it was shown that the interfacial thermal resistance is not greatly affected by the surface temperature.

# 7.2 Future Work

As it has been illustrated in the previous chapters, surface roughness is a parameter affecting a large number of properties in nanochannel flows. However, there are still some identified physical problems that need to be addressed:

- If and how the roughness amplitude can affect the thermal conductivity at the vicinity of the nanochannel walls.
- 3-dimensional profiles of the fluid properties should be obtained in the vicinity of the walls to enhance our understanding of the mechanisms of momentum and energy transport in this region.
- How the roughness amplitude might affect the phonon propagation at the wall-fluid interface.

Some topics for further investigation are proposed below:

- The determination of the W-M function parameters corresponding to manufacturing processes to develop more realistic computational models.

**7.2** Future Work

- The effect of other parameters contained in the W-M function such as the constant $\gamma$ on the fluid flow.
- The simulation of larger computational domains illustrating more realistically the fractal character of surfaces via mesoscale or multiscale models.
- The investigation of the nanochannel wall stress in correlation with roughness amplitude.
- The investigation of 3-dimensional roughness described by fractal geometry on polymer flows.

# Bibliography

[1]     C. Duan, W. Wang, and Q. Xie, "Review article: Fabrication of nanofluidic devices.," *Biomicrofluidics*, vol. 7, no. 2, p. 26501, 2013.

[2]     P. Abgrall and N. T. Nguyen, "Nanofluidic Devices and Their Applications," *Anal. Chem.*, vol. 80, no. 7, pp. 2326–2341, Apr. 2008.

[3]     G. E. Karniadakis, A. Beskok, and N. Aluru, *Microflows and Nanoflows: Fundamentals and Simulation*. Springer Science & Business Media, 2006.

[4]     J. Koplik, J. R. Banavar, and J. F. Willemsen, "Molecular dynamics of fluid flow at solid surfaces," *Phys. Fluids A Fluid Dyn.*, vol. 1, no. 5, p. 781, 1989.

[5]     M. Gad-El-Hak, "Gas and liquid transport at the microscale," *Heat Transf. Eng.*, vol. 27, no. 4, pp. 13–29, 2006.

[6]     K. P. Travis, B. D. Todd, and D. J. Evans, "Departure from Navier-Stokes hydrodynamics in confined liquids," *Phys. Rev. E*, vol. 55, no. 4, pp. 4288–4295, Apr. 1997.

[7]     D. Marx, J. Hutter, and Dominik Marx and Jurg Huutter, *Ab Initio Molecular Dynamics: Basic Theory and Advanced Methods*. Cambridge University Press, 2009.

[8]     K. Ohno, K. Esfarjani, and Y. Kawazoe, "Computational Materials Science - From Ab Initio to Monte Carlo | Kaoru Ohno | Springer," 2012. [Online]. Available: http://www.springer.com/us/book/9783540639619. [Accessed: 07-Oct-2015].

[9]     G. R. McNamara and G. Zanetti, "Use of the Boltzmann equation to simulate lattice-gas automata," *Phys. Rev. Lett.*, vol. 61, no. 20, p. 2332, 1988.

[10]    U. Frisch, B. Hasslacher, and Y. Pomeau, "Lattice-gas automata for the Navier-Stokes equation," *Phys. Rev. Lett.*, vol. 56, no. 14, p. 1505, 1986.

[11]    S. Chen and G. G. D. Doolen, "Lattice Boltzmann method for fluid flows," *Annu. Rev. Fluid Mech.*, vol. 30, no. 1, pp. 329–364, 1998.

[12]    X. Shan and H. Chen, "Lattice Boltzmann model for simulating flows with multiple phases and components," *Phys. Rev. E*, vol. 47, no. 3, p. 1815, 1993.

[13]    R. D. R. Groot and P. B. P. Warren, "Dissipative particle dynamics: Bridging the gap between atomistic and mesoscopic simulation," *J. Chem. Phys.*, vol. 107, no. 11, p. 4423, 1997.

[14]    P. J. Hoogerbrugge and J. Koelman, "Simulating microscopic hydrodynamic phenomena with dissipative particle dynamics," *EPL (Europhysics Lett.*, vol. 19, no. 3, p. 155, 1992.

[15]    A. L. Garcia, J. B. J. Bell, W. Y. W. Crutchfield, and B. B. J. Alder, "Adaptive mesh and algorithm refinement using direct simulation Monte Carlo," *J. Comput. Phys.*, vol. 154, no. 1, pp. 134–155, 1999.

[16]    E. S. Oran, C. K. Oh, and B. Z. Cybyk, "Direct simulation Monte Carlo: recent advances and applications 1," *Annu. Rev. Fluid Mech.*, vol. 30, no. 1, pp. 403–441, 1998.

[17]    S. T. O'Connell, P. P. A. Thompson, S. O'Connell, and P. P. A. Thompson, "Molecular dynamics–continuum hybrid computations: a tool for studying complex fluid flows," *Phys. Rev. E*, vol. 52, no. 6, p. R5792, 1995.

[18] M. Darbandi and E. Roohi, "Applying a hybrid DSMC/Navier–Stokes frame to explore the effect of splitter catalyst plates in micro/nanopropulsion systems," *Sensors actuators A Phys.*, vol. 189, pp. 409–419, 2013.

[19] K. Farber, P. Farber, J. Gräbel, S. Krick, J. Reitz, and P. Ueberholz, "Development and validation of a coupled Navier–Stokes/DSMC simulation for rarefied gas flow in the production process for OLEDs," *Appl. Math. ...*, 2015.

[20] I. I. G. Kevrekidis, C. W. Gear, J. M. Hyman, P. G. Kevrekidid, O. Runborg, and C. Theodoropoulos, "Equation-free, coarse-grained multiscale computation: Enabling mocroscopic simulators to perform system-level analysis," *Commun. ...*, vol. 1, no. 4, pp. 715–762, 2003.

[21] N. Asproulis, M. Kalweit, and D. Drikakis, "A hybrid molecular continuum method using point wise coupling," *Adv. Eng. Softw.*, vol. 46, no. 1, pp. 85–92, 2012.

[22] S. Yasuda and R. Yamamoto, "A model for hybrid simulations of molecular dynamics and computational fluid dynamics," *Phys. Fluids*, vol. 20, no. 11, p. 113101, 2008.

[23] J. Archard, "Elastic deformation and the laws of friction," *Proc. R. Soc. ...*, 1957.

[24] J. A. Greenwood and J. J. Wu, "Surface Roughness and Contact: An Apology," *Meccanica*, vol. 36, no. 6, pp. 617–630.

[25] B. Alder and T. Wainwright, "Studies in molecular dynamics. I. General method," *J. Chem. Phys.*, 1959.

[26] D. Y. C. Chan and R. G. Horn, "The drainage of thin liquid films between solid surfaces," *J. Chem. Phys.*, vol. 83, no. 10, p. 5311, 1985.

[27] I. K. Snook and W. van Megen, "Solvation forces in simple dense fluids. I," *J. Chem. Phys.*, vol. 72, no. 5, p. 2907, 1980.

[28] S. A. Somers and H. T. Davis, "Microscopic dynamics of fluids confined between smooth and atomically structured solid surfaces," *J. Chem. Phys.*, vol. 96, no. 7, p. 5389, 1992.

[29] U. Heinbuch and J. Fischer, "Liquid flow in pores: Slip, no-slip, or multilayer sticking," *Phys. Rev. A*, vol. 40, no. 2, pp. 1144–1146, Jul. 1989.

[30] P. A. Thompson and M. O. Robbins, "Shear flow near solids: Epitaxial order and flow boundary conditions," *Phys. Rev. A*, vol. 41, no. 12, pp. 6830–6837, Jun. 1990.

[31] R. Qiao and N. R. Aluru, "Ion concentrations and velocity profiles in nanochannel electroosmotic flows," *J. Chem. Phys.*, vol. 118, no. 10, p. 4692, 2003.

[32] M. Wang, J. Liu, and S. Chen, "Electric potential distribution in nanoscale electroosmosis: from molecules to continuum," *Mol. Simul.*, 2008.

[33] C. Y. Soong, T. H. Yen, and P. Y. Tzeng, "Molecular dynamics simulation of nanochannel flows with effects of wall lattice-fluid interactions," *Phys. Rev. E*, vol. 76, no. 3, p. 36303, Sep. 2007.

[34] A. E. Giannakopoulos, F. Sofos, T. E. Karakasidis, and A. Liakopoulos, "Unified description of size effects of transport properties of liquids flowing in nanochannels," *Int. J. Heat Mass Transf.*, vol. 55, no. 19, pp. 5087–5092, 2012.

[35] C. Sun, W.-Q. Lu, B. Bai, and J. Liu, "Anomalous enhancement in thermal conductivity of nanofluid induced by solid walls in a nanochannel," *Appl. Therm. Eng.*, vol. 31, no.

17, pp. 3799–3805, 2011.

[36]  Z. Shi, M. Barisik, and A. Beskok, "Molecular dynamics modeling of thermal resistance at argon-graphite and argon-silver interfaces," *Int. J. Therm. Sci.*, vol. 59, pp. 29–37, 2012.

[37]  V. P. Sokhan, D. Nicholson, and N. Quirke, "Fluid flow in nanopores: An examination of hydrodynamic boundary conditions," *J. Chem. Phys.*, vol. 115, no. 8, p. 3878, 2001.

[38]  N. Asproulis and D. Drikakis, "Boundary slip dependency on surface stiffness," *Phys. Rev. E*, vol. 81, no. 6, pp. 1–5, 2010.

[39]  K. P. K. Travis and K. E. Gubbins, "Poiseuille flow of Lennard-Jones fluids in narrow slit pores," *J. Chem. Phys.*, vol. 112, no. 4, p. 1984, 2000.

[40]  J. Koplik, J. R. Banavar, and J. F. Willemsen, "Molecular dynamics of Poiseuille flow and moving contact lines," *Phys. Rev. Lett.*, vol. 60, no. 13, pp. 1282–1285, Mar. 1988.

[41]  D. J. Evans and G. P. Morriss, "Nonequilibrium Molecular-Dynamics Simulation of Couette Flow in Two-Dimensional Fluids," *Phys. Rev. Lett.*, vol. 51, no. 19, pp. 1776–1779, Nov. 1983.

[42]  G. Nagayama and P. Cheng, "Effects of interface wettability on microscale flow by molecular dynamics simulation," *Int. J. Heat Mass Transf.*, 2004.

[43]  N. Asproulis and D. Drikakis, "Surface roughness effects in micro and nanofluidic devices," *J. Comput. Theor. Nanosci.*, vol. 7, no. 9, pp. 1825–1830, 2010.

[44]  N. Priezjev, A. Darhuber, and S. Troian, "Slip behavior in liquid films on surfaces of patterned wettability: Comparison between continuum and molecular dynamics simulations," *Phys. Rev. E*, 2005.

[45]  P. Thompson and S. Troian, "A general boundary condition for liquid flow at solid surfaces," *Nature*, 1997.

[46]  N. Asproulis and D. Drikakis, "Wall-mass effects on hydrodynamic boundary slip," *Phys. Rev. E*, vol. 84, no. 3, pp. 1–6, 2011.

[47]  R. Voronov and D. Papavassiliou, "Boundary slip and wetting properties of interfaces: correlation of the contact angle with the slip length," *J. Chem.*, 2006.

[48]  N. Priezjev and S. Troian, "Molecular origin and dynamic behavior of slip in sheared polymer films," *Phys. Rev. Lett.*, 2004.

[49]  M. P. Allen and D. J. Tildesley, *Computer Simulation of Liquids*. Clarendon Press, 1989.

[50]  D. Levesque, L. Verlet, and J. Kürkijarvi, "Computer &quot;Experiments&quot; on Classical Fluids. IV. Transport Properties and Time-Correlation Functions of the Lennard-Jones Liquid near Its Triple Point," *Phys. Rev. A*, vol. 7, no. 5, pp. 1690–1700, May 1973.

[51]  E. Gosling, I. McDonald, and K. Singer, "On the calculation by molecular dynamics of the shear viscosity of a simple fluid," *Mol. Phys.*, 1973.

[52]  A. W. Lees, S. F. Edwards, G. D. M. and W. T. E. Alder B J, H. E, L. A. W, and V. L, "The computer study of transport processes under extreme conditions," *J. Phys. C Solid State Phys.*, vol. 5, no. 15, pp. 1921–1928, Aug. 1972.

[53]  W. T. Ashurst and W. G. Hoover, "Argon Shear Viscosity via a Lennard-Jones Potential

with Equilibrium and Nonequilibrium Molecular Dynamics," *Phys. Rev. Lett.*, vol. 31, no. 4, pp. 206–208, Jul. 1973.

[54]  W. Ashurst and W. Hoover, "Dense-fluid shear viscosity via nonequilibrium molecular dynamics," *Phys. Rev. A*, 1975.

[55]  G. Morriss and D. Evans, *Statistical Mechanics of Nonequilbrium Liquids*. 2007.

[56]  B. Todd and D. Evans, "Temperature profile for Poiseuille flow," *Phys. Rev. E*, 1997.

[57]  I. Bitsanis, J. J. Magda, M. Tirrell, and H. T. Davis, "Molecular dynamics of flow in micropores," *J. Chem. Phys.*, vol. 87, no. 3, p. 1733, 1987.

[58]  C. S. S. R. Kumar, *Microfluidic Devices in Nanotechnology: Applications*, vol. 29. John Wiley & Sons, 2010.

[59]  F. Müller-Plathe, "Reversing the perturbation in nonequilibrium molecular dynamics: An easy way to calculate the shear viscosity of fluids," *Phys. Rev. E*, 1999.

[60]  P. Bordat, F. Mü Ller-Plathe, and F. Müller-Plathe, "The shear viscosity of molecular fluids : A calculation by reverse nonequilibrium molecular dynamics," *J. Chem. Phys.*, 2002.

[61]  M. Zhang, E. Lussetti, and L. de Souza, "Thermal conductivities of molecular liquids by reverse nonequilibrium molecular dynamics," *J.*, 2005.

[62]  P. Kapitza, "Heat transfer and superfluidity of helium II," *Phys. Rev.*, 1941.

[63]  E. Swartz and R. Pohl, "Thermal boundary resistance," *Rev. Mod. Phys.*, 1989.

[64]  A. Maiti, G. D. Mahan, and S. T. Pantelides, "Dynamical simulations of nonequilibrium processes — Heat flow and the Kapitza resistance across grain boundaries," *Solid State Commun.*, vol. 102, no. 7, pp. 517–521, 1997.

[65]  J. Barrat and F. Chiaruttini, "Kapitza resistance at the liquid—solid interface," *Mol. Phys.*, 2003.

[66]  L. Xue, P. Keblinski, S. Phillpot, and S. Choi, "Two regimes of thermal resistance at a liquid–solid interface," *J. ...*, 2003.

[67]  B. Kim, A. Beskok, and T. Cagin, "Thermal interactions in nanoscale fluid flow: molecular dynamics simulations with solid–liquid interfaces," *Microfluid. Nanofluidics*, 2008.

[68]  C. Liu, H. Fan, K. Zhang, and M. Yuen, "Flow dependence of interfacial thermal resistance in nanochannels," *J. Chem.*, 2010.

[69]  G. Balasubramanian and S. Banerjee, "Unsteady nanoscale thermal transport across a solid-fluid interface," *J. Appl. Phys.*, 2008.

[70]  S. Murad and I. Puri, "Thermal transport across nanoscale solid-fluid interfaces," 2008.

[71]  M. Barisik and A. Beskok, "Boundary treatment effects on molecular dynamics simulations of interface thermal resistance," *J. Comput. Phys.*, 2012.

[72]  M. Barisik and A. Beskok, "Temperature dependence of thermal resistance at the water/silicon interface," *Int. J. Therm. Sci.*, 2014.

[73]  H. Berendsen and J. Grigera, "The missing term in effective pair potentials," *J. Phys.*, 1987.

[74] Z. Ge, D. Cahill, and P. Braun, "Thermal conductance of hydrophilic and hydrophobic interfaces," *Phys. Rev. Lett.*, 2006.

[75] J. Nikuradse, *Laws of flow in rough pipes*. 1950.

[76] S. Richardson, "On the no-slip boundary condition," *J. Fluid Mech.*, 1973.

[77] S. G. KANDLIKAR, "Roughness effects at microscale - Reassessing Nikuradse's experiments on liquid flow in rough tubes," *Bull. Polish Acad. Sci. Tech. Sci.*, vol. 53, no. 4, Dec. 2005.

[78] J. Gao, W. Luedtke, and U. Landman, "Structures, solvation forces and shear of molecular films in a rough nano-confinement," *Tribol. Lett.*, 2000.

[79] A. Jabbarzadeh, J. Atkinson, and R. Tanner, "Effect of the wall roughness on slip and rheological properties of hexadecane in molecular dynamics simulation of Couette shear flow between two sinusoidal walls," *Phys. Rev. E*, 2000.

[80] T. Galea and P. Attard, "Molecular dynamics study of the effect of atomic roughness on the slip length at the fluid-solid boundary during shear flow," *Langmuir*, 2004.

[81] Y. Chen, C. Zhang, M. Shi, and G. G. P. Peterson, "Slip boundary for fluid flow at rough solid surfaces," *Appl. Phys. Lett.*, vol. 100, no. 7, p. 74102, 2012.

[82] A. Majumdar and C. Tien, "Fractal characterization and simulation of rough surfaces," *Wear*, 1990.

[83] F. Sofos, T. Karakasidis, and A. Liakopoulos, "Effects of wall roughness on flow in nanochannels," *Phys. Rev. E*, 2009.

[84] N. V. N. Priezjev and S. S. M. Troian, "Influence of periodic wall roughness on the slip behaviour at liquid/solid interfaces: molecular-scale simulations versus continuum predictions," *J. Fluid Mech.*, vol. 554, pp. 25–46, 2006.

[85] A. Niavarani and N. V. N. Priezjev, "Rheological study of polymer flow past rough surfaces with slip boundary conditions," *J. Chem. Phys.*, vol. 129, no. 14, p. 144902, 2008.

[86] K. Kremer and G. Grest, "Dynamics of entangled linear polymer melts: A molecular-dynamics simulation," *J. Chem. Phys.*, 1990.

[87] B. B.-Y. Cao, M. Chen, and Z. Z.-Y. Guo, "Effect of surface roughness on gas flow in microchannels by molecular dynamics simulation," *Int. J. Eng. Sci.*, vol. 44, no. 13, pp. 927–937, 2006.

[88] C. Zhang and Y. Chen, "Slip behavior of liquid flow in rough nanochannels," *Chem. Eng. Process. Process Intensif.*, vol. 85, pp. 203–208, 2014.

[89] G. Mala and D. Li, "Flow characteristics of water in microtubes," *Int. J. heat fluid flow*, 1999.

[90] F. Sofos, T. E. Karakasidis, and A. Liakopoulos, "Effect of wall roughness on shear viscosity and diffusion in nanochannels," *Int. J. Heat Mass Transf.*, vol. 53, no. 19–20, pp. 3839–3846, Sep. 2010.

[91] K. K. L. Yung, L. He, Y. Xu, and Y. Y. W. Shen, "Study of surface conditions and shear flow of LCP melts in nanochannels through molecular dynamics simulation," *Polymer (Guildf).*, vol. 47, 2006.

[92]   M. Shibahara and K. Takeuchi, "A Molecular Dynamics Study on the Effects of Nanostructural Clearances on Thermal Resistance at a Liquid Water–Solid Interface," *Nanoscale and Microscale*, 2008.

[93]   H. Acharya, N. N. J. Mozdzierz, P. Keblinski, and S. Garde, "How chemistry, nanoscale roughness, and the direction of heat flow affect thermal conductance of solid–water interfaces," *Ind. ...*, vol. 51, no. 4, pp. 1767–1773, Feb. 2011.

[94]   Y. Chen and C. Zhang, "Role of surface roughness on thermal conductance at liquid–solid interfaces," *Int. J. Heat Mass Transf.*, 2014.

[95]   Y. Chen, C. Zhang, M. Shi, and G. Peterson, "Role of surface roughness characterized by fractal geometry on laminar flow in microchannels," *Phys. Rev. E*, 2009.

[96]   D. Rapaport, *The art of molecular dynamics simulation*. 2004.

[97]   K. Binder, *Monte Carlo and molecular dynamics simulations in polymer science*. 1995.

[98]   W. A. Steele, *The interaction of gases with solid surfaces*. Pergamon Press, 1974.

[99]   F. Mourits and F. Rummens, "A critical evaluation of Lennard-Jones and Stockmayer potential parameters and of some correlation methods," *Can. J. Chem.*, 1977.

[100] M. Daw and M. Baskes, "Embedded-atom method: Derivation and application to impurities, surfaces, and other defects in metals," *Phys. Rev. B*, 1984.

[101] L. Zhou and H. Huang, "Are surfaces elastically softer or stiffer?," *Appl. Phys. Lett.*, 2004.

[102] J. Angelo and M. Baskes, "Interfacial studies using the EAM and MEAM," *Interface Sci.*, vol. 4, no. 1–2, 1997.

[103] J. W. Gibbs, *Elementary Principles in Statistical Mechanics*. Courier Corporation, 2014.

[104] S. Park and F. Khalili-Araghi, "Free energy calculation from steered molecular dynamics simulations using Jarzynski's equality," *J. Chem. ...*, 2003.

[105] Y. Li, J. Xu, and D. Li, "Molecular dynamics simulation of nanoscale liquid flows," *Microfluid. Nanofluidics*, 2010.

[106] B. Alder, D. Gass, and T. Wainwright, "Studies in Molecular Dynamics. VIII. The Transport Coefficients for a Hard-Sphere Fluid," *J. Chem. ...*, 1970.

[107] H. Rafii-Tabar, H. M. Shodja, M. Darabi, and A. Dahi, "Molecular dynamics simulation of crack propagation in fcc materials containing clusters of impurities," *Mech. Mater.*, vol. 38, no. 3, pp. 243–252, Mar. 2006.

[108] V. Yamakov, D. Wolf, and S. Phillpot, "Deformation-mechanism map for nanocrystalline metals by molecular-dynamics simulation," *Nat. Mater.*, 2004.

[109] Q.-K. Li and M. Li, "Molecular dynamics simulation of intrinsic and extrinsic mechanical properties of amorphous metals," *Intermetallics*, vol. 14, no. 8–9, pp. 1005–1010, Aug. 2006.

[110] H. Van Swygenhoven, A. Caro, and D. Farkas, "A molecular dynamics study of polycrystalline fcc metals at the nanoscale: grain boundary structure and its influence on plastic deformation," *Mater. Sci. ...*, 2001.

[111] V. Varshney, S. Patnaik, A. Roy, and B. Farmer, "A molecular dynamics study of epoxy-

based networks: cross-linking procedure and prediction of molecular and material properties," *Macromolecules*, 2008.

[112] C. Bennemann, W. Paul, K. Binder, and B. Dünweg, "Molecular-dynamics simulations of the thermal glass transition in polymer melts: α-relaxation behavior," *Phys. Rev. E*, vol. 57, no. 1, pp. 843–851, Jan. 1998.

[113] D. Frenkel and B. Smit, *Understanding Molecular Simulation: From Algorithms to Applications*. Academic Press, 2001.

[114] K. Eom, *Simulations in nanobiotechnology*. 2011.

[115] L. Verlet, "Computer' experiments' on classical fluids. I. Thermodynamical properties of Lennard-Jones molecules," *Phys. Rev.*, 1967.

[116] B. B. Mandelbrot and a. Blumen, "Fractal Geometry: What is it, and What Does it do? [and Discussion]," *Proc. R. Soc. A Math. Phys. Eng. Sci.*, vol. 423, no. 1864, pp. 3–16, 1989.

[117] A. Majumdar and B. Bhushan, "Fractal model of elastic-plastic contact between rough surfaces," *J. Tribol.*, 1991.

[118] M. Berry and Z. Lewis, "On the Weierstrass-Mandelbrot fractal function," *... R. Soc. London ...*, 1980.

[119] M. Ausloos and D. H. Berman, "A multivariate Weierstrass-Mandelbrot function," *Proc. R. Soc. London.A.Mathematical Phys. Sci.*, vol. 400, no. 1819, pp. 331–350, 1985.

[120] M. Ciavarella, J. Greenwood, and M. Paggi, "Inclusion of 'interaction' in the Greenwood and Williamson contact theory," *Wear*, 2008.

[121] K. Komvopoulos, "Effects of multi-scale roughness and frictional heating on solid body contact deformation," *Comptes Rendus Mécanique*, 2008.

[122] B. Chatterjee and P. Sahoo, "Finite Element Based Contact Analysis of Fractal Surfaces – Effect of Varying Elastic Modulus," *Procedia Eng.*, vol. 90, pp. 116–122, 2014.

[123] S. Bernardi, B. D. Todd, and D. J. Searles, "Thermostating highly confined fluids," *J. Chem. Phys.*, vol. 132, no. 24, p. 244706, 2010.

[124] K. Binder, J. Horbach, W. Kob, W. Paul, and F. Varnik, "Molecular dynamics simulations," *J. Phys. Condens. Matter*, vol. 16, no. 5, p. S429, 2004.

[125] S. Plimpton, "Fast parallel algorithms for short-range molecular dynamics," *J. Comput. Phys.*, vol. 117, no. 1, pp. 1–19, 1995.

[126] W. F. van Gunsteren and A. E. Mark, "Validation of molecular dynamics simulation," *J. Chem. Phys.*, vol. 108, no. 15, p. 6109, 1998.

[127] S. Yip, *Handbook of materials modeling*. 2007.

[128] D. M. Heyes, "Self-diffusion and shear viscosity of simple fluids. A molecular-dynamics study," *J. Chem. Soc. Faraday Trans. 2*, vol. 79, no. 12, p. 1741, 1983.

[129] J. Laurent, A. Drezet, H. Sellier, J. Chevrier, and S. Huant, "Large variation in the boundary-condition slippage for a rarefied gas flowing between two surfaces," *Phys. Rev. Lett.*, 2011.

[130] C.-H. Choi, K. J. A. Westin, and K. K. S. K. Breuer, "Apparent slip flows in hydrophilic

and hydrophobic microchannels," *Phys. Fluids*, vol. 15, no. 10, pp. 2897–2902, 2003.

[131] D. D. C. Tretheway and C. D. C. Meinhart, "Apparent fluid slip at hydrophobic microchannel walls," *Phys. Fluids*, vol. 14, no. 3, pp. L9–L12, 2002.

[132] R. S. R. Voronov, D. V. D. Papavassiliou, and L. L. Lee, "Slip length and contact angle over hydrophobic surfaces," *Chem. Phys. Lett.*, vol. 441, no. 4, pp. 273–276, 2007.

[133] N. V Priezjev, "Effect of surface roughness on rate-dependent slip in simple fluids," *J. Chem. Phys.*, vol. 127, no. 14, p. 144708, 2007.

[134] D. Kim and E. Darve, "Molecular dynamics simulation of electro-osmotic flows in rough wall nanochannels," *Phys. Rev. E*, 2006.

[135] W. Qu, G. M. Mala, and D. Li, "Heat transfer for water flow in trapezoidal silicon microchannels," *Int. J. Heat Mass Transf.*, vol. 43, no. 21, pp. 3925–3936, Nov. 2000.

[136] D. G. Cahill, W. K. Ford, K. E. Goodson, G. D. Mahan, A. Majumdar, H. J. Maris, R. Merlin, and S. R. Phillpot, "Nanoscale thermal transport," *J. Appl. Phys.*, vol. 93, no. 2, p. 793, Dec. 2003.

[137] B. Kim, A. Beskok, and T. Cagin, "Molecular dynamics simulations of thermal resistance at the liquid-solid interface," *J. Chem. Phys.*, 2008.

[138] S. Maruyama and T. Kimura, "A study on thermal resistance over a solid-liquid interface by the molecular dynamics method," *Therm. Sci. Eng*, 1999.

[139] N. M. Ghoniem†, E. P. Busso, N. Kioussis, and H. Huang, "Multiscale modelling of nanomechanics and micromechanics: an overview," *Philos. Mag.*, vol. 83, no. 31–34, pp. 3475–3528, 2003.

[140] *Elements of Metallurgy and Engineering Alloys*. ASM International, 2008.

[141] W. Conover, "Chemistry, 8th Edition (by Stephen S. Zumdahl and Susan A. Zumdahl)," *J. Chem. Educ.*, vol. 86, no. 11, p. 1273, Nov. 2009.

[142] B. Brooks and R. Bruccoleri, "CHARMM: A program for macromolecular energy, minimization, and dynamics calculations," *J. ...*, 1983.

[143] S. Mayo, B. Olafson, and W. Goddard, "DREIDING: a generic force field for molecular simulations," *J. Phys. ...*, 1990.

[144] J. Wang and R. Wolf, "Development and testing of a general amber force field," *J. ...*, 2004.

[145] A. Rappé and C. Casewit, "UFF, a full periodic table force field for molecular mechanics and molecular dynamics simulations," *J. ...*, 1992.

[146] D. Brenner, "Empirical potential for hydrocarbons for use in simulating the chemical vapor deposition of diamond films," *Phys. Rev. B*, 1990.

[147] D. Root, C. Landis, and T. Cleveland, "Valence bond concepts applied to the molecular mechanics description of molecular shapes. 1. Application to nonhypervalent molecules of the P-block," *J. Am. ...*, 1993.

[148] A. C. T. Van Duin, S. Dasgupta, F. Lorant, W. A. Goddard, A. Van Duin, and S. Dasgupta, "ReaxFF: a reactive force field for hydrocarbons," *J. ...*, vol. 105, no. 41, pp. 9396–9409, 2001.

[149] A. Rappe and W. G. III, "Charge equilibration for molecular dynamics simulations," *J. Phys. Chem.*, 1991.

[150] A. van Duin, "Delft molecular mechanics: a new approach to hydrocarbon force fields. Inclusion of a geometry-dependent charge calculation," *J. Chem. ...*, 1994.

[151] A. Greenfield, J. Wellendorf, and N. Wiser, "X-ray determination of the static structure factor of liquid Na and K," *Phys. Rev. A*, 1971.

[152] E. Allahyarov, P. Schram, and S. Trigger, "Low-angle structure factor behavior of expanded liquid metals," *Phys. B Condens. Matter*, 1995.

[153] R. Vacher, T. Woignier, J. Pelous, and E. Courtens, "Structure and self-similarity of silica aerogels," *Phys. Rev. B*, 1988.

[154] D. Chandler, "Introduction to modern statistical mechanics," *Introd. to Mod. Stat. Mech. by ...*, 1987.

[155] J. Dong, O. Sankey, and C. Myles, "Theoretical study of the lattice thermal conductivity in Ge framework semiconductors," *Phys. Rev. Lett.*, 2001.

[156] P. Cummings and D. Evans, "Nonequilibrium molecular dynamics approaches to transport properties and non-Newtonian fluid rheology," *Ind. Eng. Chem. ...*, 1992.

[157] R. J. Sadus, *Molecular Simulation of Fluids*. Elsevier, 2002.

[158] B. Holian and D. Evans, "Shear viscosities away from the melting line: A comparison of equilibrium and nonequilibrium molecular dynamics," *J. Chem. Phys.*, 1983.

[159] C. E. Shannon, "A mathematical theory of communication," *ACM SIGMOBILE Mob. Comput. Commun. Rev.*, vol. 5, no. 1, p. 3, Jan. 2001.

[160] H. Berendsen, "Molecular dynamics with coupling to an external bath," *J. ...*, 1984.

[161] W. Hoover, "Canonical dynamics: equilibrium phase-space distributions," *Phys. Rev. A*, 1985.
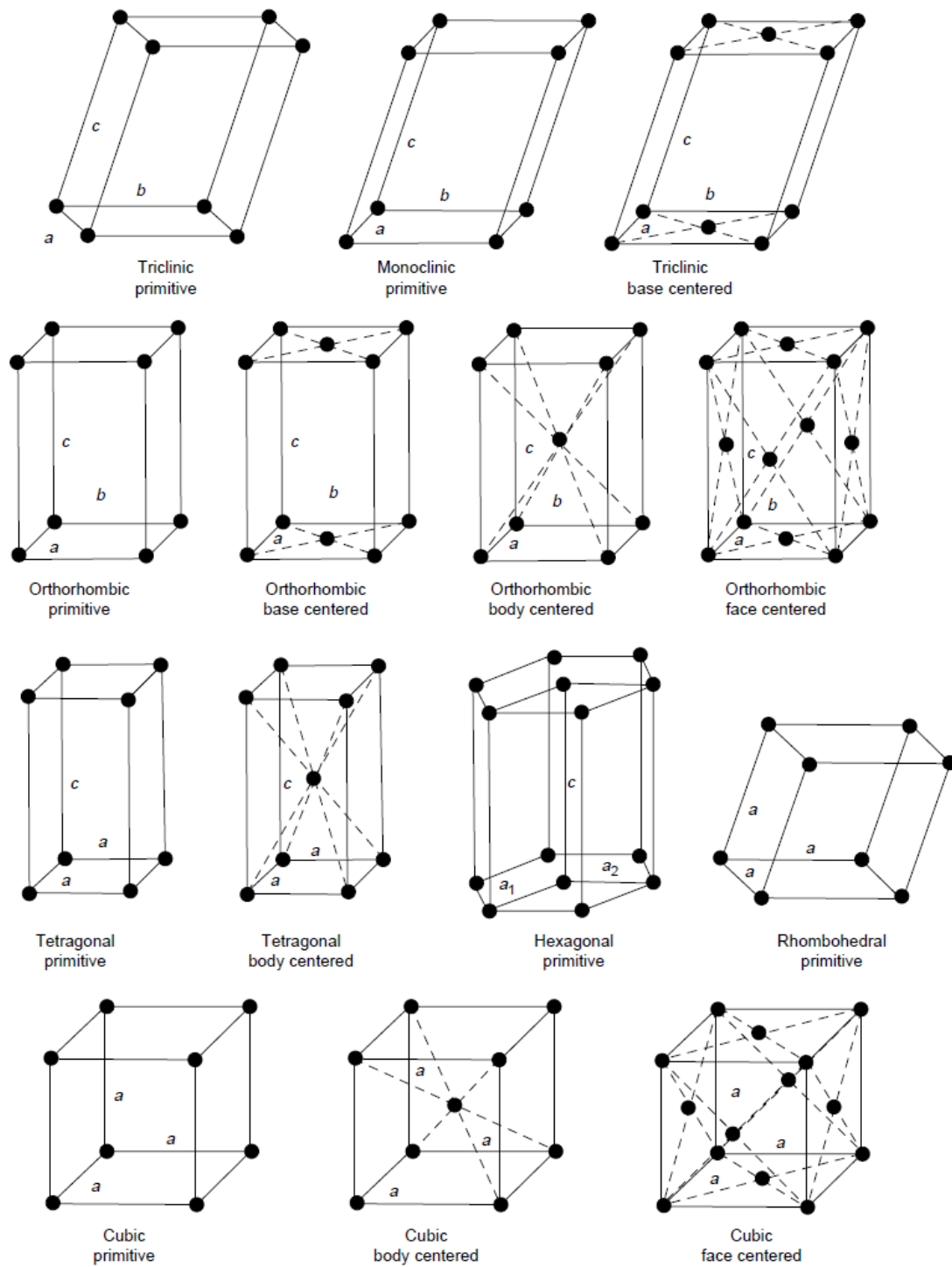
# Appendix A

## Appendix A.1: Bravais lattices



**Figure A.1:** The fourteen Bravais lattices [140]

## Appendix A.2: Determination of Miller indices

In order to denote directions and planes in a lattice the Miller indices are used. The procedure to determine the Miller indices characterising a plane for a cubic system is as follows:

1.  The intercepts of the plane with the axes $x = a$, $y = b$ and $z = c$ are determined.
2.  The reciprocals $h$, $k$, $l$ are then determined, where: $h = \frac{1}{x} = \frac{1}{a}$, $k = \frac{1}{y} = \frac{1}{b}$ and $l = \frac{1}{y} = \frac{1}{c}$.
3.  The reciprocals are then multiplied or divided by a number to form the smallest $(h, k, l)$ set of integers, which are the miller indices for this plane.

Figure A.2 illustrates two examples of calculating the Miller indices for the corresponding planes:
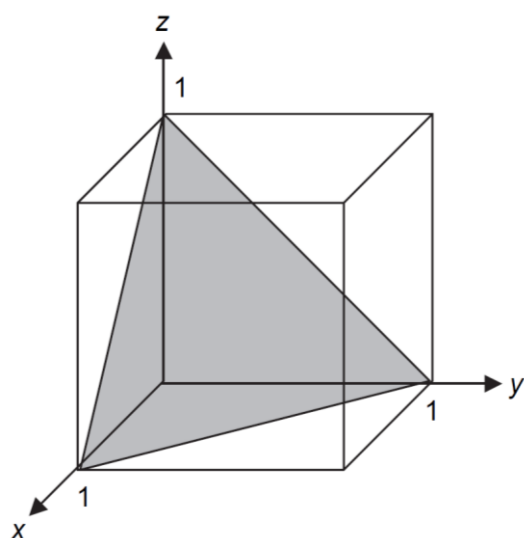


1.  $x = 1, y = 1, z = 1$
2.  Reciprocals: $\frac{1}{x} = 1, \frac{1}{y} = 1, \frac{1}{z} = 1$
3.  No fractions to clear
4.  Miller indices: (1,1,1)
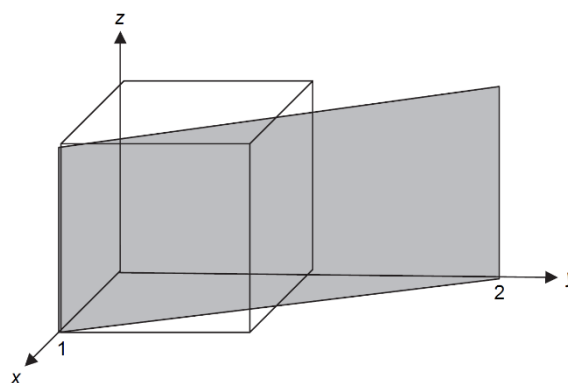
1.  $x = 1, y = 2, z = \infty$ (the plane does not intercept the z-axis)
2.  Reciprocals: $\frac{1}{x} = 1, \frac{1}{y} = \frac{1}{2}, \frac{1}{z} = 0$
3.  Clear fractions ($\times 2$): $\frac{1}{x} = 2, \frac{1}{y} = 1, \frac{1}{z} = 0$
4.  Miller indices: (2,1,0)

**Figure A.2:** Determination of Miller indices

## Appendix A.3: Energy minimisation techniques

### Steepest descent

Steepest descent is a simple but not very effective minimisation method and uses the first derivative of the potential energy $U(\mathbf{R})$ to find a local minimum, where $\mathbf{R}$ is the position vector of the atoms. At every iteration the negative first derivative of the potential energy, which is equal to the force $\mathbf{F}$, is calculated and then $\mathbf{R}$ is displaced by $\mathbf{F}\Delta$ where $\Delta$ is an increment. The procedure is repeated until the absolute value of the force $|\mathbf{F}|$ becomes smaller than a quantity $\varepsilon$. The algorithm is illustrated in Figure A.3.
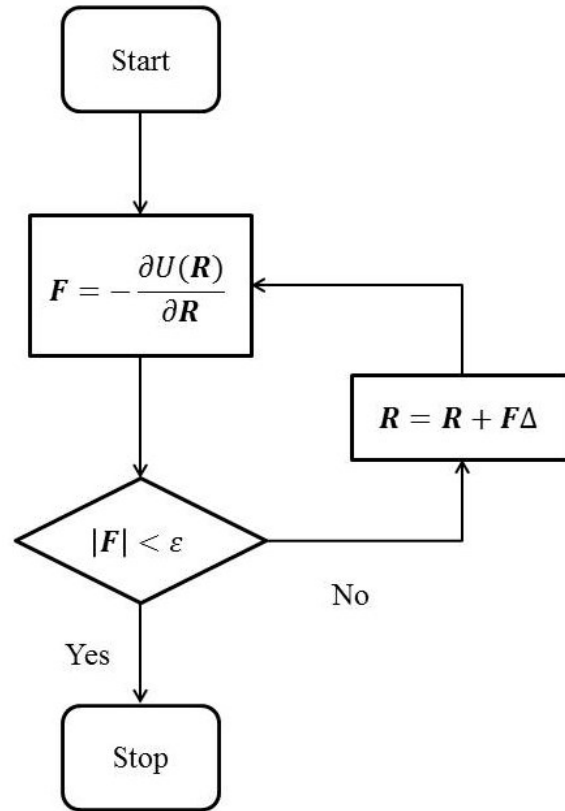
**Figure A.3:** Flowchart of the steepest descent algorithm

## Conjugate gradient

The conjugate gradient (CGR) method is more effective compared to the steepest descent technique as it accumulates information from previous iterations. In each iteration, the search direction is calculated and used to compute the next direction in the following timestep. Therefore, the subsequent search directions do not coincide with the preceding ones. As a result, the direction towards the local minimum is refined and the convergence is faster compared to the steepest descent algorithm. On the other hand, this method is computationally expensive and shall be used in large systems where the longer computational time is compensated by the increased efficiency.

In the CG method any two search directions $d^{(n)}$ and $d^{(m)}$ are linked according to the following equation:

$$d^{(n)} \cdot G \cdot d^{(m)} = 0 \qquad \text{Eq. A.1}$$

where $G$ is a positive definite matrix. When $n = n_f$ there are no directions left to search for the potential energy minimum, the minimum of the potential energy has been found and the loop is terminated. In other words, the number of iterations needed to locate the potential energy minimum is equal to the dimensionality of the system. A flowchart of the CG algorithm is illustrated in Figure A.4.

104
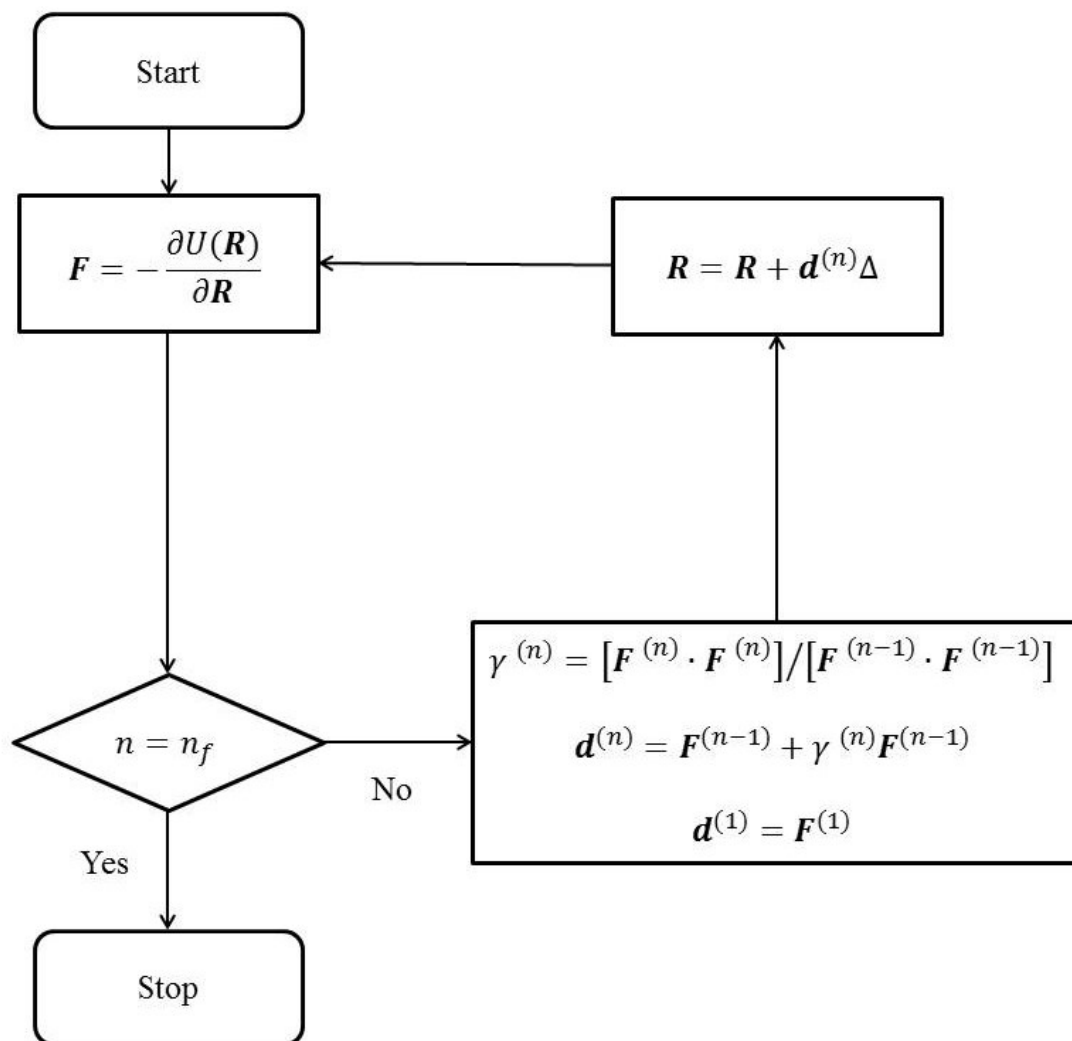
**Figure A.4:** Flowchart of the conjugate gradient algorithm

## Newton-Raphson

The Newton-Raphson method uses both the first and second order derivatives in order to identify the search direction. The main disadvantages of this method are the high storage requirements and computational cost. Thus, it is not recommended for the minimisation of large systems away from the potential energy minimum, but just for cases when rapid convergence is expected.

## Appendix A.4: Chemical Bonds

The behaviour of materials is dependent on the interaction between the molecules and the atoms, which are governed by the laws of quantum mechanics. In nature there are different kinds of bonds but all chemical bonds are characterised by the movement of the electrons around the atoms. However, all the types of bonds exhibit a common behaviour: two bonded atoms are repulsed when the distance between them is smaller than a specified distance $r_0$ and attracted at larger distances between them (Figure A.5). The interatomic distance for which the potential energy is minimum is called equilibrium bond length and the corresponding value of the potential energy is called bond energy. Chemical bonds can be categorised as follows:

1. Covalent bonds
2. Metallic bonds
3. Ionic bonds
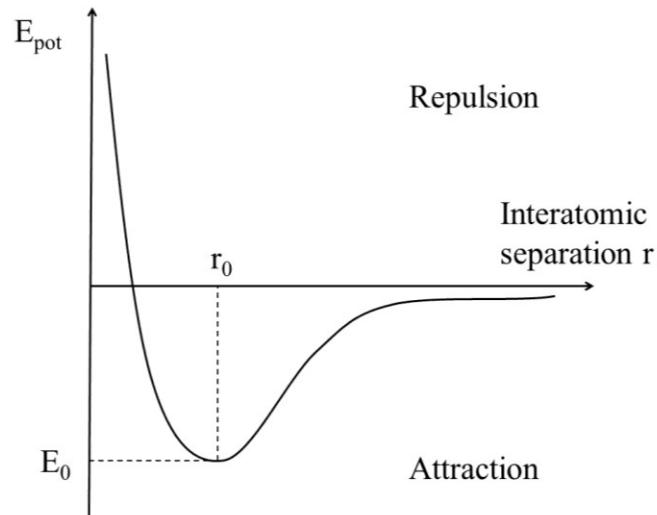


**Figure A.5:** Typical characteristics of chemical bonds

## Covalent bonds

In this type of bonding, electrons are shared between nuclei and there is an attraction between the two nuclei because of the shared electrons. For example, in the case of the $H_2$ molecule two electrons are equally shared between the corresponding nuclei. However, the distribution of the electrons is not always equal but one of the bonded atoms attracts the shared electrons more strongly (Figure A.6). This type of bonds are called polar covalent. Covalent bonds can be found in carbon nanotubes (C-C bond) and organic molecules and are the strongest chemical bonds.
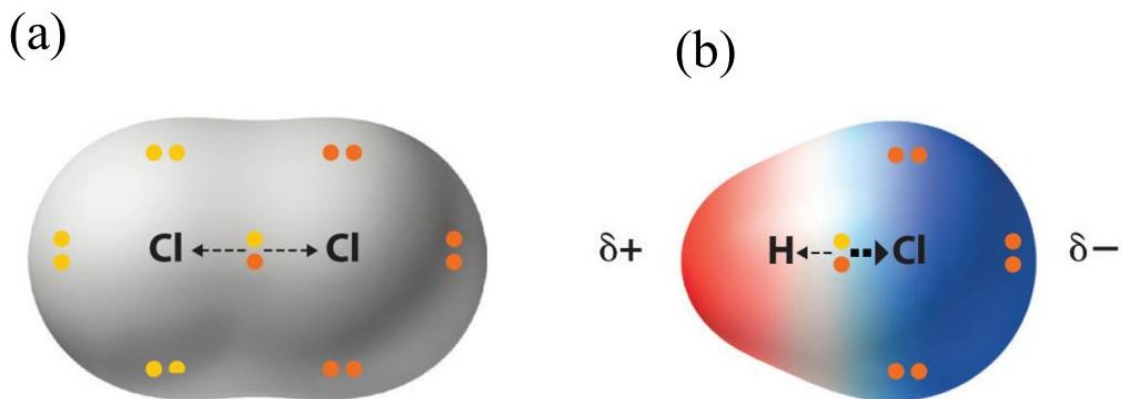


**Figure A.6:** (a) Nonpolar and (b) polar covalent bonds

## Metallic bonds

In metals, bonds are formed from the electrostatic attraction between delocalised electrons and positive ions. The delocalised ions form a "sea" and travel around the metal

crystal. The symmetric packing of the metal atoms into crystals and the constant movement of electrons make the metal bonding strong and indirectional. This can explain some of their macroscopic properties such as their isotropy, the high tensile strength and ultimate thermal and electrical conductivity.
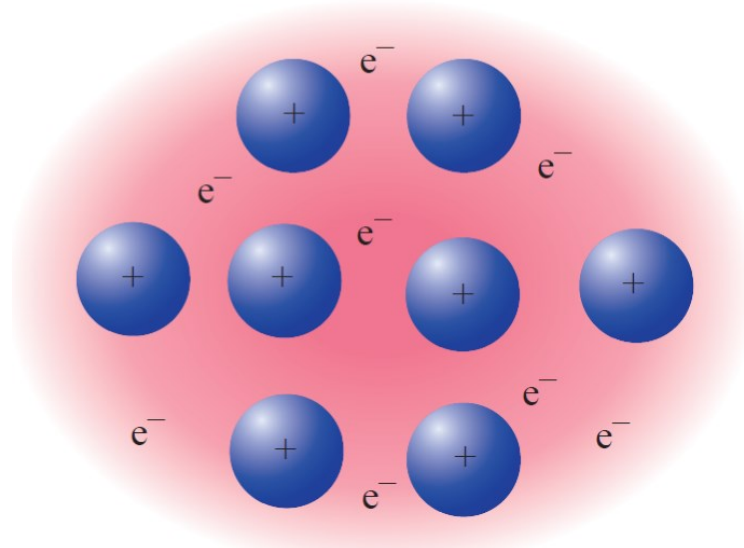


**Figure A.7:** Electron sea model [141]

## Ionic bonds

Ionic bonds are formed when electrons are transferred from one atom to another forming two oppositely charged ions which are electrostatically attracted. Ionic bonding is similar to covalent bonding with the difference that the electron sharing is strongly unequal. This is due to the fact that the two atoms forming ionic bonds have low and high electron affinity respectively. Ionic bonds can be found in ceramics such as $SiO_2$ and $Al_2O_3$.

## Appendix A.5: Force Fields for Macromolecules

In order to model polymeric molecules such as proteins, complex forcefields have to be utilised due to the complex atomistic structure and the variety of bond types involved in such systems. More specifically, when modelling polymers we have to account for covalent, ionic and VdW terms when calculating the potential energy of the system.

One of the most popular force fields for modelling macromolecules is CHARMM [142]. CHARMM includes harmonic and anharmonic terms for the description of the covalent, VdW, ionic and hydrogen interactions as illustrated in Figure A.8. The energy function of the CHARMM force field is the sum of the bonded and non-bonded potential energy terms:

$$V_{tot} = V_{bonded} + V_{non-bonded}$$

<div align="right">Eq. A.2</div>

where:

$$V_{bonded} = V_{bond} + V_{angle} + V_{dihedral} + V_{improper} + V_{UB}$$

<div align="right">Eq. A.3</div>

The terms of Eq. A.3 are listed below:

$$V_{bond} = \sum_{bonds} k_b (b - b_0)^2$$

$$V_{angle} = \sum_{angles} k_\theta (\theta - \theta_0)^2$$

$$V_{dihedral} = \sum_{dihedrals} k_\varphi [1 + cos(n\varphi - \delta)]$$

$$V_{improper} = \sum_{impropers} k_\omega (\omega - \omega_0)^2$$

$$V_{Urey-Bradley} = \sum_{Urey-Bradley} k_{ub} (b^{1-3} - b^{1-3,0})^2$$

In the preceding equations, $k_i$ are force constants, and the naught terms $b_0$, $\theta_0$, $n$, $\omega_0$ $b^{1-3,0}$ are parameters read from the CHARMM force field tables. The Urey-Bradley term describes the interactions between the atoms 1 and 3 which are separated by two bonds and $b^{1-3}$ is the distance between them. The potential energy due to the non-bonded interactions is defined as:

$$V_{non-bonded} = V_{LJ} + V_{coul} \qquad \text{Eq. A.4}$$

with:

$$V_{LJ} = \sum_{non-bonded\ pairs} \varepsilon_{ij} \left[ \left( \frac{\sigma_{ij}}{r_{ij}} \right)^{12} - 2 \left( \frac{\sigma_{ij}}{r_{ij}} \right)^6 \right]^2$$

$$V_{coul} = \sum_{non-bonded\ pairs} \frac{q_i q_j}{\varepsilon r_{ij}}$$

where $q_i$, $q_j$ are the charges assigned to atoms $i$ and $j$ respectively and $\varepsilon$ is the effective dielectric constant ($\varepsilon = 1.602 \times 10^{-19}\ C$ for vacuum). Moreover, $\varepsilon_{ij}$ and $\sigma_{ij}$ are the LJ parameters for a pair of atoms $i,j$. When the atoms $i,j$ are unlike $\varepsilon_{ij}$ and $\sigma_{ij}$ are calculated using the Lorentz-Berthelot mixing rule:

$$\varepsilon_{ij} = \sqrt{\varepsilon_i \varepsilon_j} \qquad \text{Eq. A.5}$$

$$\sigma_{ij} = \frac{\sigma_i + \sigma_j}{2}$$

k$_r$, r

**Bond stretching**

$$V_{bond} = \sum_{bonds} k_b (b - b_0)^2$$

k$_\theta$, θ

**Angle bending**

$$V_{angle} = \sum_{angles} k_\theta (\theta - \theta_0)^2$$

**Dihedral torsion**

k$_\varphi$, φ

$$V_{dihedral} = \sum_{dihedrals} k_\varphi [1 + cos(n\varphi - \delta)]$$

δ$^+$

δ$^-$

**Electrostatic interactions**

$$V_{coul} = \sum_{non-bonded\ pairs} \frac{q_i q_j}{\varepsilon r_{ij}}$$

δ$^-$

δ$^+$

**VdW interactions**

$$V_{LJ} = \sum_{non-bonded\ pairs} \varepsilon_{ij} \left[ \left(\frac{\sigma_{ij}}{r_{ij}}\right)^{12} - 2\left(\frac{\sigma_{ij}}{r_{ij}}\right)^6 \right]^2$$

**Figure A.8:** Interaction types in the CHARMM forcefield

CHARMM belongs to a family of force fields with similar characteristics such as Dreiding [143], Amber [144] and UFF [145]. The most significant of their disadvantages is that bonds cannot be broken or created, a fact that prohibits the modelling of chemical reactions such as the crosslinking process in polymers. Moreover, charges are fixed and the equilibrium angles do not change with stretch.

## Appendix A.6: Reactive Force Fields

Reactive force fields have been developed in order to overcome the incapability of classical force fields to describe chemical reactions. Brenner [146] was the first to develop a reactive potential for carbon-based systems which was capable of simulating bond forming and breaking during the course of a molecular dynamics simulation. The neighbour list of each atom was regularly updated and it was assumed that short-range bonded interactions are reactive. Another reactive force field developed by Root et al. [147] is VALBOND, which calculates the angle bending energies based on the simple valence bond theory and can describe various geometries found in transition metal compounds, such as hybrids and alkyls. However, the aforementioned force fields do not fully describe fully the chemistry of bond breakage or formation, a problem which has been effectively addressed by the reactive force field ReaxFF [148].

Similar to the force fields for macromolecules, the potential energy in the ReaxFF is given by:

$$V_{total} = V_{bond} + V_{over} + V_{under} + V_{val} + V_{pen} + V_{torsion}$$
$$+ V_{conj} + V_{VdW} + V_{coul}$$

Eq. A.6

where $V_{over}$, $V_{under}$ are the system energy penalties for over- and under-coordination respectively, $V_{pen}$ describes the effects of over- and under-coordination in the central atom on the penalty energy and $V_{conj}$ describes the resonance effects on the molecular energy. Non-bonded interactions ($V_{VdW}$, $V_{coul}$) are calculated for each pair of atoms regardless of their connectivity to avoid any discontinuities that are taking place in the system. To calculate the contributions of electrostatic interactions the shielded Coulomb potential is used to prevent excessive repulsion at short distances:

$$V_{coul} = \sum_{i=1}^{N} \sum_{j=1}^{N} \frac{q_i q_j}{\varepsilon \left[ r_{ij}^3 + \left( \frac{1}{\gamma_{ij}} \right)^3 \right]^{1/3}}$$

Eq. A.7

where $\gamma_{ij}$ is a force field parameter used to describe the contributions of the orbital overlap.

In the ReaxFF the bond order $BO'_{ij}$ is obtained directly from the interatomic distance $r_{ij}$ between atoms $i$ and $j$ as described by Eq. A.8:

$$BO'_{ij} = \exp\left[ p_{bo,1} \left( \frac{r_{ij}}{r_0} \right)^{p_{bo,2}} \right] + \exp\left[ p_{bo,3} \left( \frac{r_{ij}^{\pi}}{r_0} \right)^{p_{bo,4}} \right] + \exp\left[ p_{bo,5} \left( \frac{r_{ij}^{\pi\pi}}{r_0} \right)^{p_{bo,6}} \right]$$

Eq. A.8

where $p_{bo,i}$ are experimental fitting parameters which have been selected to describe the dependence of the bond order on the bond geometry based on experimental and quantum data. The first exponential term in the equation represents the contribution of a sigma bond, the second of a pi bond and the third of a double pi bond (Figure A.9).
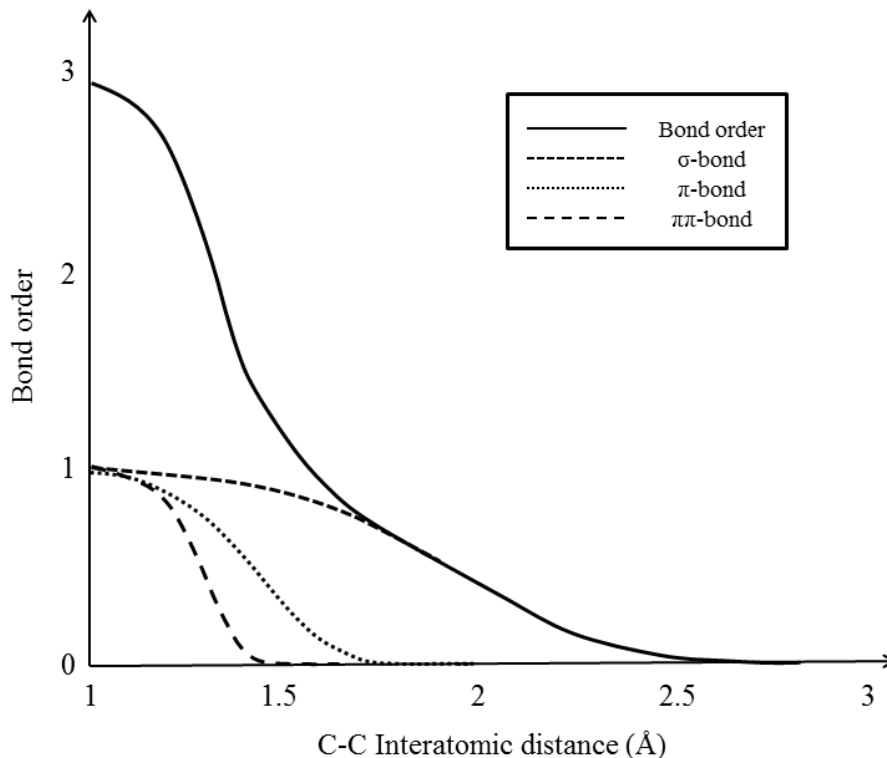
**Figure A.9:** Interatomic distance dependency of the carbon-carbon bond order

To account for the effect of over- and under-coordination the bond order has to be corrected through a group of correction functions based on the degree of deviation of the sum of the uncorrected bond orders around an atomic centre from its valency $Val_i$ ($Val_i = 4$ for carbon atoms, $Val_i = 1$ for hydrogen atoms):

$$\Delta_i' = \sum_{j=1}^{nbond} BO_{ij}' - Val_i \qquad \text{Eq. A.9}$$

Finally, ReaxFF uses QEq which is a geometry-dependent charge equilibration scheme [149] controlling the atomic charges as the atomistic structures change their shape. In ReaxFF a cut-off for the interatomic interactions equal to 10 Å is being used.

The parameters used in the Reactive Force field have been trained against Quantum Mechanics calculations (DFT, experiments) on properties such as bond dissociation, angle distortion, surface energies and equation of state. The optimisation of the parameters of the ReaxFF has been performed using a successive search parameter technique [150] to minimise the following sum of squares:

$$sum \ of \ squares = \sum_{j=1}^{n} \left[ \frac{x_{i,exp} - x_{i,calc}}{\sigma_i} \right]^2 \qquad \text{Eq. A.10}$$

where $x_{i,exp}$ is the Quantum Mechanics result value, $x_{i,calc}$ the ReaxFF calculated value and $\sigma_i$ the weight assigned to the data point $i$.

As expected, due to the increased complexity and frequency of the calculations performed, (e.g. charge equilibration is performed every timestep that the forces exerted on atoms are calculated) ReaxFF is about 10 to 100 times more expensive computationally compared to conventional non-reactive force fields such as CHARMM and DREIDING. Therefore, alternative methods in which reactions are simulated in a stepwise manner using conventional force fields have been developed [111]. However, it is much more efficient than quantum mechanical methods such as DFT and semi-empirical methods (PM3) which are capable of modelling reactivity in molecular systems (Figure A.10).
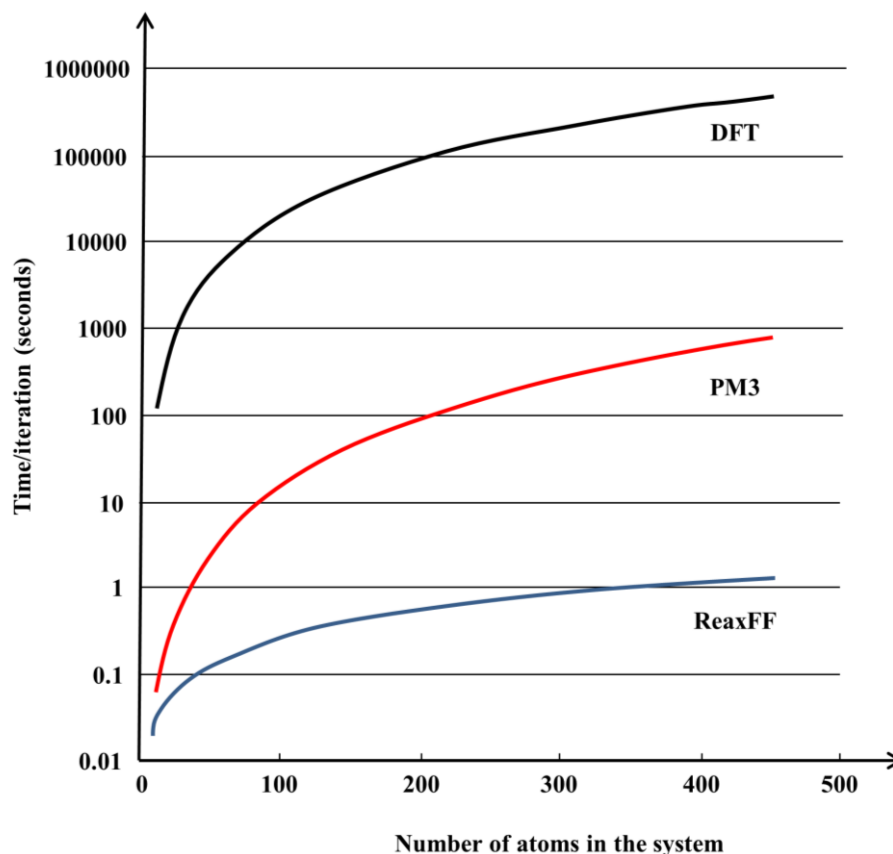


**Figure A.10:** Influence of system size on computer time for various simulation methods

## Appendix A.7: Common Thermodynamic Averages

### Temperature

One of the most important problems in statistical mechanics is to explore the way that the energy of the system is distributed over various directions. This issue has been addressed by the energy equipartition theorem which states that when a system is in equilibrium at temperature $T$, energy will be distributed equally among all the degrees of freedom or varieties of motion in the system. Let's consider the Hamiltonian of a system:

$$H = \sum_i K(\boldsymbol{p}) + V(\boldsymbol{q})$$

Eq. A.11

where $(\mathbf{p}, \mathbf{q})$ a set of canonical coordinates. For Cartesian coordinates Hamilton's equations obtain the following form:

$$\dot{\mathbf{r}}_i = \frac{\mathbf{p}_i}{m_i}$$

$$\dot{\mathbf{p}}_i = -\nabla_{r_i} V = \mathbf{f}_i$$

Eq. A.12

where $\mathbf{p}_i$, $\mathbf{r}_i$ and $m_i$ are the momentum, position and mass of the atom $i$ respectively, $\mathbf{f}_i$ the force exerted on the atom $i$ and $V$ the potential. The total energy is given by:

$$E = \langle H \rangle = \langle E_{kin} \rangle + \langle E_{pot} \rangle$$

Eq. A.13

According to Allen and Tildesley [49] the virial theorem is expressed in the form of generalised equipartition:

$$\langle p_k \frac{\partial H}{\partial p_k} \rangle = k_b T$$

$$\langle q_k \frac{\partial H}{\partial q_k} \rangle = k_b T$$

Eq. A.14

The total kinetic energy is equal to:

$$\langle E_{kin} \rangle = \langle \sum_{i=1}^{N} \frac{|\mathbf{p}_i|^2}{2m_i} \rangle = \frac{1}{2} \sum_{i=1}^{N} \sum_{a=1}^{3} \langle \frac{|\mathbf{p}_i|^2}{m_i} \rangle = \frac{1}{2} \sum_{i=1}^{N} \sum_{a=1}^{3} \langle p_{ia} \frac{\partial H}{\partial p_{ia}} \rangle \overset{Eq.A.12}{\Longleftrightarrow}$$

$$\Leftrightarrow \langle E_{kin} \rangle = \frac{3}{2} N k_b T$$

Eq. A.15

where $N$ is the total number of atoms and $3N$ is the total number of the degrees of freedom. Therefore the average temperature is equal to:

$$T = \frac{2\langle E_{kin} \rangle}{3N k_b}$$

Eq. A.16

## Pressure

Similarly, pressure can be calculated using the virial theorem (Eq. A.13):

$$-\frac{1}{3} \langle \sum_{i=1}^{N} \mathbf{r}_i \cdot \nabla_{r_i} V \rangle = -\frac{1}{3} \langle \sum_{i=1}^{N} \sum_{a=1}^{3} r_{ia} \cdot \nabla_{r_{ia}} V \rangle$$

$$v \qquad = -\frac{1}{3} \sum_{i=1}^{N} \sum_{a=1}^{3} \langle r_{ia} \frac{\partial H}{\partial r_{ia}} \rangle \overset{Eq.A.12}{\Longleftrightarrow}$$

Eq. A.17

$$\overset{Eq.A.12}{\Longleftrightarrow} -\frac{1}{3} \langle \sum_{i=1}^{N} \mathbf{r}_i \cdot \nabla_{r_i} V \rangle = \frac{1}{3} \langle \sum_{i=1}^{N} \mathbf{r}_i \cdot \mathbf{f}_i^{tot} \rangle = -N k_b T$$

However, the total force exerted on an atom is the sum of the intermolecular forces and external forces because of the walls:

$$\frac{1}{3}\langle\sum_{i=1}^{N} r_i \cdot \mathbf{f}_i^{tot}\rangle = \frac{1}{3}\langle\sum_{i=1}^{N} r_i \cdot \mathbf{f}_i^{id}\rangle + \frac{1}{3}\langle\sum_{i=1}^{N} r_i \cdot \mathbf{f}_i^{ext}\rangle = -Nk_bT \qquad \text{Eq. A.18}$$

Eq. A.19 can be written as:

$$PV - \langle W \rangle = Nk_bT \qquad \text{Eq. A.19}$$

where:

$$P = -\frac{1}{3V}\langle\sum_{i=1}^{N} r_i \cdot \mathbf{f}_i^{ext}\rangle$$

is the external pressure because of the effect of the walls and:

$$\langle W \rangle = \frac{1}{3}\langle\sum_{i=1}^{N} r_i \cdot \mathbf{f}_i^{id}\rangle$$

is defined as the internal virial accounting for intermolecular forces. Pressure is finally equal to:

$$PV = \rho k_b T + \frac{\langle W \rangle}{V} \qquad \text{Eq. A.20}$$

where $\rho = N/V$ is defined as the number density.

## Structural properties

The quantities being used for investigating the structure and the behaviour of the system during any molecular simulation can be divided in two main categories based on whether they account for the time evolution of the system or not:

(a) Structural properties
(b) Dynamic properties

To study the structural properties of a system and the extent to which a system deviates from randomness, particle distribution functions are being used. One of the most common particle distribution functions is the radial distribution function (RDF). The RDF is a measure of the average density of particles as a function of the distance from an arbitrary point or particle. RDF is mainly used for liquids where randomness is dominant in contrast to solids which are characterised by the lattice structure.
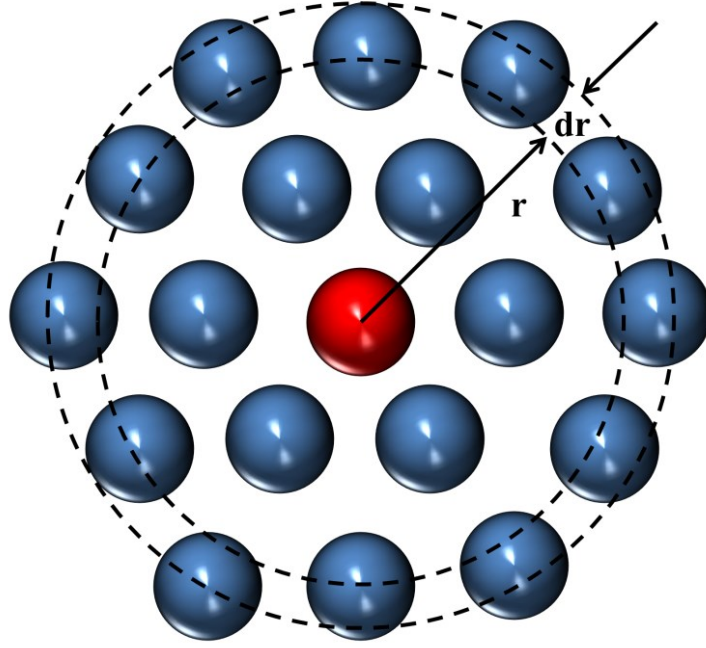
**Figure A.11:** Radial distribution function

The RDF provides an estimation of the average number of atoms lying within the distance $r < r_i < r + \Delta r$ (Figure A.11) and is given by:

$$g(r) = \frac{V}{N^2} \langle \sum_i \sum_{j \neq i} \delta(r - r_{ij}) \rangle \qquad \text{Eq. A.21}$$

where $V$ is the system volume and $N$ the number of atoms. An alternative way of exploring the structure of particles in a system is to draw typical density profiles by counting the number of atoms in orthogonal bins. However, the RDF provides the user with the additional advantage to calculate the number density with respect to a point or a group of points of reference.

The static structure factor provides a measure of the correlation between the particle positions in the reciprocal space. Knowledge of the static structure factor is crucial for understanding the structure and the properties of liquid metals and alloys ([151], [152]). The static structure factor is defined as the density correlation function in the Fourier space:

$$S(q) = \frac{1}{N} \sum_j \sum_k \langle e^{-iq(r_j - r_k)} \rangle \qquad \text{Eq. A.22}$$

where N is the number of atoms, $q = |q| = {2\pi}/{\lambda}$ is the wave vector and $\lambda$ is the wavelength. Generally, for large length scales or small values of the wave vector ($q < 1$) the static structure factor $S(q)$ is only dependent on $q$:

$$S(q) \sim q^{-d} \qquad \text{Eq. A.23}$$

where $d$ is the fractal dimension of clusters [153].

One other quantity used to describe the structure of particles is the radius of gyration, which is mainly used in polymer physics. It is defined as the weighted root mean square (RMS) average of the magnitudes of the vectors connecting the centre of mass to the points belonging to the polymer chain or to the rigid body in general:

$$R_g^2 = \frac{1}{N} \sum_{i=1}^{N} (r_i - r_m)^2$$

<div align="right">Eq. A.24</div>

where $r_m$ is the position of the centre of mass of the body. The radius of gyration $R_g$ is indicative of the level of compaction in the system. In the case of polymeric system as $R_g$ decreases the polymer chain will obtain a more folded conformation.

## Dynamic properties and transport coefficients

The above mentioned quantities fall to the category of structural properties. On the other hand, dynamic properties involve the time evolution during the averaging procedure. One of the most important dynamic properties describing how fast particles move is the self- or tracer-diffusion coefficient which is given by the Einstein's relation for the motion of Brownian particles:

$$D = \lim_{t \to \infty} \frac{1}{2dt} \langle |\boldsymbol{r}(t) - \boldsymbol{r}(0)|^2 \rangle$$

<div align="right">Eq. A.25</div>

where $\boldsymbol{r}(t)$ is the position of a single particle, $d$ is the dimensionality of the system and:

$$\langle |\boldsymbol{r}(t) - \boldsymbol{r}(0)|^2 \rangle = MSD(t) = \frac{1}{N} \sum_{i=1}^{N} (|\boldsymbol{r}(t) - \boldsymbol{r}(0)|^2)$$

<div align="right">Eq. A.26</div>

is the mean square displacement (MSD), which provides an estimation of the distance travelled by each atom during the time interval $(0, t)$. When the simulation time is very large, Eq. A.25 can be written as:

$$D = \frac{1}{6t} MSD(t)$$

<div align="right">Eq. A.27</div>

It is therefore clear that the Diffusion coefficient can be obtained by calculating the slope of the MSD-versus-time diagram. The diffusion coefficient can also be estimated by using the Green-Kubo relations [154]:

$$D_a = \frac{1}{3} \int_0^\infty \langle u_{i,a}(t) \cdot u_{i,a}(0) \rangle \, dt$$

<div align="right">Eq. A.28</div>

where $u_{i,a}$ is $a$-component of the velocity of the atom $i$. The term $\langle u_{i,a}(t) \cdot u_{i,a}(0) \rangle$ is called the velocity autocorrelation function (VACF).

One additional fluid property that can be calculated using the Green-Kubo relations is the shear viscosity which is given by [49]:

$$\eta_{shear} = \frac{V}{k_b T} \int_0^\infty \langle P_{\alpha\beta}(t) \cdot P_{\alpha\beta}(0) \rangle \, dt \qquad \text{Eq. A.29}$$

where $\alpha, \beta \ (a \neq \beta)$ are Cartesian coordinates and $P_{\alpha\beta}$ is an off-diagonal term of the pressure tensor of the system:

$$P_{\alpha\beta} = \frac{1}{V} \left( \sum_{i=1}^N \frac{p_{ix} p_{iy}}{m_i} + \sum_{i=1}^N \sum_{i<j}^N r_{ijx} f_{ijy} \right) \qquad \text{Eq. A.30}$$

In Eq. A.30 $f_{ij}$ is the interatomic force between atoms $i$ and $j$ and $p_i$ the momentum of the atom $i$. The bulk viscosity can by estimated in a similar manner:

$$\eta_{bulk} = \frac{1}{V k_b T} \int_0^\infty \langle \delta P(t) \cdot \delta P(0) \rangle \, dt \qquad \text{Eq. A.31}$$

where:

$$P = \frac{1}{3} \sum_{i=1}^a P_{aa} = \frac{P_{xx} + P_{yy} + P_{zz}}{3} \qquad \text{Eq. A.32}$$

and:

$$\delta P(t) = P(t) - \langle P \rangle \qquad \text{Eq. A.33}$$

Moreover, the thermal conductivity $\lambda$ can also been calculated using the Green-Kubo formulas [106]:

$$\lambda = \frac{V}{3 k_b T^2} \int_0^\infty \langle \boldsymbol{J}(t) \cdot \boldsymbol{J}(0) \rangle \, dt \qquad \text{Eq. A.34}$$

where $a = x, y, z$, the term $\langle \boldsymbol{J}(t) \cdot \boldsymbol{J}(0) \rangle$ is the heat flux autocorrelation function and $\boldsymbol{J}$ is the heat flux vector which according to Dong et al. [155] can be defined as:

$$\boldsymbol{J} = \frac{1}{V} \left[ \sum_{i=1}^N e_i \boldsymbol{u}_i + + \frac{1}{2} \sum_{i<j}^N \left( \boldsymbol{f}_{ij} \cdot (\boldsymbol{u}_i + \boldsymbol{u}_j) \right) \boldsymbol{r}_{ij} \right] \qquad \text{Eq. A.35}$$

In Eq. A.35 $e_i$ is the total energy (potential and kinetic) carried by the particle $i$.

The main advantage of the Green-Kubo relations is that the transport coefficients can be estimated with just one run. However, they have been proven to be size-dependent [156] and computationally expensive. Moreover their output depends on the geometry of the system under examination as they are very sensitive to any system noise [157]. As a result the non-equilibrium molecular dynamics (NEMD) technique, which combines molecular dynamics simulations with constitutive equations, is also being employed for studying the transport

properties of fluids. For example the shear viscosity of fluids can be obtained by estimating the time-averaged off-diagonal pressure terms $P_{xy}$ and $P_{yx}$ as follows:

$$\eta = -\frac{\langle P_{xy} + P_{yx}\rangle}{2\gamma}$$

where $\gamma = \frac{\partial u_x}{\partial y}$ is the shear or strain rate. The results of the EMD and NEMD techniques have been in agreement between them in some cases [158], but generally NEMD is preferable for the estimation of transport properties.

## Appendix A.8: Partition function of statistical ensembles

Let's consider a system which is surrounded by a heat bath of constant temperature $T$. When in equilibrium the temperature of the system is constant and equal to $T$ as well. The system and the heat bath can exchange energy so the system can be found in different energy states $E_i$. Moreover, let $N$ be the total number of measurements (observations), $n_i$ the number of times that the energy state $E_i$ is observed and $\langle E\rangle$ the expected value of energy. The following equations constitute the constraints of the NVT ensemble:

$$N = \sum_i n_i$$

$$\sum_i n_i E_i = N\langle E\rangle$$

Moreover, using the method of combination the number of arrangements of the microstates is equal to:

$$\Omega = \frac{N!}{n_1! \cdot n_2! \cdot n_3! \cdots} = \frac{N!}{\prod_i n_i!}$$

We can also define the probability of observing the microstate $E_i$ as:

$$P(E_i) = P_i = \frac{n_i}{N}$$

According to the basic properties of probabilities:

$$\sum_i P_i = \sum_i \frac{n_i}{N} = 1$$

By combining Eq. A.37 and Eq. A.40 we can write:

$$\sum_i P_i E_i = \langle E\rangle$$

In the previous chapters, it has been mentioned that a system being in equilibrium will flow through all the possible microstates defined by the imposed constraints over a time interval. In other words, the number of arrangements of the microstates has to be maximum in

order to ensure that the system is in equilibrium. However, performing calculations with products is more complicated than with sums. Therefore, we should try to maximise the function $\ln(\Omega)$ since the logarithm is a monotonically increasing function. After some algebraic manipulation and using Stirling's approximation we obtain a relationship very similar to Shannon's entropy definition [159]:

$$\ln(\Omega) = -N \sum_i [P_i \ln(P_i)]$$

Eq. A.42

Using the Lagrange multipliers $\alpha$ and $\beta$ in order to maximise $\ln(\Omega)$ with respect to the constraints stated in Eq. A.37 and differentiating with respect to $i$ we obtain:

$$P_i = e^{-(1+\alpha)} e^{-\beta E_i}$$

Eq. A.43

where $\frac{1}{z} = e^{-(1+\alpha)}$ the partition function and $\beta = \frac{1}{k_b T}$ with $k_b = 1.38064852 \times 10^{-23} \, m^2 kg \, s^{-2} K^{-1}$ as the Boltzmann constant. In order to estimate the partition function we have to use Eq. A.40:

$$\sum_i P_i = 1 \overset{\text{Eq.A.43}}{\Longleftrightarrow}$$

$$\Leftrightarrow \sum_i \frac{1}{z} e^{-\beta E_i} = 1 \Leftrightarrow$$

Eq. A.44

$$\Leftrightarrow z_{NVT} = \sum_i e^{-\beta E_i}$$

Similarly we can obtain the partition function for all the basic statistical ensembles:

| Ensemble | Constraints | Z | $p_i$ |
|---|---|---|---|
| Microcanonical (NVE) | N, V, E | $\sum_i \delta(E_i - E)$ | $\frac{\delta(E_i - E)}{z_{NVE}}$ |
| Canonical (NVT) | N, V, T | $\sum_i e^{-\beta E_i}$ | $\frac{e^{-\beta E_i}}{z_{NVT}}$ |
| Grand Canonical | $\mu$, V, T | $\sum_i e^{-\beta N_i \mu} z_{NVT}$ | $\frac{e^{-\beta(E_i - \mu N_i)}}{z_{\mu VT}}$ |
| Isothermal –Isobaric (NPT) | N, P, T | $\sum_i e^{\beta PV_i} z_{NVT}$ | $\frac{e^{-\beta(E_i + PV_i)}}{z_{NPT}}$ |

**Table A.1:** Common statistical ensembles [157]

Each statistical ensemble is associated with a thermodynamic quantity. The entropy $S$ is associated with the Microcanonical ensemble:

$$S = k_b \cdot ln(z_{NVE}) \hspace{3cm} \text{Eq. A.45}$$

The Helmholtz free energy $A$ is linked with the canonical partition function as follows:

$$A = -k_b T \cdot ln(z_{NVT}) \hspace{3cm} \text{Eq. A.46}$$

Pressure is the appropriate thermodynamic quantity for the grand canonical ensemble:

$$PV = -k_b T \cdot ln(z_{\mu VT}) \hspace{3cm} \text{Eq. A.47}$$

Finally, the Gibbs free energy $G$ is estimated using the isobaric-isothermal partition function:

$$G = -k_b T \cdot ln(z_{NPT}) \hspace{3cm} \text{Eq. A.48}$$

## Appendix A.9: Thermostats

One of the simplest methods to control the system temperature is to rescale the particle velocities, i.e. to multiply each particle velocity by a factor:

$$u_{new} = \sqrt{\frac{T}{T_{ins}}} u_{old} \hspace{3cm} \text{Eq. A.49}$$

where $T$ is the desired temperature and $T_{ins}$ is the estimated instant temperature of the system as defined by Eq. A.16. The main disadvantage of velocity rescaling is that the produced results do not correspond to any statistical ensemble. Therefore its use is mainly restricted to the equilibration phase. Moreover, velocity rescaling is a time irreversible and nondeterministic method.

The Berendsen thermostat [160] is also based on velocity rescaling which in this case is given by:

$$\frac{du}{dt} = \frac{f}{m} + \frac{1}{2\tau}\left(\frac{T_{md}}{T(t)} - 1\right)u \hspace{3cm} \text{Eq. A.50}$$

where $\tau$ is a constant called the rise time of the thermostat, $T(t)$ is the current value of the temperature and $T_{md}$ the desired temperature. The Berendsen thermostat is a very effective and robust way to control the system temperature. However, it does not correspond to any statistical ensemble as well and therefore its use is restricted to the equilibration phase.

The Nose Hoover thermostat [161] is coupled with the canonical (NVT) ensemble and introduces an extra degree of freedom $s$ which corresponds to a heat bath. The Hamiltonian is extended and modified as follows:

$$H_{N-H} = \sum_{i=1}^{N} \frac{p_i^2}{m_i} + V(R) + \frac{\zeta^2 Q}{2} + \frac{3N \ln s}{\beta} \qquad \text{Eq. A.51}$$

where $Q$ is an imaginary mass and $\zeta$ the friction coefficient. The Nose Hoover thermostat is deterministic and time reversible but in some cases the system produced with the application of this thermostat is not ergodic.

The Langevin thermostat is used to control the temperature by modifying Newton's equations of motion:

$$m_i \ddot{r}_i = -\frac{\partial V}{\partial r_i} - m\Gamma \dot{r}_i + A_i(t) \qquad \text{Eq. A.52}$$

where $V$ is the potential energy and $\Gamma(s^{-1})$ is a friction coefficient. In Eq. A.52 the first term corresponds to the force exerted on the atom $i$, the second term is the drag force and $A_i(t)$ is a stochastic term corresponding to the noise (random force) with a dispersion equal to:

$$\langle A_i(t) A_j(t + \Delta t) \rangle = 2\Gamma m_i k_b T \Delta t \delta_{ij} \delta(\Delta T) m_i \ddot{r}_i = -\frac{\partial V}{\partial r_i} - m\Gamma \dot{r}_i + A_i(t) \qquad \text{Eq. A.53}$$

From Eq. A.53 we can see that the second and third terms of Eq. A.52 are linked and balanced in order to achieve the desired temperature. The Langevin thermostat is used to simulate a canonical ensemble and has been proven to be ergodic. Moreover, a large timestep compared to non-stochastic thermostats can be used.